



AFRL-AFOSR-VA-TR-2018-0389

TRANSITION METAL AND RARE EARTH DOPED II-VI CHALCOGENIDES FOR OPTICALLY AND ELECTRICALLY PUMPED BROADLY TUNABLE MID-IR LASERS

Sergey Mirov
UNIVERSITY OF ALABAMA AT BIRMINGHAM

10/05/2018
Final Report

DISTRIBUTION A: Distribution approved for public release.

Air Force Research Laboratory
AF Office Of Scientific Research (AFOSR)/ RTB1
Arlington, Virginia 22203
Air Force Materiel Command

DISTRIBUTION A: Distribution approved for public release.

REPORT DOCUMENTATION PAGE		<i>Form Approved</i> <i>OMB No. 0704-0188</i>	
<p>The public reporting burden for this collection of information is estimated to average 1 hour per response, including the time for reviewing instructions, searching existing data sources, gathering and maintaining the data needed, and completing and reviewing the collection of information. Send comments regarding this burden estimate or any other aspect of this collection of information, including suggestions for reducing the burden, to Department of Defense, Executive Services, Directorate (0704-0188). Respondents should be aware that notwithstanding any other provision of law, no person shall be subject to any penalty for failing to comply with a collection of information if it does not display a currently valid OMB control number.</p> <p>PLEASE DO NOT RETURN YOUR FORM TO THE ABOVE ORGANIZATION.</p>			
1. REPORT DATE (DD-MM-YYYY) 16-10-2018	2. REPORT TYPE Final Performance	3. DATES COVERED (From - To) 30 Sep 2013 to 29 Sep 2018	
4. TITLE AND SUBTITLE TRANSITION METAL AND RARE EARTH DOPED II-VI CHALCOGENIDES FOR OPTICALLY AND ELECTRICALLY PUMPED BROADLY TUNABLE MID-IR LASERS		5a. CONTRACT NUMBER	
		5b. GRANT NUMBER FA9550-13-1-0234	
		5c. PROGRAM ELEMENT NUMBER 61102F	
6. AUTHOR(S) Sergey Mirov		5d. PROJECT NUMBER	
		5e. TASK NUMBER	
		5f. WORK UNIT NUMBER	
7. PERFORMING ORGANIZATION NAME(S) AND ADDRESS(ES) UNIVERSITY OF ALABAMA AT BIRMINGHAM 701 20TH STREET SOUTH AB 990 BIRMINGHAM, AL 35294-0001 US		8. PERFORMING ORGANIZATION REPORT NUMBER	
9. SPONSORING/MONITORING AGENCY NAME(S) AND ADDRESS(ES) AF Office of Scientific Research 875 N. Randolph St. Room 3112 Arlington, VA 22203		10. SPONSOR/MONITOR'S ACRONYM(S) AFRL/AFOSR RTB1	
		11. SPONSOR/MONITOR'S REPORT NUMBER(S) AFRL-AFOSR-VA-TR-2018-0389	
12. DISTRIBUTION/AVAILABILITY STATEMENT A DISTRIBUTION UNLIMITED: PB Public Release			
13. SUPPLEMENTARY NOTES			
14. ABSTRACT AFOSR sponsored research work at University of Alabama at Birmingham enabled development of new middle-infrared chalcogenide laser materials via post-growth radiation and hot isostatic pressing enhanced thermal diffusion of laser active transition metal impurities into the polycrystalline crystal host. We report on unique process of recrystallization and effective doping of ZnS ceramics under hot isostatic pressing resulting in a large cm-scale monocrystalline domains formation and an increase of the Fe diffusion length by four orders of magnitude. In collaboration with the University of Central Florida and IPG Photonics Corporation a new breakthrough was demonstrated: a first ultrafast optical parametric oscillator based on random phase matching in disordered polycrystal, ZnSe ceramic. A new kinetic Monte Carlo simulation algorithm for cation diffusion in zinc blend (ZB) crystals has been developed. One of difficulty is the lattice indexing for ZB crystals. We found that diffusion in ZB crystals can be mapped to the diffusion in the fourdimensional simple cubic crystal with certain constraints. This algorithm has various advantage, in particular it finds the neighboring lattice sites quickly and also it makes it very easy to calculate the hopping distance between two distance lattice sites. Using this algorithm, we have simulated diffusion processes based on interstitial-assisted knock-out and vacancy-assisted mechanisms. The simulation was carried out on the cluster computer using 500 cores. The results are analyzed with waiting time distribution. The relation between the diffusion constants and concentration of the assisting impurities. Based on the the results we are able to explain the increases of Cr-ion diffusion rate under high concentration of Zn interstitials in ZnS. UAB team also created a multilayer thin film structure that integrates an optically-active m			

15. SUBJECT TERMS

crystal growth, non-equilibrium, state of the material, state properties, non-equilibrium thermodynamics, kintec, rare earth materials, chalcogenide materials, compounds

16. SECURITY CLASSIFICATION OF:			17. LIMITATION OF ABSTRACT UU	18. NUMBER OF PAGES	19a. NAME OF RESPONSIBLE PERSON SAYIR, ALI
a. REPORT Unclassified	b. ABSTRACT Unclassified	c. THIS PAGE Unclassified			19b. TELEPHONE NUMBER <i>(Include area code)</i> 703-696-7236

UNCLASSIFIED

Report UAB

Transition metal and rare earth doped II-VI chalcogenides for optically and electrically pumped broadly tunable mid-IR lasers

S. Mirov, V. Fedorov, R. Camata, R. Kawai, D. Martyshkin, A. Martinez, O. Gafarov, J. Peppers, Z. Lindsey, M.R. Rhoades, K. Bentley

Prepared for AFOSR Contract FA9550-13-1-0234

September 2018



Department of Physics
310 Campbell Hall, 1300 University Blvd,
Birmingham, AL 35294
<http://www.phy.uab.edu>

UNCLASSIFIED

Table of Contents

1. Introduction	3
2. Novel diffusion doped mid-IR laser active materials	4
2.1 Crystal Field Engineering of Transition Metal Doped II-VI Ternary and Quaternary Semiconductors for Mid-IR Tunable Laser Applications	4
2.2 Mid-IR and Near-IR Photoluminescence of Fe ²⁺ and Cr ²⁺ ions in ZnSe excited via ionization transitions	12
2.3 Temperature Dependence of the Spectroscopic Parameters in Fe:ZnSe and Cr:ZnSe Mid-IR Gain Elements	14
2.4 Gamma radiation-enhanced thermal diffusion of iron ions into II-VI semiconductor crystals	20
2.5 Enhancement of Cr in II-VI Crystals via Annealing in co-annealing in vapor of Zn	31
2.6 Diffusion of transition metal ions in II-VI semiconductors (Theoretical and computational approaches)	35
2.7. TM Diffusion under Hot Isostatic Pressing.....	46
3. Diffusing doped RE:II-VI materials	53
3.1. Spectroscopic characterization of Pr ³⁺ :ZnSe crystals fabricated via post growth thermal diffusion.....	53
3.2 Diffusion doped Er:ZnS and Er:ZnSe laser active powders	55
4. Electrically pumped transition metal doped II-VI semiconductor materials.....	57
4.1 Electrical Characterization And Electroluminescence Of Thin Film Structures	57
4.2 Electroluminescence in Thin Film Structures Containing Cr ²⁺ :ZnSe Layer	69
4.3. Electrical Characterization of bulk Cr(Fe):ZnSe Laser Active Materials	73
4.4. ectrical characterization TM:ZnSe samples at high temperatures	75
4.5 Ohmic Contact Formation in Al:Cr:ZnS(Se) crystals.	77
4.6 Mid-IR Electro Luminescence of n-type Cr:ZnSe Crystal.....	78
5. Optical parametric oscillation in random medium.....	80
6. Conclusions	81
7. REFERENCES.....	83

1. Introduction

Interest in laser sources operating in the middle-infrared (mid-IR) 2-20 μm region of the electromagnetic spectrum has been constantly growing in the recent decades. The reason for such ubiquitous attention towards these materials arises from a wide variety of applications, made possible by existence of strong and unique absorption features of organic molecules in this spectral range. Applications include molecular spectroscopy, non-invasive medical diagnostics, laser surgery, tissue ablation, processing of polymers, industrial process monitoring, and many others. Also, mid-IR lasers are highly promising for defense related applications such as, standoff detection of explosives and other hazardous materials, aircraft countermeasure systems, and combat identification systems. Moreover, existence of three major windows of transparency of atmosphere in the mid-IR spectral range makes mid-IR lasers attractive for free space communication, environmental monitoring, and remote sensing applications. Mid-IR wavelengths are usually generated using relatively complex nonlinear optical conversion techniques or by means of direct generation in hetero-junction lead-salt, antimonide, or quantum cascade semiconductor lasers, as well as transition metal (TM) doped II-VI semiconductor lasers. Major attention is focused on the latter type of mid-IR lasers, based on Fe:ZnSe/S and Cr:ZnSe/S, due to their favorable properties that enable modes of operation far exceeding the other types of mid-IR lasers, in the 1.8-6 μm range. The II-VI host materials feature heavy ions, this decreases the cut-off frequency of the optical phonons, and decrease the probability of non-radiative decay in the dopant ions. Small crystal field splitting energy associated with the tetrahedral coordination of the II-VI host materials positions intrashell transitions of the TM ions in the mid-IR spectral region. Their wide band gap and transparency in the mid-IR is another key feature of this materials. These materials feature favorable spectroscopic properties such as, a four-level energy structure, an absence of excited state absorption, broad absorption bands overlapping with many convenient fiber laser sources, vibronically broadened emission bands enabling wide tunability. Moreover, reliable and cost-effective fabrication technology of post-growth thermal diffusion doping of these materials has been developed, which allows fabrication of large scale uniformly doped crystals, with preassigned dopant concentrations, and low optical losses. Lasers based on this technology world-record output characteristics such as, high output power of over 140 W, high energy of over 1.1 J, narrow linewidth of <100 kHz, and fs-pulses of 30 fs have been demonstrated. Rare Earth (RE) ions constitute another promising class of optically active centers for mid-IR lasers. Moreover, co-doping of TM and RE ions can be useful for energy transfer from TM to RE and vice versa, extending the range of possible optical pumping sources and enabling direct electrical

pumping. Despite the maturity of post growth thermal diffusion doping of II-VI materials by TM ions, difficulties associated with doping of certain TM ions (e.g. Fe in ZnS) and RE ions still exist. To date pumping sources for TM doped II-VI materials has been limited to optical sources. However, TM doped II-VI media, having wide band gap, hold potential for direct electrical excitation. This type of electrically pumped mid-IR lasers based on TM doped II-VI structures have not yet been demonstrated in the literature. In this effort studies on novel TM:II-IV, TM:TM:II-VI, RE:II-VI materials were performed. Studies included dopant ion diffusion enhancement under γ -irradiation from ^{60}Co source, by diffusion under extreme temperatures and pressures (Hot Isostatic Pressing-HIP), as well as in overpressure of other diffusion assisting ions. Another major part of this work was to develop a pathway for achieving mid-IR lasing under direct electrical excitation. In this part, studies on electrical conductivity of II-VI materials n-type doping with preservation of optically active dopants (TM ions) as well as preservation of minimal optical losses in the mid-IR were carried out.

2. Novel diffusion doped mid-IR laser active materials

2.1 Crystal Field Engineering of Transition Metal Doped II-VI Ternary and Quaternary Semiconductors for Mid-IR Tunable Laser Applications

Introduction

Regardless of the progress in mid-IR TM doped II-VI crystals and lasers several important issues are still outstanding. One of them is covering spectral gap between the oscillation band of the chromium and iron doped materials, $\sim 3\text{-}4\ \mu\text{m}$. The tunability of chromium and iron doped Zn-chalcogenides stretches over $1.9\text{-}3.3$ and $3.5\text{-}5.1\ \mu\text{m}$ spectral ranges, respectively. Therefore, the development of new lasers materials with a maximum emission cross-section between 2.9 and $3.5\ \mu\text{m}$ is essential to cover this gap. The second important research thrust is to extend tunability of TM:II-VI solid state lasers to longer wavelengths with a strategic goal to cover $1.9\text{-}10\ \mu\text{m}$ spectral range. Another critical issue is to control the absorption band spectral position of iron doped II-VI laser crystals. Several iron doped materials (for example Fe:CdMnTe [1]) are promising candidates for room-temperature (RT) lasers with tunability up to $6\ \mu\text{m}$, however these crystals require $3.5\ \mu\text{m}$ pump source. There are no convenient direct laser sources around this wavelength at the moment, therefore a shift of the absorption band to the shorter wavelength will allow using conventional $2.9\ \mu\text{m}$ Er:YAG laser as a pump source. A study of crystal field engineering of TM doped II-VI ternary and quaternary semiconductors for mid-IR tunable laser applications is reported. To reduce the time and cost of ternary and quaternary sample fabrication an

approach based on synthesis of novel TM doped ternary and quaternary powders by thermal annealing was used. These powders were fabricated by mechanically mixing commercially available precursor binary II-VI powders with grain sizes approximately 5-10 μm in desired stoichiometry along with appropriate dopant (e.g. ZnS, ZnSe and FeSe powders). These powder mixtures were then sealed in quartz ampoules and evacuated to 10^{-3} Torr and annealed at temperatures from 850-1000 $^{\circ}\text{C}$ for several days.

Experimental setup for luminescence studies

Figure shows the experimental setup for photoluminescence (PL) and kinetics measurements. Sample powders were sealed in ZnSe cuvettes and placed into a helium closed-cycle cryostat (Janis Research Co., Inc., Model CCS-450). The ${}^5\text{E} \leftrightarrow {}^5\text{T}_2$ transition in the powders was directly excited by the radiation from an electro-optically Q-switched Er:YAG or Er:Cr:YSGG laser operating at 2.94 μm and 2.79 μm , respectively, directed into the cryostat. Q-switched pulses had 100 ns duration and pulse energy of 10 mJ in single pulse operation.

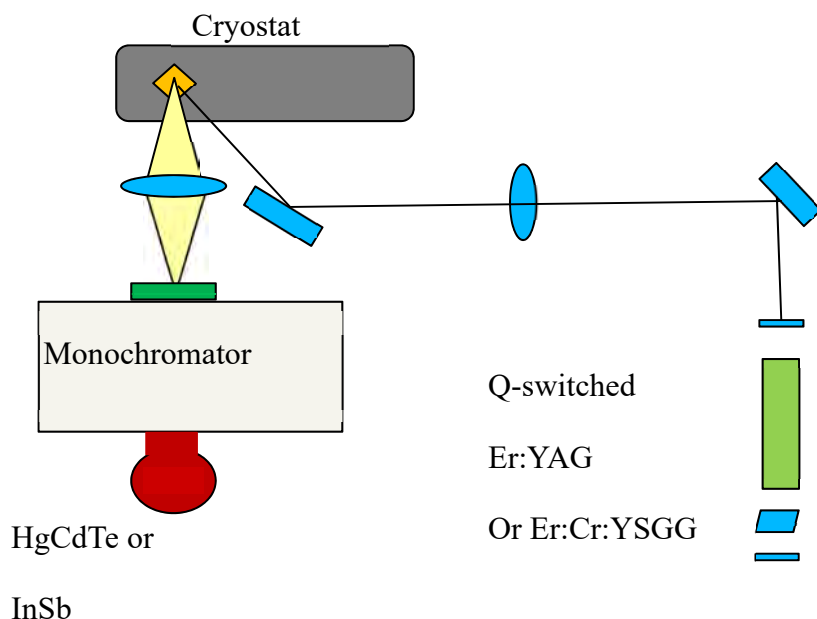


Figure 2.1.1. Platform for photoluminescence and kinetics measurements.

The cryostat was evacuated to 10^{-6} Torr and photoluminescence was collected by a CaF_2 lens through a monochromator (Acton Research ARC-300i). PL spectra were measured with a liquid nitrogen cooled HgCdTe detector (EG&G Optoelectronics J15D14-M200-S01M-10-WE) acquired with a boxcar integrator (Standard Research Systems Models SR250), and kinetics were measured with a liquid

nitrogen cooled InSb detector (EGG Judson J10D-M204-R04M-60) coupled to an amplifier (Perry PA050) (rise-time 300 ns) or thermoelectrically cooled HgCdZnTe (PVI-3TE-6-1, VIGO systems) with a ~ 10 ns response time. Kinetics were measured at temperatures from 13K to room temperature.

Kinetics of luminescence

The intensity of PL was also measured in the time domain at temperatures ranging from 13-298 K in order to determine temperature dependence of the lifetime of the excited state and from these measurements, estimate the radiative lifetimes of these novel materials. Samples measured included Fe:CdTe, Fe:Cd_{0.75}Mn_{0.25}Te, Fe:Cd_{0.75}Mn_{0.25}Se, Fe:Zn_{0.5}Cd_{0.5}Te, and Fe:ZnSe. **Error! Reference source not found.** 2.1.2 shows the low temperature kinetics of Fe:CdTe (curves i, ii), Fe:ZnCdTe (curves iii, iv), and Figure shows low temperature kinetics of Fe:CdMnTe (curves v, vi) and Fe:CdMnSe (curves vii, viii). Fe:CdTe kinetics show some non-exponential behavior in the beginning and this effect is even more pronounced in Fe:ZnCdTe, however this kinetics asymptotically approach exponential over a short time, so lifetimes can be measured by the tail-fitting method. This asymptotic approach to exponential decay suggests that the mechanism at work is non-radiative energy migration between Fe ions becoming more prominent at low temperatures [2]. One can see that the lifetime of Fe:CdTe does not change significantly between 40 K (68 μ s) and 14 K (75 μ s), therefore it can be assumed that at low temperature, quantum efficiency approaches 100% and that these lifetimes approximately equal the radiative lifetime. Likewise, the lifetime of Fe:ZnCdTe shows little change between 40 K and 14 K and the decay rate is nearly the same as that of Fe:CdTe. However, in the case of Fe:CdMnTe and Fe:CdMnSe, the low temperature lifetimes are still changing between 45 K and 13 K, indicating that quantum efficiency does not reach 100% at 13 K. This may indicate that there may still be strong quenching at low temperature as has been observed in Fe:ZnS which has a lifetime of approximately 5 μ s while radiative lifetime was estimated to be 55 μ s by quantum efficiency measurements [3]. This shortening of lifetime is possibly due to non-radiative quenching [4]. The quenching observed in Fe:CdMnTe may be primarily concentration dependent as [5] reported PL lifetimes which were stable from 13 K to 75 K in a bulk crystal sample.

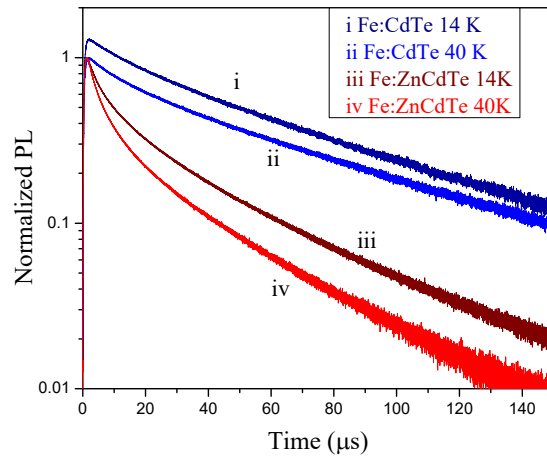


Figure 2.1.2. Low temperature kinetics of luminescence for Fe: CdTe (i, ii) at 14 K and 40 K respectively, and Fe: ZnCdTe (iii, iv) at 14 K and 40 K respectively.

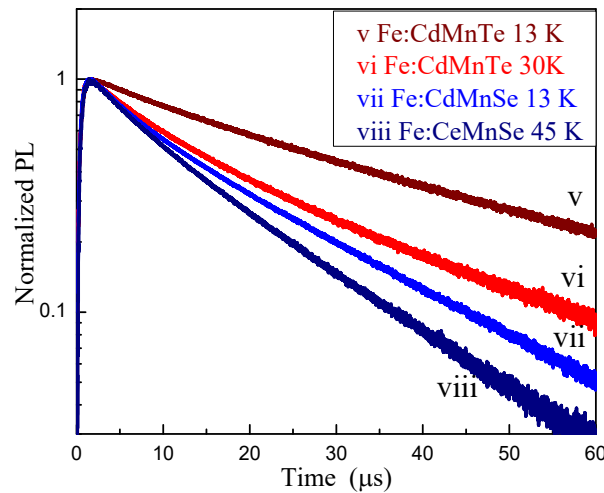


Figure 2.1.3. Low temperature kinetics of luminescence for Fe: CdMnTe (v, vi) at 13 K and 30 K respectively, and Fe: CdMnSe (vii, viii) at 13 K and 45 K respectively.

Photoluminescence spectra

Figure . shows the Photoluminescence spectra of Fe: Cd_xMn_{1-x}Se for x=0, 0.25, and 0.5. One can clearly see in the Figure that the introduction of Mn causes a shift in the maximum emission wavelength toward longer wavelengths, and that this effect is enhanced as more Mn is added. In addition, there is an overall broadening of the emission band with the increase of disorder in the crystal as has been observed previously in Cr: ZnS_xSe_{1-x} [4].

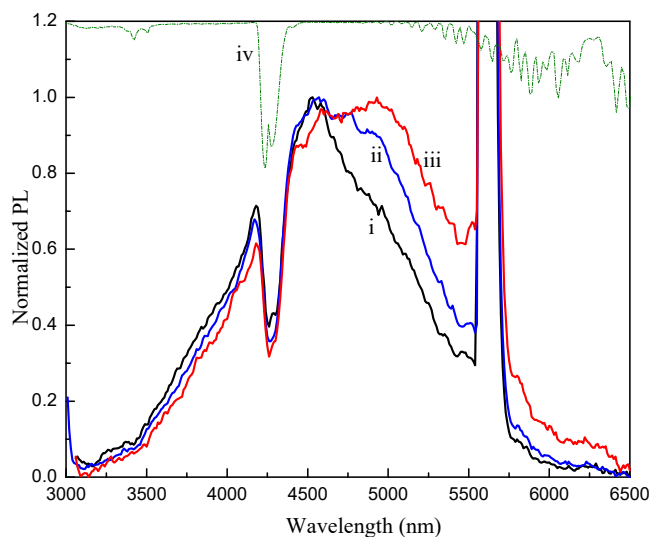


Figure 2.1.4. Non-calibrated photoluminescence spectra of i) Fe:CdSe, ii) Fe:Cd_{0.75}Mn_{0.25}Se, and iii) Fe:Cd_{0.5}Mn_{0.5}Se shown with iv) characteristic atmospheric absorption. The large spike centered near 5.6 μm is an artifact of the monochromator caused by the residual second order diffraction of the pump wavelength of 2.79 μm which was transmitted through the 3 μm filter.

The photoluminescence spectra for Fe:Cd_xMn_{1-x}Te are shown in Figure 15. for x=0, 0.25, and 0.5 measured after a 3.5 μm filter. Here again the same trend can be seen. Additional Mn causes a broadening of the emission band and a shift of the PL toward longer wavelengths. However, in these compounds, the effect is less pronounced than it is in the CdSe-based compounds and the changes in the PL spectra are closer to the level of error in the measurement method.

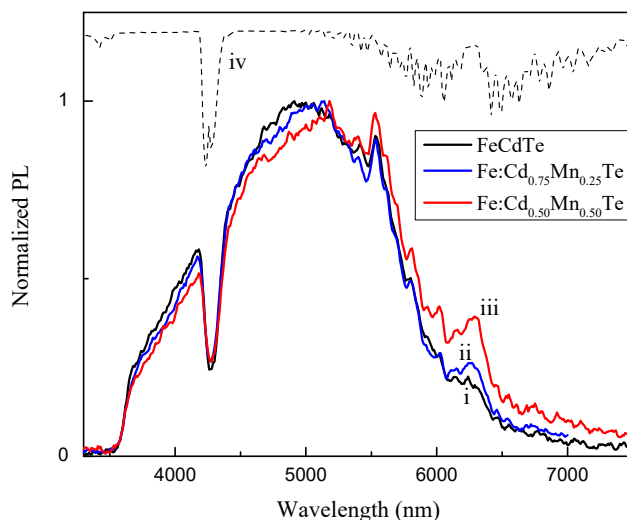


Figure 1 Non-calibrated, normalized PL spectra of i) Fe:CdTe, ii) Fe:Cd_{0.75}Mn_{0.25}Te and iii) Fe:Cd_{0.5}Mn_{0.5}Te powders annealed at 925 $^{\circ}\text{C}$ measured after a 3.5 μm filter, shown with iv) characteristic atmospheric absorption features. The apparent peak near 6.3 μm is caused by a window of transparency in the absorption of atmospheric water.

Results and discussion

These disordered II-VI materials are very promising for active gain media for use in tunable lasers operating over wavelengths longer than 5 μm . The shape and magnitude of emission cross-sections for Fe:Cd_{0.5}Mn_{0.5}Te, Fe:Cd_{0.75}Mn_{0.25}Se, and Fe:Zn_{0.5}Cd_{0.5}Te were estimated using the Füchtbauer-Ladenburg equation,

$$\sigma_{em}(\lambda) = \frac{\lambda^5 I(\lambda)}{8\pi cn^2 \tau_{rad} \int I(\lambda) \lambda d\lambda}$$

where $\sigma_{em}(\lambda)$ is the emission cross-section, λ is emission wavelength, $n=2.7$ is the refractive index, c is the speed of light, τ_{rad} is the radiative lifetime, and $I(\lambda)$ is the emission spectrum calibrated with respect to the detection platform.

In low-doped Fe:ZnSe, radiative lifetime was measured at low temperature to be approximately 55 μs and Fe:ZnS was estimated [6] to have a similar lifetime of 50 μs .

Fe:CdTe shows a stable lifetime below 40 K of around 72 μs which is close to the lifetime of Fe:CdMnTe of 77 μs reported in [7]. Therefore, in calculations for CdTe-based compounds, radiative lifetimes of ~ 72 μs were used. In the case of Fe:CdMnSe, measured lifetimes at low temperature were still strongly quenched, and without more extensive quantum efficiency studies of low-doped samples, it is difficult to pinpoint the radiative lifetime, however it is reasonable to assume that the radiative lifetime for Fe:CdSe-based compounds would fall within the range of those of Fe:ZnSe and Fe:CdTe compounds. Therefore, for these calculations, the range 55-77 μs was used as limits on radiative lifetime of Fe:CdMnSe. The calculated normalized gain profiles are shown in **Error! Reference source not found.**1.6.

As the Figure shows, these materials effectively cover the 3-8 μm range, each with broad tunability and absorption at 2.9 μm .

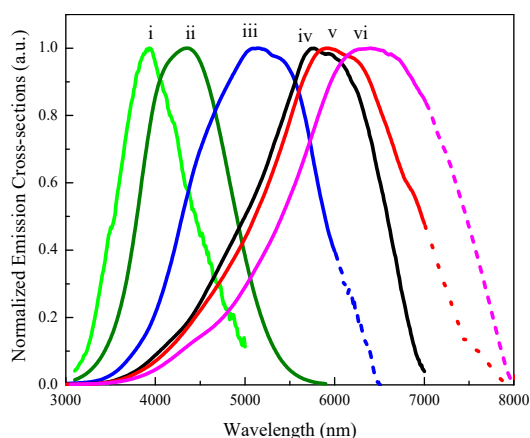


Figure 2.1.6. Normalized room-temperature cross sections of emission of i) Fe:ZnS, ii) Fe:ZnSe, iii) Fe:Cd_{0.75}Mn_{0.25}Se, iv) Fe:CdTe, v) Fe:Zn_{0.5}Cd_{0.5}Te, and vi) Fe:Cd_{0.5}Mn_{0.5}Te

Table 2.1 lists the estimated lifetimes at RT and radiative lifetimes and values for maximum cross-section of emission, spectral position of maximum gain, and full width half maximum of gain profiles calculated using these radiative lifetimes.

Table 2.1 Spectroscopic properties measured for materials prepared for this study

Material	$\sigma_{em} \text{ max (cm}^{-1} \times 10^{-18})$	λ_{max} (μm)	$\Delta\lambda$ (μm) FWHM	τ_{RT} (ns)	τ_{rad} (μs)
Fe:ZnS	1.1	3.94	0.9	50	55
Fe:ZnSe	1.1	4.35	1.1	350	57
Fe:CdTe	1.4	5.73	1.4	240	67
Fe:Cd _{0.75} Mn _{0.25} Se	1.2-0.9	5.06	1.5	<50	55-77
Fe:Cd _{0.5} Mn _{0.5} Se	1.3-1.0	5.50	1.8	<50	55-77
Fe:Cd _{0.75} Mn _{0.25} Te	1.2	5.94	2.0	188	77
Fe:Cd _{0.5} Mn _{0.5} Te	1.4	6.40	2.1	188	77
Fe:Zn _{0.5} Cd _{0.5} Te	1.2	5.86	1.3	193	~70

Conclusions

We demonstrate the effective use of crystal field engineering to fabricate new ternary and quaternary disordered crystals to tune emission bands to overlap with parts of the mid-IR spectral region not currently covered by available solid-state lasers while maintaining absorption bands

which coincide with readily available pump sources. An inexpensive, simple technique was developed for prototyping and characterizing novel ternary and quaternary doped II-VI crystals in powder form without the need for a crystal growth stage. Using this process, several new and promising laser gain media were fabricated, and measurements of kinetics of luminescence and cross-sections of emission were made and listed here in Table 2.1 [5].

These results indicate that, when grown in bulk, these will be a very promising gain media for broadly tunable laser sources operating over the 3-7.5 μm spectral range [6, 7].

2.2 Mid-IR and Near-IR Photoluminescence of Fe²⁺ and Cr²⁺ ions in ZnSe excited via ionization transitions

Lasers utilizing chromium and iron doped II-VI media currently employ direct optical excitation of mid-IR ${}^5E \leftrightarrow {}^5T_2$ laser active transitions with absorption wavelengths of Cr²⁺ and Fe²⁺ centered at 1.8 μm and 3 μm , respectively. Use of the optical excitation into charge transfer band could not only enable a new type of optical pumping of these lasers but also improve the understanding of processes that could lead to the development of solid-state lasers with electrical excitation. In this paper we studied kinetics of the photoluminescence (PL) at near-IR transitions from the meta-stable 3T_1 level and mid-IR transitions between ${}^5E \leftrightarrow {}^5T_2$ under visible excitation into the charge transfer band.

Experimental results and discussion

The TM doped II-VI samples used in this research were fabricated by post-growth thermal diffusion of impurity ions in polycrystalline II-VI. Parameters of the thermal diffusion process (time, temperature) were optimized for each combination of host and impurity to produce minimal distribution gradient and maintain high crystal quality.

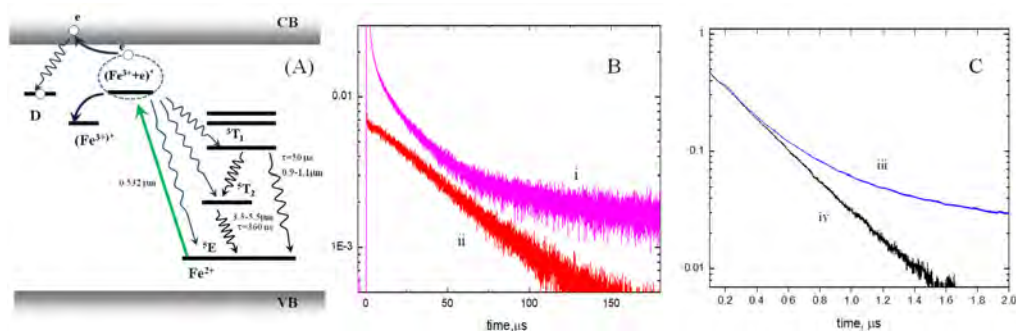


Figure 2.2.1. A. Energy levels of Fe²⁺ and energy transfer mechanisms. B. RT long PL kinetics of Fe:ZnSe showing i) mid-IR kinetics under 532nm excitation and ii) near-IR PL at 950nm. C. RT short PL kinetics of Fe:ZnSe under iii) 532nm excitation and iv) 2780nm excitation.

In the Fe²⁺ energy level structure (see Figure 2.2.1.A) the 5D ground state is split in the tetrahedral crystal field (Td) of ZnSe crystals into the doublet 5E (ground state) and triplet 5T_2 , (first excited state). Mid-IR luminescence and absorption are a result of this ${}^5E \leftrightarrow {}^5T_2$ laser active transition. Excitation by visible radiation into the charge transfer band results in the formation of $(\text{Fe}^{3+} + e)^*$ which can then relax using several channels including direct fast non-radiative relaxation to 5T_2 level and/or cascade relaxations via 3T_1 meta-stable level. To study the mechanisms of relaxation, near-IR and mid-IR kinetics were measured at room temperature (RT) (see Figure 2.2.1B, C). In our experiments with detector response $\sim 40\text{ns}$, no rise time was observed. Under 532nm excitation, the short kinetics (curve iii) matches

the decay of Fe^{2+} under intra-band 2780nm excitation (curve iv), which is indicative of fast non-radiative relaxation from excited complexes. However, in the long time-scale (curve i) there is non-exponential relaxation with hundreds of μs time scale. For comparison, the kinetic of PL (curve ii) at ${}^3\text{T}_1 \rightarrow {}^5\text{E}$ transition (950nm) with exponential decay time 50 μs was measured under green excitation at RT. The long luminescence tail of mid-IR PL could be attributed to ionization transitions of iron ions, which has been observed to be tens of seconds at 100K [8].

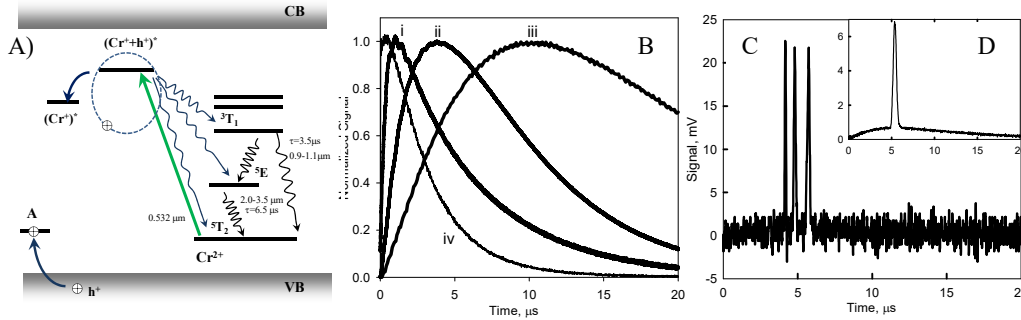


Figure 2.2.2 A. Energy levels of Cr^{2+} and energy transfer mechanisms. B. Normalized RT PL kinetics of Cr:ZnSe illustrating rise time under i) intra-shell excitation at 1560nm, ii) 532nm nanosecond scale excitation, iii) 532nm picosecond scale excitation, and iv) Cr:ZnSe PL kinetics at 960nm under 532nm ns scale excitation. C. Lasing of Cr:ZnSe under 532nm 10ns pulsed excitation showing three pulses under 9.1mJ pump energy. D. Averaged signal under 6.7mJ pump energy.

The energy level structure of Cr^{2+} is similar to that of Fe^{2+} , however the triplet ${}^3\text{T}_2$ is the ground level and the doublet ${}^5\text{E}$ is the first excited state level (see Figure 2.2.2A). We studied the RT PL signal in Cr:ZnSe under 532nm excitation at ${}^3\text{T}_1 \rightarrow {}^5\text{T}_2$ and ${}^5\text{E} \rightarrow {}^5\text{T}_2$ transitions (Figure 2.2.2B). Rise time of mid-IR kinetics show no fast non-radiative relaxation to the upper laser level and exhibit dependence on pump intensity, with a rise time of $\sim 3.5\mu\text{s}$ under 10ns pulse excitation (curve ii) and $\sim 10\mu\text{s}$ under 35ps pulse excitation (curve iii). Kinetics at 950nm (${}^3\text{T}_1 \rightarrow {}^5\text{T}_2$) exhibit strong lifetime quenching from the low temperature value of 1.1ms [9] to a RT value of 2.8 μs (curve iv).

The near-IR emission cross sections from ${}^3\text{T}_1$ levels were estimated to be $0.4 \times 10^{-20} \text{ cm}^2$ and $0.7 \times 10^{-20} \text{ cm}^2$ at RT for Cr^{2+} and Fe^{2+} ions, correspondingly. Analysis of the mid IR luminescence of Fe^{2+} and Cr^{2+} ions in ZnSe under visible excitation allowed us to calculate the excitation efficiency of the upper laser level. The efficiency of the fast non-radiative relaxation to the upper laser level for both ions was measured to be not more than $\sim 2\%$ from absorbed energy of ns excitation pulses. However, due to thermal quenching of the ${}^3\text{T}_1$ level in Cr^{2+} ions, the cascade relaxation over this level exhibits lifetime shorter than that of the upper laser level (6.5 μs) and could therefore enable pumping rate sufficient for laser operation. In our experiments, the mid-IR lasing of Cr:ZnSe under 532nm excitation has been realized with transverse pumping. The results of these lasing experiments are shown in Figure 2.2.2C and

D. The graph insert (Figure 2.2.2D) shows lasing spike slightly above threshold to illustrate the timing of the lasing spike relative to the luminescence. Three laser pulses (Figure 2.2.2C) are visible in the kinetics beginning $\sim 4\mu\text{s}$ after excitation, which are the result of slow accumulation of population in the upper laser level after excitation to higher lying levels.

A similar excitation route via 3T_1 level for Fe^{2+} ions has relaxation time $\sim 50\ \mu\text{s}$ which is significantly longer than the lifetime of the upper level at RT (380 ns). One way to potentially increase efficiency of pumping under visible excitation would be the utilization of cross-relaxation processes in highly doped crystals, which is a subject for future investigation.

2.3 Temperature Dependence of the Spectroscopic Parameters in Fe:ZnSe and Cr:ZnSe Mid-IR Gain Elements

The specific goal of the next section was a study of temperature dependence of absorption band broadening, spectral position, and amplitude of absorption coefficient in Fe(Cr):ZnSe for temperatures ranging from 77-389K. Knowledge about temperature dependence of spectroscopic properties can have many implications. Changes in the absorption spectra at different temperatures could influence on optimization of pump sources for laser system operating at different temperatures. This knowledge is also important to understand influence of the thermal effects on maximum possible output laser power and laser noise.

Experimental setup

Chemical vapor deposition (CVD) grown polycrystalline samples of ZnSe were used. The samples were doped using post growth thermal diffusion method. This process involves deposition of a several hundred nm film of the dopant, Cr or Fe, on the crystal facet and annealing at $T\sim 1000^\circ\text{C}$ in vacuumed quartz ampoules (10^{-5} Torr) for several days. Obtained crystals had a concentration of 4.2×10^{18} and 1.4×10^{18} for Cr:ZnSe and Fe:ZnSe crystals, respectively. In this experiment, absorption spectra were measured at 77K, RT and up to 389K in $\sim 10\text{K}$ increments. Heating of the samples was done using a resistive heater. An empty cryostat was placed into a Shimadzu UV-VIS-NIR- 3101PC (200nm – 3000 nm) spectrophotometer and the baseline was measured. Then, Cr:ZnSe was placed into a cryostat which was vacuumed to 10^{-5} Torr. The cryostat was placed into the spectrophotometer and the transmission spectra were taken. Liquid nitrogen was used to cool down the samples to 77K during the transmission measurement. The same procedure was repeated for the Fe:ZnSe crystal. The absorption of Fe however is near the limit of the UN-VISIR spectrophotometer, so the Fe:ZnSe was also

measured in a FTIR (2000-20000nm) spectrophotometer.

Absorption spectra of Cr:ZnSe samples measured at room temperature and at T=77K are shown in the Figure8.1. The absorption coefficient of Cr:ZnSe at 77K showed an overall increase in the absorption coefficient as well as a shift in the peak to a shorter wavelength in comparison with spectrum measured at room temperature. From these experiments, the position of the absorption peak, the maximum of the absorption coefficient and full bandwidth at half maximum were measured.

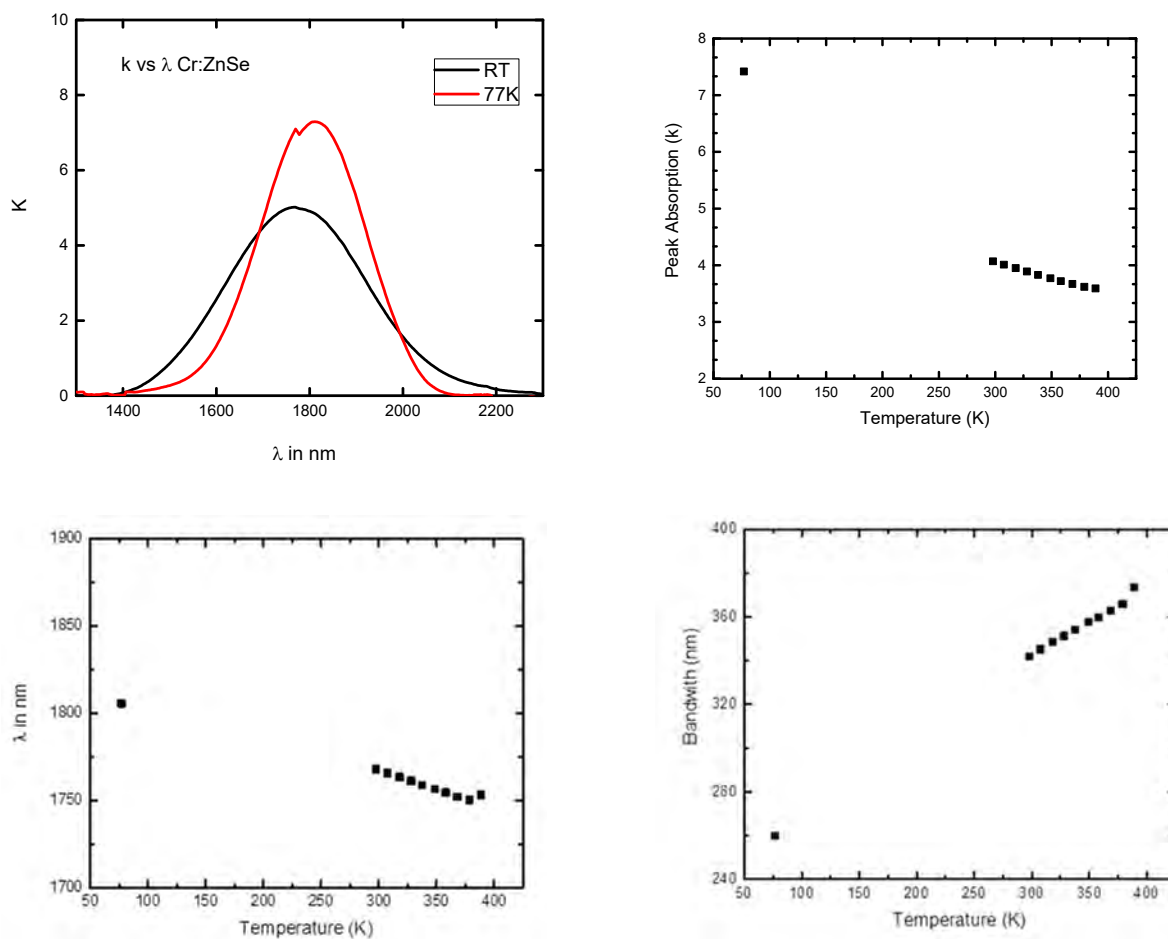


Figure 2.3.1. Absorption spectra of Cr:ZnSe and Fe:ZnSe samples measured at room temperature (black curve) and at T=77K (red curve); Temperature dependence of absorption bandwidth (FWHM); spectral position, and maximum of absorption coefficient in Cr:ZnSe in 77-389K temperature range

Figure 2.3.1 also shows the temperature dependence of absorption band broadening, spectral position, and amplitude of absorption coefficient in Cr:ZnSe in 77-389K temperature range. As one can see, the heating of the crystal from 77K to 389K shifted the absorption peak

from 1806nm to 1753 nm and decreased the overall peak absorption. It also caused the bandwidth to broaden by 113nm. Heating also caused the absorption to increase at the specific wavelength of 1530nm which coincides with the wavelength at which Er fiber lasers operate at.

Figure 2.3.2. shows the difference of the absorption coefficient measured at room and absorption coefficient measured other temperatures within 77K-385K range. One can see that there are two wavelengths where absorption coefficient is approximately constant within the studied temperature range. These two wavelengths are 2040 nm and 1650 nm, respectively. These points are valuable for stable, low noise laser pumping. It should be noted that these wavelengths are close to the lasing wavelength of the Er:YAG and Ho:YAG lasers, which could be used as a pump source. On other hand, the absorption at 1530 and 1830 nm reveals the strongest changes while temperature increases. One can see that the increase of k at 1530 nm from RT to 116°C is 0.29 (cm)^{-1} , which is a significant increase in absorption. This wavelength corresponds to the lasing wavelength of an Er fiber laser. Conversely, one can see that at around 1830 nm, there is a 0.58 (cm)^{-1} decrease in k from RT to 116°C. These strong changes of the absorption could result in nonlinear dependence of absorbed pump radiation on pump intensity. It also could stimulate thermal optical bistability when there are two different steady state values of the absorbed pump power under the same initial conditions of incident radiation.

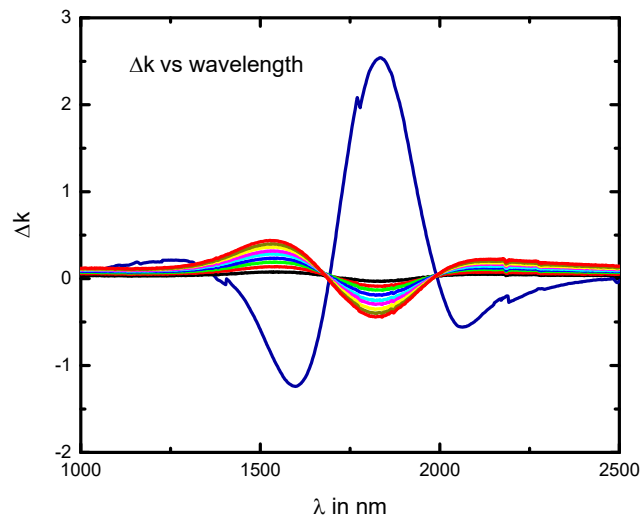


Figure 2.3.2. Change in absorption coefficient ($\Delta k = k_{300K} - k_T$)

The dependence of the absorption cross-sections on temperature is a crucial parameter for

analysis of the thermo-optical characteristics of Cr:ZnSe under pump radiation. Figure 2.3.3. shows the temperature dependence of $|\Delta\sigma|/\sigma_{RT}$ at two wavelengths where the maximum changes in cross section were measured. One can see from the Figure 2.3.3 that the dependences could be fitted by linear equations with slopes:

$$\sigma^{-1} d\sigma/dT = -1.6 \times 10^{-3} K^{-1}$$

for wavelength = 1830 nm

$$\sigma^{-1} d\sigma/dT = 2.9 \times 10^{-3} K^{-1}$$

for wavelength = 1530 nm.

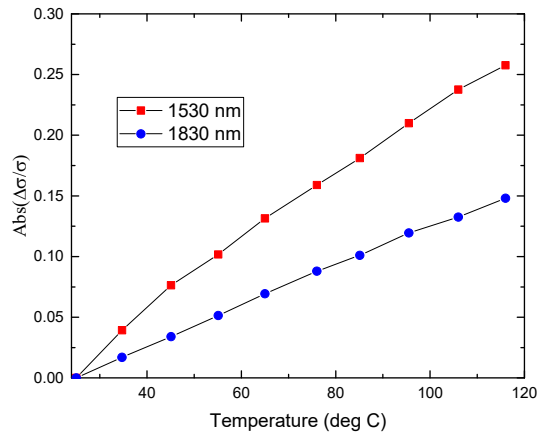


Figure 2.3.3. $|\Delta\sigma|/\sigma_{RT}$ vs temperature for 1530 nm and 1830 nm

The transmission spectrum of Fe:ZnSe crystal in the 5000-2000 nm spectral range with respect to varied temperature is shown in Figure 2.3.4 (left). The absorption band of ${}^5E \leftrightarrow {}^3T_2$ transitions of Fe^{2+} ions in ZnSe crystals has a maximum at 3100 nm. For ease of readability, the difference in absorption coefficient from room temperature to each recorded temperature (denoted Δk) is graphed in Figure 2.3.4 (right) for the 3200-1950 nm range

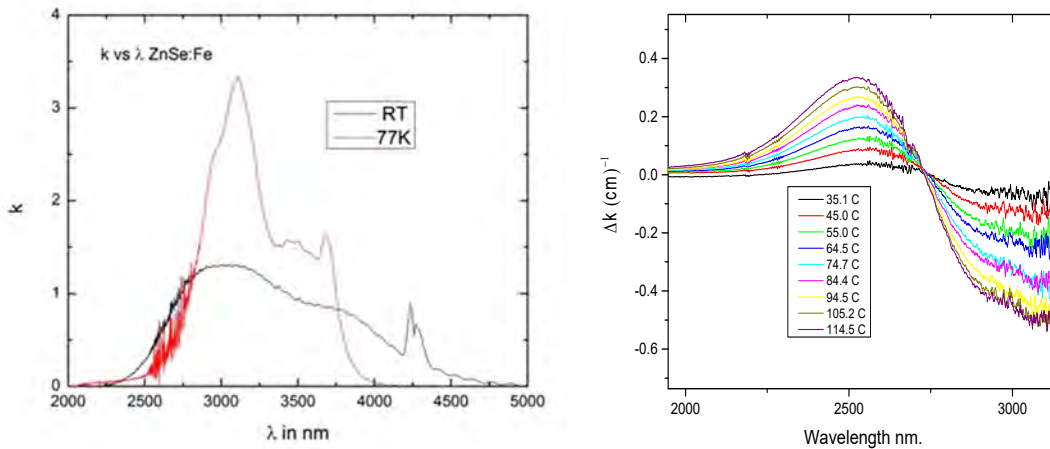


Figure 2.3.4. Right) Absorption spectra of Cr:ZnSe and Fe:ZnSe samples measured at room temperature (black curve) and at T=77K (red curve); Left) Δk vs wavelength for Fe:ZnSe for 3200-1950 nm range with respect to increasing temperature

As one can see, the difference is only relatively large in the 3200-2250 nm wavelength range. Also, the peak width appears to be broadening with increasing temperature, although, as mentioned for transmission we are limited by the spectral range of our spectrophotometer (3.2 μm). One can see that Fe:ZnSe has one wavelength in this spectral range where absorption coefficient remains approximately constant, namely 2730 nm. It is likely that another such point exists at a wavelength higher than 3200nm, but that is past the capability of our spectrophotometer. From the Figure, it is evident that there is a maximum of Δk at 2525 nm (as expected from the graph of k), and the difference of k from RT to 114.5°C at this point is 0.335 (cm)⁻¹. Conversely, at 3.1 μm , we see a decrease in k of around 0.5 (cm)⁻¹ from RT to 114.5°C. k falls to approximately 87% of its room temperature value at this wavelength. The calculated relative change of the absorption cross section at 2525nm was measured to be $\sigma^{-1} d\sigma/dT = 3.5 \times 10^{-3} \text{K}^{-1}$.

In conclusion of this section, it was demonstrated that there are two wavelengths (2040 nm and 1650 nm) where absorption coefficient is approximately constant within the studied temperature range. These wavelengths are close to the lasing wavelengths of the Er:YAG and Ho:YAG lasers. Optical pumping of Cr:ZnSe using the above pump sources should provide

greater stability and lower noise operation than pumping at a different wavelength. On other hand, the absorption at 1530 and 1830 nm reveals the largest change as temperature increases. The temperature changes of the absorption cross sections at these wavelengths were measured to be $\sigma^{-1} d\sigma/dT = -1.6 \times 10^{-3} K^{-1}$ and $\sigma^{-1} d\sigma/dT = 2.9 \times 10^{-3} K^{-1}$ at 1830 nm and 1530 nm wavelengths, respectively. These wavelengths could be used to study thermally induced optical bistability [4]. Under heating from RT to 116°C, the peak of absorption coefficient decreased to 88% of RT absorption and shifted from 1770 nm to 1750 nm.

In Fe:ZnSe, we also observed a decrease in absorption peak to 88% level of the RT value. The maximum temperature change of the absorption coefficient was measured at 2525nm with slope $\sigma^{-1} d\sigma/dT = 3.5 \times 10^{-3} K^{-1}$, while constant absorption was measured at 2730 nm. Using RT absorption spectrum and $g_1/g_2=1$, the radiative life time was calculated to be 17 μs , which is 3.5 times larger than for the Cr^{2+} transition in ZnSe.

2.4 Gamma radiation-enhanced thermal diffusion of iron ions into II-VI semiconductor crystals

Introduction

The diffusion of the TM ions into II-VI semiconductors has been studied for more than 60 years (e.g. [10]). These materials can be reliably produced by post-growth thermal diffusion of TM ions into bulk II-VI crystals [11,12,13,14]. Thermal diffusion is usually realized from the TM film deposited on the crystal surface or from the liquid or vapor phases. In the first case, Cr or Fe films are deposited on a crystal surface using pulsed laser deposition, thermal deposition, or magnetron sputtering. Thermal diffusion is then carried out in sealed ampoules under a vacuum of $\sim 10^{-5}$ Torr at a temperature of 900-1100 °C over 7-20 days. In the liquid phase diffusion, a portion of the crystal is immersed in molten metal during the annealing process. In the vapor phase diffusion method, II-VI samples together with TMs (Cr, Fe, Co, Ni) or TM compounds (CrS, CrSe, FeSe) are placed in the different parts of the ampoules. The ampoules are sealed at low pressure and annealed. The thermal diffusion method takes advantage of available cost-effective technology for chemical vapor deposition (CVD) mass production of low optical loss II-VI infrared polycrystalline windows. In comparison with crystal growth technology, thermal diffusion is very cost-effective, simple, and has been used quite extensively [15].

Currently, the post-growth thermal diffusion of transition metals into II-VI semiconductors allows the inexpensive fabrication of large scale, highly doped Cr:ZnSe and ZnS laser active crystals [16,17]. However, the diffusion rate of iron ions in both ZnSe and ZnS is small enough to make homogeneous doping of large crystals by this method impractical [11,18,19]. This imposes limits on the size of homogeneously doped crystals which can be produced and causes non-uniform doping with large concentration gradients in iron doped crystals. Because the rate of diffusion of metal ions through the lattice of the II-VI crystal is mediated by point defects in the crystal [20,21], increasing the population of point defects during the annealing process by γ -irradiation is a way to increase the rate of diffusion of iron ions into II-VI materials. This study will examine the effect of γ -irradiation during the annealing process on the diffusion rate of iron ions in ZnSe and ZnS.

Previous studies were performed in order to measure the passive losses introduced into II-VI bulk crystals by exposure to γ -irradiation [22]. In these studies, samples of undoped ZnS were irradiated for 18 days at approximately 45 Rad/s by a Co^{60} source. Results of this study showed that after annealing at room temperature for less than an hour, the losses in the absorption spectrum introduced by irradiation returned to the levels similar to those present before exposure to radiation. In the same study, doped Cr:ZnS and Cr:ZnSe crystals were irradiated under the same conditions. These samples were then used as gain media in laser cavities and the slope efficiency of these lasers were compared to the twin crystals not

subjected to irradiation. These experiments demonstrated that no appreciable passive losses were permanently introduced through the irradiation process. So, the conclusion can be made that γ -irradiation from Co^{60} source does not result in formation of stable intrinsic defects in ZnSe and ZnS and, hence, γ -irradiation could be used to enhance the diffusion process of iron.

Gamma-Enhanced Thermal Diffusion Procedure

Polycrystalline bulk ZnS and ZnSe crystals were cut to uniform sizes ($7 \times 7 \times 5$ mm), polished, and cleaned using acetone and methanol in sequence. These crystals then had thin films of iron of thicknesses 300 nm deposited onto a single facet. Next they were sealed in evacuated quartz ampoules at 10^{-3} Torr and installed in a vertical cylindrical furnace custom designed by Thermo Scientific (see Figure 2.4.3) for the experiments at irradiation facility of Edmund C. Leach Nuclear Center at Auburn University (see Figure 2.4.4). This furnace was brought up to annealing temperature, and then ^{60}Co rods were raised to surround the furnace for the duration of the annealing process. The samples were annealed for 14 days at 950 °C under γ -irradiation from ^{60}Co source with irradiation dose rate of 44 R/s. Samples accumulated a total dose of 50-90 MRad. For comparison, identical samples were also annealed in evacuated quartz ampoules in identical furnace without irradiation at the same temperature for the same duration. After annealing, the crystals were removed from quartz ampoules and polished on facets parallel to the direction of metal ion diffusion.



Figure 2.4.3. Two custom made furnaces designed by Thermo Scientific for γ -enhanced thermal diffusion experiments. The furnaces were able to operate long-term under γ -irradiation at temperatures up to 1000 °C and accepted up to $20 \text{ } \phi 9 \times 50$ mm ampoules.

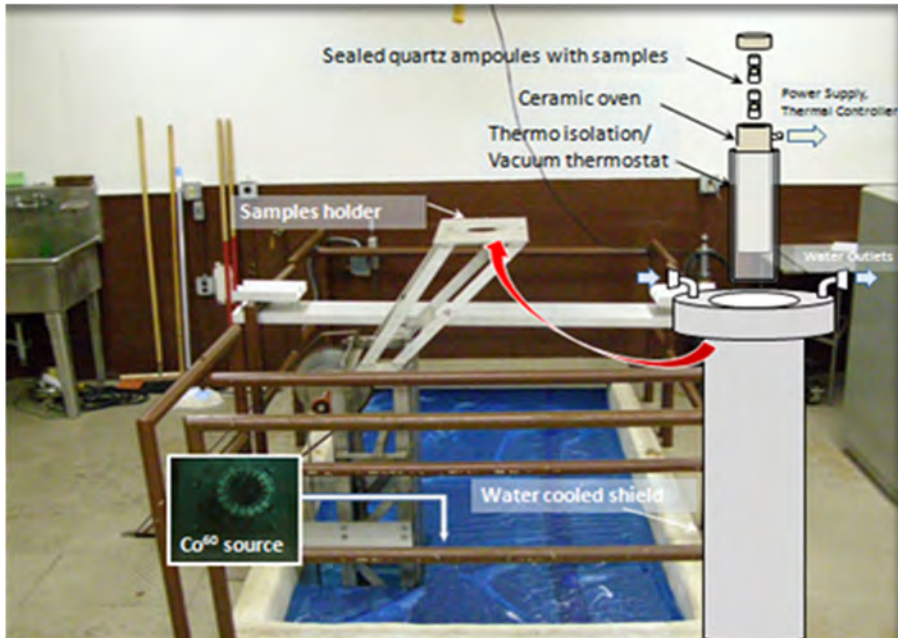


Figure 2.4.4. Sketch of experimental set-up for γ -assisted diffusion of TM ions in II-VI semiconductors at Edmund C. Leach Nuclear Center at Auburn University

Gradient Measurement Experimental Methods

After diffusion, the concentration gradients of iron ions in crystals were measured directly by the measuring the absorption of iron with respect to position within the crystal. An experimental set-up for concentration gradient measurement is depicted in Figure 2.4.5.

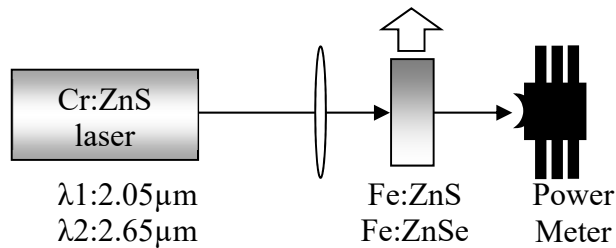


Figure 2.4.5. Platform for measuring concentration gradient. Emission from a tunable Cr:ZnS laser is focused by a CaF_2 lens. The sample is translated through the focus and transmitted power is recorded as a function of sample position.

A specially designed tunable laser based on Cr:ZnS pumped by an Er: fiber laser (ELR-20-1532, IPG Photonics Corporation) (see Figure 2.4.6) was used as a source. Polycrystalline Cr:ZnS gain element ($2 \times 4 \times 9 \text{ mm}$, $N_{\text{Cr}} = 6.1 \times 10^{18} \text{ cm}^{-3}$) with AR coating over 1530-1570 nm and 2000-2700 nm spectral range was placed in the cavity at normal incidence. Pumping was done through dichroic, folded, plane-plane input mirror transmitting pump radiation and highly reflective over 2000-2700 nm range and intra-cavity AR coated bi-convex CaF_2 lens with a focal distance of 20 mm and positioned at ~ 19 mm from the front

facet of the gain element. A second identical intra-cavity lens was installed at ~ 19 mm from the rear facet of the gain element and was used for the overall cavity stability and proper operation of 600 grooves/mm grating placed at Littrow configuration. The output coupler was a plane-plane mirror with reflectivity of 50% over

2000-2700 nm spectral range installed in a folded configuration forming an angle of 15° between the direction of the output and pump beams.

Cr:ZnS laser radiation was focused through a CaF_2 lens of 150 mm (or 75 mm) focal length and directed into a power meter. The laser beam diameter was measured by the knife edge method at several points in order to accurately model the location and size of the beam waist (Figure 2.4.7).

The minimum beam diameter was measured to be approximately $109 \mu\text{m}$ with a Rayleigh length of 3 mm. For higher resolution measurements, the beam was expanded before the focusing lens to reduce the beam waist to approximately $78 \mu\text{m}$ and a Rayleigh length of 2 mm. The estimated M^2 parameter of the beam was 2.4 according to the equation

$$\omega(z) = \omega_0 \sqrt{\left(\frac{z\lambda M^2}{\pi\omega_0^2}\right)^2 + 1}$$

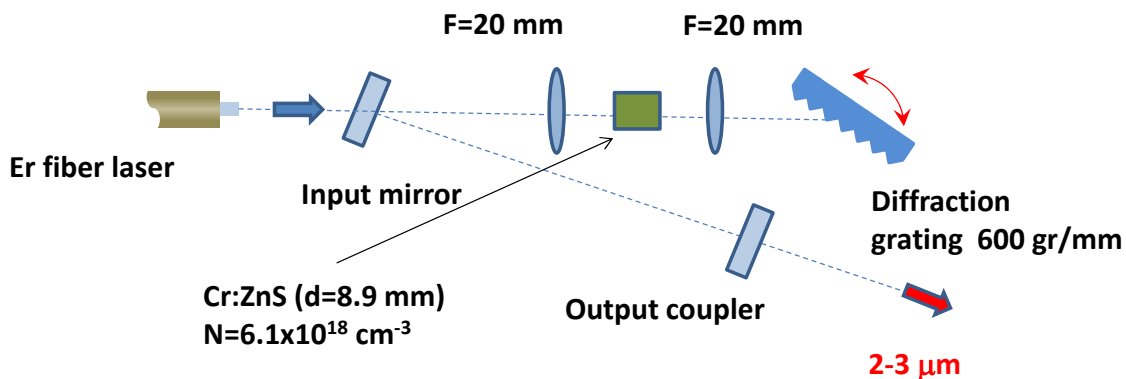


Figure 2.4.6. Tunable Cr:ZnS laser designed for measurement of iron gradients in II-VI crystals.

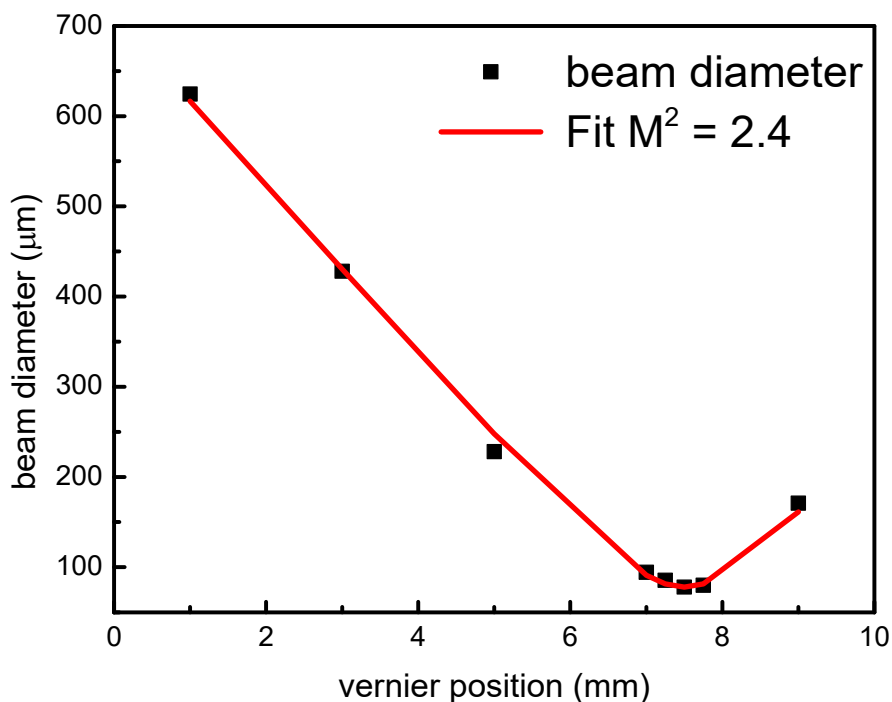


Figure 2.4.7. Beam waist profile of expanded beam focused by 150 mm focal length lens, shown as beam diameter as a function of position along the optical axis and a fit of a beam profile with $M^2=2.4$.

The Cr:ZnS laser emission was tuned to 2637 nm to overlap with Fe^{2+} absorption (see Figure 2.4.8) and the Fe-doped samples were translated across the focus of the beam in the direction of iron diffusion while the transmitted power was recorded in order to measure the active and passive losses together. Then the laser was tuned to 2048 nm, outside the absorption band of Fe in II-VI (see Figure 2.4.8), in order to measure passive losses alone so that they could be eliminated in calculation of Fe gradient profile.

The normalized transmitted power of 2038 nm and 2637 nm are plotted with respect to distance from the coated crystal facet of one of the studied Fe:ZnSe samples is depicted in Figure 2.4.9. The pronounced drop in power near the 0 mm and 5.3 mm marks are caused by the shadowing of the beam by the unpolished surfaces. Examples of crystals which were laser scanned are shown in Figure 2.4.10 (Fe:ZnS) and Figure 2.4.11 (Fe:ZnSe). The deviation of the 2637 nm curve from the 2038 nm curve near the edges can be attributed to iron absorption. By taking the ratio of these measurements, it is possible to normalize the transmitted signal to account for Fresnel losses and polishing quality of the crystal surfaces.

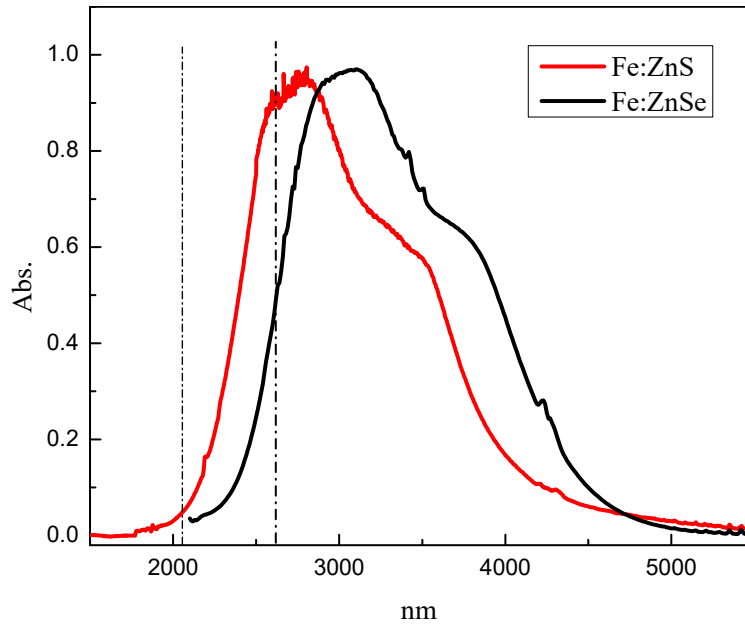


Figure 2.4.8. Absorption bands of Fe:ZnS and Fe:ZnSe shown with the wavelengths of the Cr:ZnS laser which were used to measure passive (2048 nm) and active (2637 nm) losses

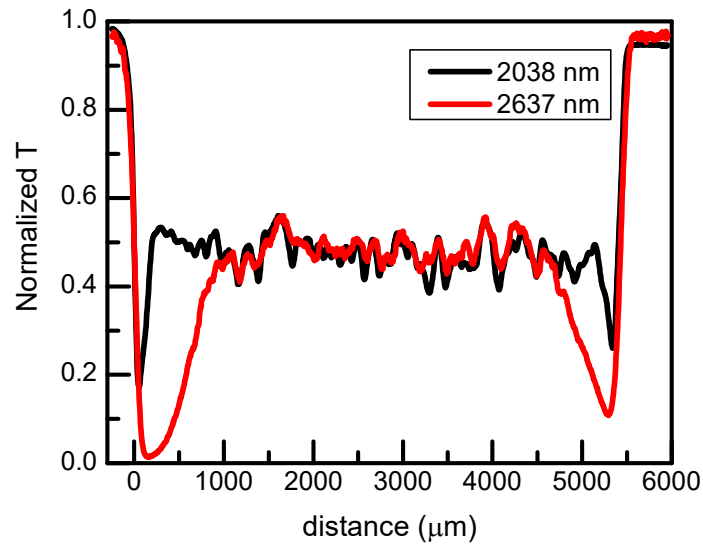


Figure 2.4.9. Normalized transmission of 2038 nm and 2637 nm laser emission vs. distance from crystal facet of Fe:ZnSe crystal of length 5.3 mm.



Figure 2.4.10. Fe:ZnS crystals (2×5×7 mm) annealed at 950 °C for 14 days under 44 Rad/s (left) and 0 Rad/s (right).

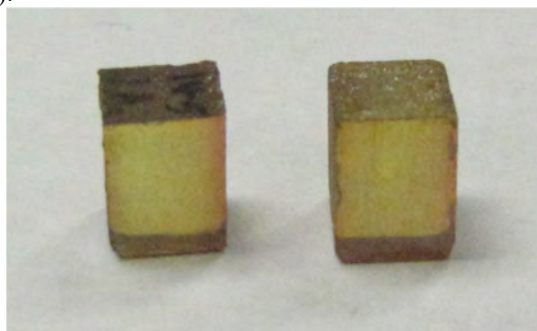


Figure 2.4.11. Fe:ZnSe crystals (5×5.3×7 mm) annealed at 950 °C for 14 days under 44 Rad/s (left) and 0 Rad/s (right).

The accuracy of this laser scanning technique was verified by a second gradient measuring technique. The total absorption spectrum was measured by FTIR parallel to the direction of iron diffusion. From this spectrum, absorption coefficients (I/I_0) at 3048 nm and absorption coefficient ($\sigma_{abs}N$) were calculated using Beer-Lambert Law,

$$I = I_0 e^{-\sigma_{abs}Nl}$$

where I_0 is intensity of light incident on the crystal, I is transmitted intensity, σ_{abs} is the cross-section of absorption and N is the average concentration of dopant and l is the path length through the crystal. This measurement integrated concentration through the whole length of the crystal, but from this, total concentration of iron could be determined. Then a thin layer (~10-20 μm) was polished off of the facet onto which iron had been deposited. The absorption measurement was then repeated as shown in Figure 2.4.12 and in this way the amount of iron, N , in the removed layer could be determined. This process was repeated iteratively until a profile of the concentration gradient could be plotted.

The gradient profiles measured with each technique were compared as shown in Figure 2.4.13. The data points indicated with x's were measured by the laser scanning technique detailed above. The solid line shows the absorption coefficients calculated according to Fisk's Laws of diffusion using parameters

obtained by fitting a Gaussian curve predicted to absorption coefficients at 3048 nm measured using the incremental polishing method. As can be seen in the Figure 2.4.10, these methods show very good agreement.

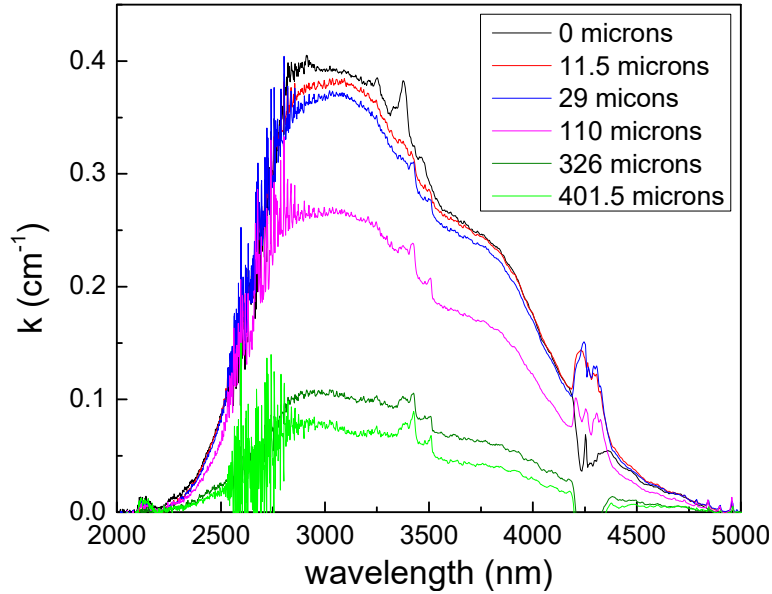


Figure 2.4.12. Absorption coefficient spectra after repeated polishing measured after 11.5 μm , 29 μm , 110 μm , 326 μm , and 401.5 μm of material was removed. The narrow features near 3500 nm and 4500 nm are artifacts from water and CO_2 absorption.

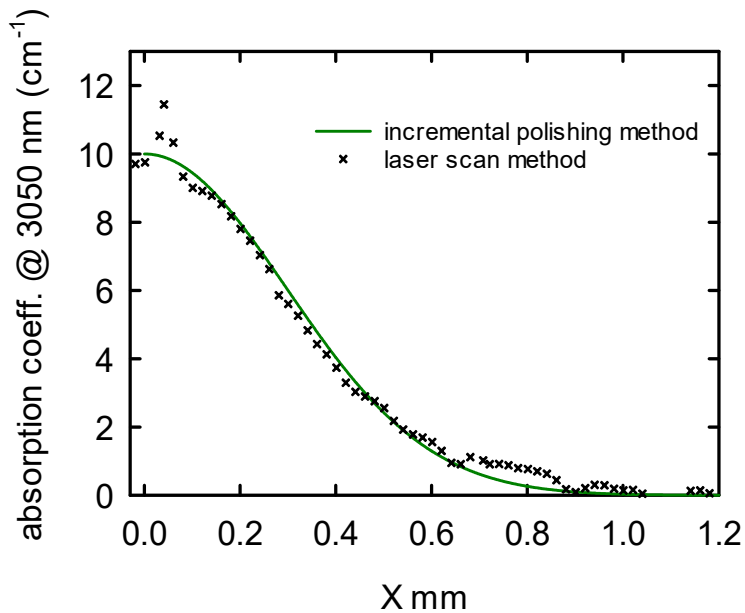


Figure 2.4.13. Gradient profile of a sample measured by laser scan (x's) and incremental polishing method (solid line). The spike around 0.05 mm is most likely an artifact caused by the shadowing of the unpolished edge.

Results and Discussion

Figure 2.4.14 shows the absorption coefficient as a function of distance from the edge of the crystal for irradiated (dashed curve) and non-irradiated (solid curve) samples of Fe:ZnSe measured by the tunable laser scanning technique. Crystals were scanned starting at the facet onto which the iron thin film had been deposited. One can see from the relative magnitudes of the optical densities near the leading edge that a larger concentration of iron diffused through the thin film interface of the crystal which was annealed under γ -irradiation. During the annealing process, some of the iron film sublimates and a portion of this iron vapor may diffuse into other surfaces of the crystal. This process accounts for the second peak in iron concentration at the opposite facet of the crystal near the 5000 nm mark. These results also show that in the sample annealed in the absence of γ -irradiation, a greater amount of iron diffused from the vapor phase. This may indicate that in the case of radiation-enhanced diffusion, the metal in the thin film was induced to diffuse through the crystal surface more quickly, thus allowing less iron to sublimate and maintaining a higher concentration of iron near the surface where the thin film had been deposited. It is possible that the diffusion length in this case may have been even further enhanced if the film had been thicker and thus the supply of iron had not been exhausted as quickly.

Figure 2.4.15 shows normalized absorption coefficient as a function of distance from the leading crystal facet for samples of Fe:ZnSe annealed under 0 Rad/s (dashed black) and 44 Rad/s (dashed blue) measured by the laser scanning method.

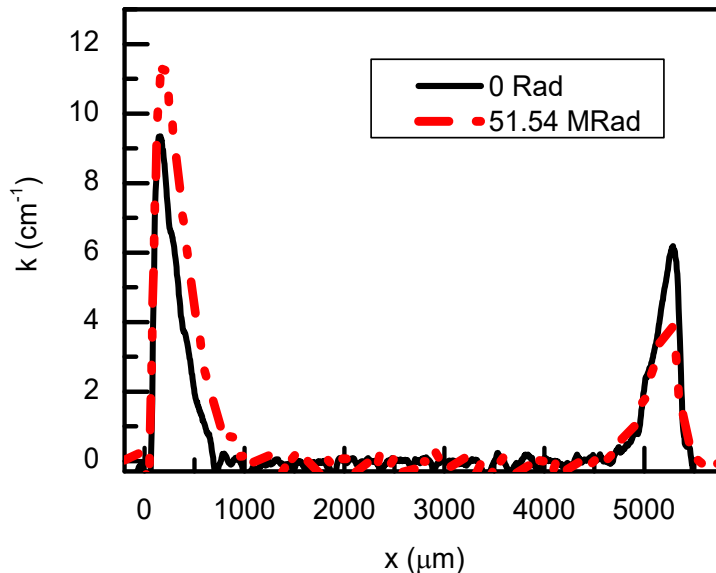


Figure 2.4.14. Absorption coefficient of Fe:ZnSe samples annealed under 44 Rad/s (dashed) and 0 Rad/s (solid).

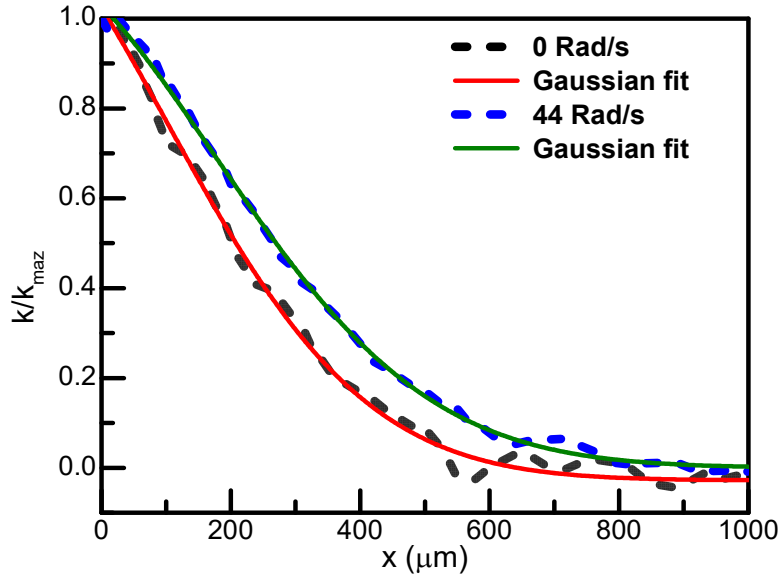


Figure 2.4.15. Normalized absorption coefficient vs. distance from the crystal edge for Fe:ZnSe annealed at 0 Rad/s (dashed black) and 44 Rad/s (dashed blue) and Gaussian fits (solid lines).

According to a simple model based on Fisk's diffusion Laws, if the diffuser is deposited initially onto the surface of a sample and spreads into one half-space, the concentration distribution $C(x,t)$ solution is in the form of a Gaussian [23,14,24] :

$$C(x,t) = \frac{M}{\sqrt{\pi Dt}} \exp\left(-\frac{x^2}{4Dt}\right)$$

where M denotes the number of diffusing ions deposited on the surface per unit area; D is diffusion coefficient, and t is annealing time. The concentration distributions (dashed lines) were fitted with Gaussians (solid lines) and agreed very well with theory. From these fits, diffusion lengths ($2\sqrt{Dt}$) and diffusion coefficients for these samples were calculated. In the ZnSe samples, the calculated diffusion length for the non-irradiated sample was 340 μm and in the irradiated sample diffusion length was 429 μm . The corresponding diffusion coefficients were $D = 2.4 \times 10^{-10} \text{ cm}^2/\text{s}$ and $D = 3.9 \times 10^{-10} \text{ cm}^2/\text{s}$, respectively, representing an increase in diffusion coefficient of 60%.

Doping ZnS with iron by post-growth thermal diffusion has shown very limited diffusion lengths as compared to ZnSe [23,18,19]. This is likely due to a combination of factors including a smaller crystal lattice parameter, and a stronger crystal field. This makes production of a large-scale Fe:ZnS crystals challenging. However, iron-doped ZnS is of interest for several reasons. In comparison with Fe:ZnSe it shows a larger damage threshold, and stronger crystal field splitting, which shifts the emission of iron in

ZnS to 3.3-4.5 μm spectral range. Therefore, significant radiation enhancement of diffusion of iron in ZnS is particularly useful.

Figure 2.4.16 shows normalized absorption coefficient as a function of distance from the leading crystal facet for samples of Fe:ZnS annealed under 0 Rad/s (dashed black) and 44 Rad/s (dashed blue) and Gaussian fits (solid lines).

Diffusion lengths calculated from the measurements of concentration gradients of non-irradiated and γ -irradiated samples of Fe:ZnS crystals were 203 μm and 296 μm respectively. These diffusion lengths corresponded to diffusion coefficients of $8.6 \times 10^{-11} \text{ cm}^2/\text{s}$ for Fe:ZnS annealed in the absence of γ -irradiation, and $1.1 \times 10^{-10} \text{ cm}^2/\text{s}$ for Fe:ZnS annealed under γ -irradiation. This corresponds to enhancement of diffusion coefficient of approximately 30%.

Radiation-enhanced thermal diffusion shows great promise as a means of achieving higher dopant concentrations and larger uniformly doped laser active crystals without introducing additional losses in the crystals. These results were achieved using only the relatively weak dose rate of 44 Rad/s and it is possible that a higher power dose rate, or alternative source of irradiation could provide greater enhancement to diffusion rates.

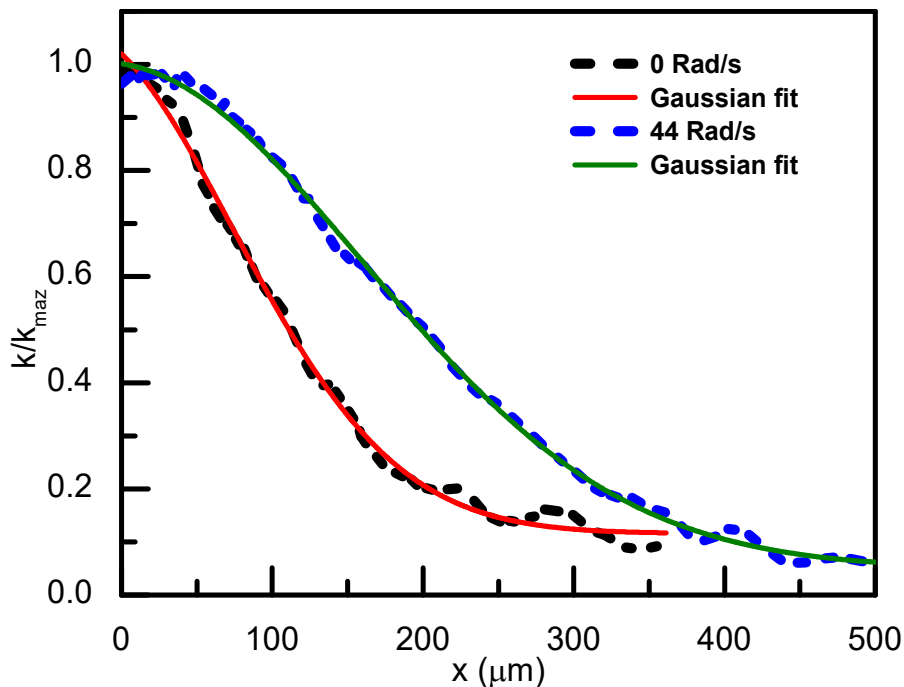


Figure 2.4.16. Normalized absorption coefficient vs. distance from the crystal edge for Fe:ZnS annealed at 0 Rad/s (dashed black) and 44Rad/s (dashed blue) and Gaussian fits (solid lines).

Conclusions

We developed a method of improving the diffusion rates of metal ions into II-VI semiconductor materials by means of radiation-enhanced post-growth thermal diffusion. Using a relatively low power dose, the diffusion coefficient of Fe^{2+} into ZnSe and ZnS were improved by 60% and 30% respectively. This offers a way of fabricating TM:II-VI laser elements with larger crystal sizes, higher dopant concentrations and more uniform distribution of dopant ions. This also opens the possibility of utilizing the post-growth thermal diffusion method for combinations of dopants and host crystals which were not previously available, such as large rare earth metals in II-VI. This technique has already shown positive results in this regard and were presented and published in [25, 26, 27, 28, 29, 30].

2.5 Enhancement of Cr in II-VI Crystals via Annealing in co-annealing in vapor of Zn

Based on computer simulations and theoretical considerations, it is predicted that the presence of interstitial cations may increase the diffusion rate in these crystals [31,32]. This takes place because the energy barrier is lower for an interstitial to kick-out a nodal cation into interstitial position, which, in turn, will cause another similar process and mediate the migration of the diffusing ion in the cation sublattice [31]. In our crystals this process should take place in the presence of interstitial Zn. Thus, the effects of excessive Zn, provided by co-annealing in Zn vapor, on diffusion characteristics of Cr in ZnSe were studied.

Chemical vapor deposition grown polycrystalline samples of ZnSe ($3.5 \times 8 \times 7 \text{ mm}^3$) were thoroughly cleaned with acetone, methanol, and DI-water, because surface contamination can create significant barriers for ion diffusion. A 150 nm thick Cr film was deposited on one of the largest facets of the crystal using magnetron sputtering. Samples were placed in quartz tube and a $\sim 0.8\text{g}$ piece of Zn metal was added such that there was no physical contact between the metal and the crystal. Another set of identical crystals was placed in the quartz tubes without the addition of Zn. The second set was used as a reference for comparing the thermal diffusion of Cr with and without co-annealing in vapor of Zn. Quartz tubes were pumped out (10^{-5} Torr) and sealed. Samples were then annealed at 1000°C for 3 days. After annealing samples were removed from quartz tubes. A 1.5mm thick layer was polished-off from the facets normal to the direction of diffusion in order to reduce the surface scattering associated with some surface degradation during the annealing process. The crystals were placed on a translation stage and were scanned across a focused beam of 1560 nm Er: fiber laser in the direction of diffusion. The diameter of the beam was $\sim 80\mu\text{m}$. Figure 2.5.1 depicts the experimental setup. Cr^{2+} has an absorption band of the ${}^5T_2 \rightarrow {}^5E$ transition with a peak at 1770 nm, the absorption spectra of such transition are shown in Figure 2.5.3. The radiation at 1560 nm coincides with this band allowing estimation of the Cr concentration by

measuring the power transmitted through the crystal with a thickness $l \sim 4$ mm.

Power transmitted through the crystal as a function of diffusion distance was recorded using a power meter connected to PC with analysis software and normalized with respect to the incident power. From the transmission measurements (T) an optical density, $OD = -\ln(T)$, was calculated. Figure 2.5.2 shows the plot of OD as a function of distance from the crystal facet (black curve). Due to linear relation between optical density and dopant concentration, the measured dependences were used to calculate the diffusion parameters. Based on Fick's laws of diffusion [33], for a diffuser that spreads into one half-space, the concentration distribution (C) as function of distance and time has a Gaussian form given by equation.

$$C(x, t) = \frac{M}{\sqrt{\pi Dt}} \exp\left(-\frac{x^2}{4Dt}\right)$$

where M represents the ions diffusing per unit area, D is diffusion coefficient, x and t are distance, and annealing time, respectively. The diffusion length, $L_{\text{diff}} = 2\sqrt{Dt}$, was estimated using parameters from fitting Gaussian curves to the OD plot. Obtained values for the diffusion length were 0.4mm and 0.87mm

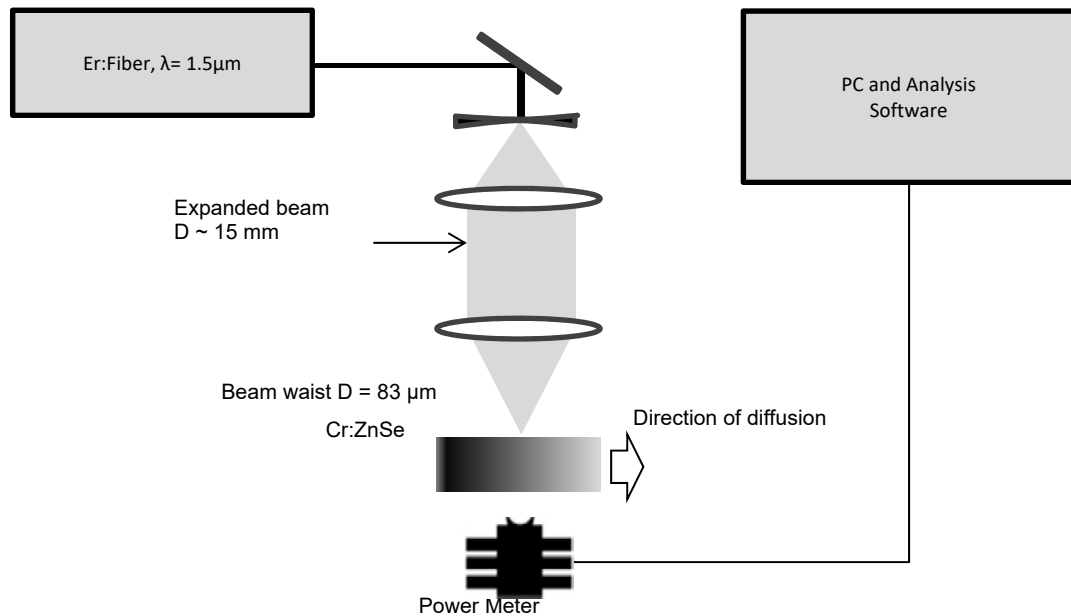


Figure 2.5.1. Experimental setup for measurement of spatial distribution of Cr^{2+} ions.

for the standard and Zn co-annealed diffusion methods, respectively. Hence, an improvement of more than 2.2 times and 4.7 times for diffusion length and coefficient of diffusion of Cr, respectively, was achieved through ZnSe co-annealing in vapor of Zn. Co-annealing in Zn vapor enables an excess of Zn interstitials in the ZnSe lattice [33]. The interstitial Zn^{2+} , which has vibrational energy, kicks out nodal Cr^{2+}/Zn^{2+} into an interstitial position and occupies the freed nodal position. Then, interstitial Cr^{2+} goes through another cycle of similar nodal-interstitial exchange and propagates further into the crystalline lattice, consequently mediating better diffusion of the desired ions. It is worth noting that, in some instances purification of the crystal from Cr takes place during annealing with Zn. It could result in reduction of chromium concentration in crystals after diffusion or even complete purification when the crystal is in physical contact with the Zn liquid during annealing. This happens since the solubility of a solute is usually higher in a liquid solvent than a solid.

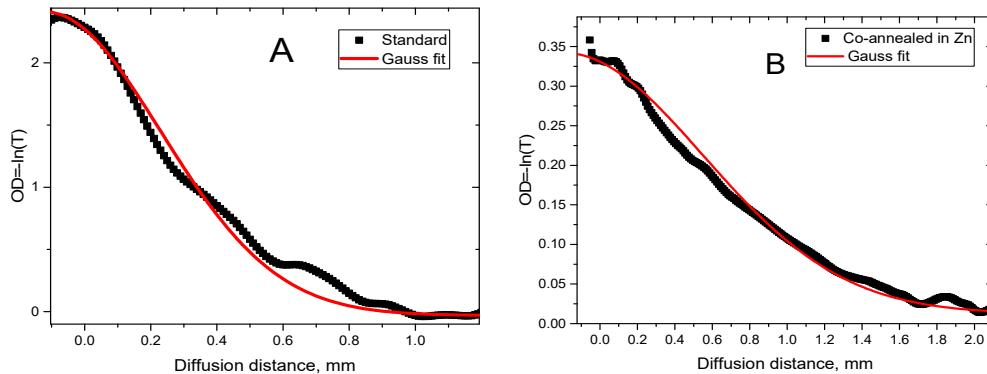


Figure 2.5.2. Optical density as a function of distance from the crystal facet. A) standard thermal diffusion method and B) thermal diffusion in presence of Zn vapor.

Similar purification results were seen by other groups in II-VI materials [34,35,36,37, 38]. We also found that this effect could be observed when ampoule has a poor vacuum, i.e. oxygen is present in the ampoule. At 1000⁰ C there is selenium atmosphere in the ampoule that can react with the deposited Cr film and form CrSe, followed by reaction (2.5.1) and (2.5.2) enabling Cr precipitation in non-volatile Cr₂O₃ form.

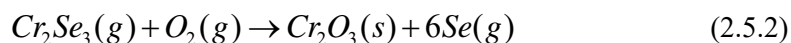
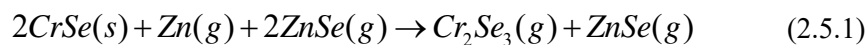


Figure 2.5.3 shows the absorption spectra of Cr:ZnSe before and after annealing in vapor of Zn and O_2 as well as in liquid Zn. It can be clearly seen that the characteristic Cr^{2+} absorption due to ${}^5T_2 \rightarrow {}^5E$ transition, with a peak at 1770nm is eliminated, after crystal annealing in Zn vapor in the presence of O_2 , as well as in Zn melt without oxygen. Inductively coupled plasma-mass spectroscopy (ICP-MS), which

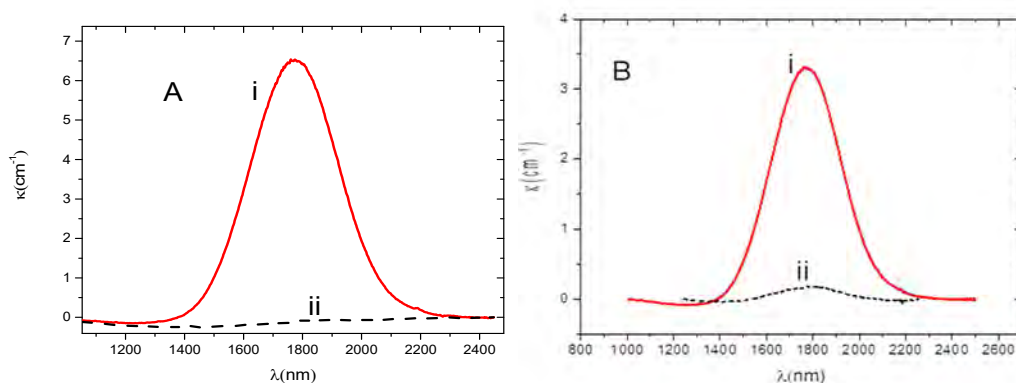


Figure 2.5.3. Absorption coefficient of Cr^{2+} in ZnSe A) before annealing (i), after annealing in vapor of Zn and O_2 (ii), B) before annealing (i), sample after annealing in Zn liquid (ii).

measures Cr at any valence state, was used to check for possible conversion of Cr^{2+} into any other valence state. After analysis it was seen that Cr concentration that was initially at 90 ppm dropped below the detection limit of 2ppm, confirming effective crystal purification from chromium.

Summarizing, the diffusion coefficient was improved by ~ 4.7 times as compared to “Standard” by co-annealing in Zn vapor during the thermal diffusion process.

2.6. Diffusion of transition metal ions in II-VI semiconductors. Theoretical and computational approaches

2.6.1. Introduction

II-VI semiconductors such as ZnSe doped with transition metal(TM) ions appear to be a good candidate for mid-infrared laser materials. In order to make these materials useful in practical applications, we must be able to dope the TM ions efficiently. A common method is thermal diffusion. However, diffusion of the TM ions in II-VI semiconductors is in general quite slow. In this report, we focus on the diffusion of Cr and Fe in ZnS and ZnSe crystals. In these crystals, Zn is positively and S/Se is negatively charged. Since the TM ions, Cr and Fe, are also positively charged, it is difficult for them to travel through the positively charged space. Some of the traditional migration paths are not available for this type of systems.

In order to enhance the diffusion speed, we first need to identify and understand a main migration mechanism. The goal of the present research project is to identify possible migration mechanisms and find ways to enhance the diffusion speed. We will take the following steps.

1. Identify possible migration mechanisms.
2. Develop a qualitative theory describing the migration mechanism.
3. Develop a kinetic Monte Carlo (KMC) simulation algorithm specific to zinc blend crystal structures.
4. Confirm the theory by the KMC simulation.
5. Estimate transition rates using first principles method.
6. Carry out quantitative Monte Carlo simulation.
7. Confirm the overall understanding by ab initio molecular dynamics (AIMD).

The first 4 steps and 50% of step 5 have been completed. We have started steps 6 and 7 based on the current stage of understanding. In the following we summarize the results for each steps.

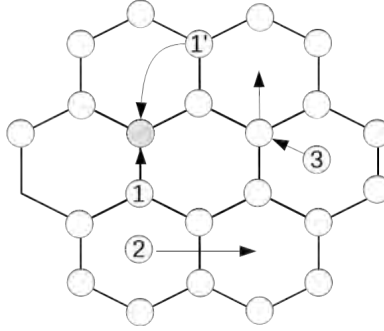


Figure 1: Schematic diagram for three different migration mechanisms, vacancy-assisted (1 and 1'), interstitial-to-interstitial (2), and knock-out (3).

2.6.2 Identifying possible migration mechanisms

Unfortunately, clean experimental data is still not available and thus the experimental data alone cannot determine the migration mechanism. Based on simple theoretical consideration, we have identified three migration mechanisms. A schematic diagram of three most probable diffusion mechanisms is shown in in Fig 1. The first one (①) is the vacancy assisted diffusion. An atom adjacent to the vacancy migrates to the empty site. Even the second neighbor atom ① can jump to the vacancy. This is a popular migration mechanism of self-diffusion in single element crystals such as Si. Upon the jump, the new vacancy is created at the original position of the atom that jumped. The second mechanism (②) shown in Fig 1 is the interstitial-to-interstitial migration. This is a popular mechanism for small dopants in non-ionic crystal. The third one (③) is a less known process where an ion in an interstitial site knocks out another ion in adjacent lattice site. In turn the knocked-out ion knocks out another ion at the nearest lattice site. The chain of collisions result in the diffusion. We shall call this mechanism *knock-out mechanism*. In the following we discuss the likelihood of these migration mechanism.

2.6.2.1 Interstitial-to-interstitial migration

There are two major interstitial sites in the zinc blend crystals. One is at a center of the tetrahedron formed by Zn ions (T_{Zn}) and the other by S/Se ions (T_{Se}). Due to the charge distribution, positively charged TM ions are more stable at the negatively charged T_{Zn} than the positively charged T_{Zn} . Therefore, the interstitial TM ions stay at T_{Se} . The direct transition from T_{Se} to another T_{Se} is unlikely due to the long distance and high potential energy barrier between them. Going from T_{Se} to the adjacent T_{Zn} site is possible but it must overcome a steep uphill potential. Therefore, this mechanism is not considered as a main mechanism. We carried out ab initio molecular dynamics simulation and confirmed that this process can happen but less likely than other mechanisms. (See Section 6.)

2.6.2.2 Vacancy-assisted migration

Conceptual diagrams shown in Fig 2 indicates that the S/Se vacancy does not assists the TM ion migration due to the Coulomb repulsion from other cations adjacent to the vacancy. This is a major difference from self-diffusion of Si. On the other hand, a Zn vacancy will allow relatively

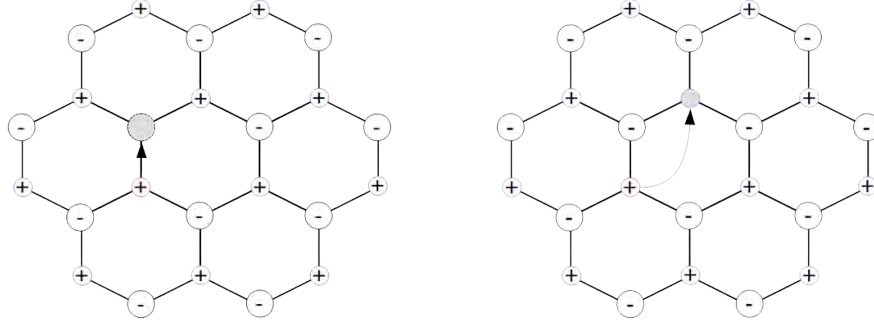


Figure 2: Vacancy-assisted migration of TM ions at the lattice site.

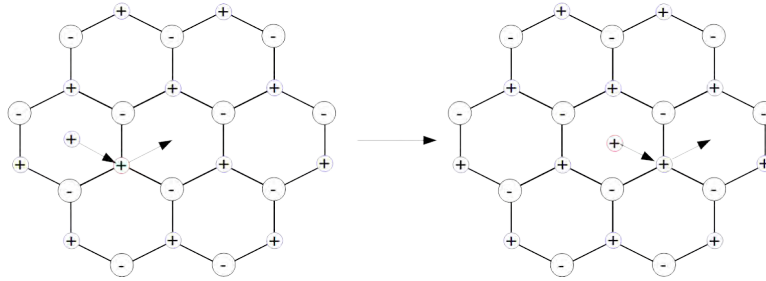


Figure 3: Knock-out migration.

easy migration over the second nearest neighbor distance. We shall call it vacancy-assisted (VA) migration. At the present, we have no data for the migration energy. However, similar cases has been studied for Zn self-diffusion in ZnO crystal. If the Fermi level is closer to the bottom of the conduction band, this mechanism is expected to be dominant. This suggests that the increasing the concentration of Zn vacancy could lead to faster diffusion. (See Section 3 for theoretical analysis). However, too many of Zn vacancies may cause undesired change in the electronic structure. Significant electric conductivity has been observed under the presence of Zn vacancies but disappears when Zn vapor pressure is elevated, suggesting that the Zn vacancies can be eliminated by the additional Zn vapor pressure.

2.6.2.3 Knock-out migration

Figure 3 illustrates the knock-out (KO) migration mechanism. Initially a TM ion is substituted to a Zn site. A Zn ion arrives to a nearest interstitial site to the TM ion. Since Zn ion and the TM ion are similar from the view of anions (See Section 5.2 for the first principle calculation), it is relatively easy to replace the TM ions with the Zn ion. The TM ion is now knocked out to an interstitial site. In turn, the TM ion knocks out a nearby Zn ion to an interstitial site and occupies the Zn site. As Fig 3 shows, the TM ion migrated to a different lattice site. By repeating this process, the TM ion can diffuse relatively quickly. Since this migration is assisted by Zn in the interstitial site, we expect that raising the Zn vapor pressure increases the diffusion speed. Furthermore, since Zn and Cr behave similarly, higher concentration of interstitial Zn ions entropically destabilize Cr ions in the lattice site, leading to higher diffusion rate. Based on this simple consideration, we have suggested our experimental partner to raise Zn vapor pressure. It turns out that applying ambient

Zn vapor pressure (1 atm) increases the diffusion constant significantly (500% increase. See the report by the experimental PI.) This experimental results indicate indirectly that the knock-out mechanism is a dominant process.

2.6.3 A qualitative theory

Diffusion constants for simple crystals are well studied. For example the diffusion constant for the interstitial-to interstitial migration in simple cubic crystal or vacancy migration in Si crystal is given by

$$D = \frac{1}{6}\eta a^2 \kappa \quad (1)$$

where a and κ are lattice constant and transition rate for a single jump. The prefactor η is a dimensionless constant solely determined by the crystal structure, for example, $\eta = 1$ for simple cubic and $\eta = 3/4$ for diamond structure.

We have developed a similar formula for the vacancy-assisted or knock-out migration. They seems very different from mechanical view of point. However, mathematically they share many similar features. The migration takes place only when a vacancy or an interstitial ion hits the TM atom, which immediately suggests that the migration speed depends on the density of vacancies and interstitials and also on their movement. Based on a simple theoretical consideration, *we found the following general expression of diffusion constant for these two mechanisms:*

$$D = \frac{1}{6}\eta a^2 \kappa \rho \quad (2)$$

where the concentration of vacancies or interstitial ions are measured in atomic fraction. For diffusion without assisting particles, $\rho = 1$ which leads to Eq. (1). The prefactor η is again a dimensionless constant determined solely by the crystal symmetry and the migration mechanism (VA or KO). While the formula looks oversimplified, it turns out to be very useful. Once η is obtained by some means, this formula gives the diffusion constant for different materials, different concentration of impurities and different environment such as temperature without further simulation for different cases.

Since the TM ions cannot move until an assisting particle arrive, this diffusion processes is limited by the mobility of the assisting particle. In principle, η can be determined from the waiting (residence) time distribution. We introduce an effective transition rate $\tilde{\kappa}$ such that

$$D = \frac{1}{12}a^2 \tilde{\kappa} \quad (3)$$

which leads to $\tilde{\kappa} = 2\eta\kappa\rho$. The additional factor 1/2 is due to the Zn-Zn distance is $a/\sqrt{2}$. On the other hand, the effective transition is equivalent to the inverse of the mean waiting time $\langle\tau_w\rangle$. Hence, we obtain a useful expression:

$$\eta = (2\kappa \langle\tau_w\rangle \rho)^{-1}. \quad (4)$$

It is clear that the diffusion speed can be enhanced if we can manipulate the waiting time. Unfortunately, we have not been able to find an analytic expression of the mean waiting time so far. Thus we try to get it by numerical simulation. (See Section 4.2). However, we think that an analytical expression is still possible and continue to explore possibilities.

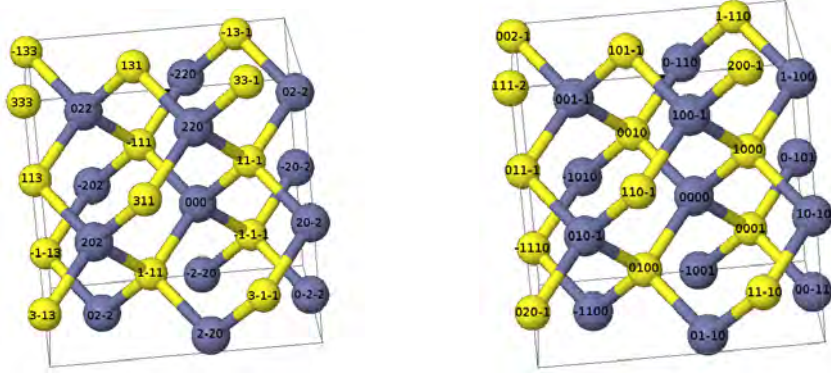


Figure 4: Three dimensional indexing (left) and four-dimensional indexing (right) of zinc blend crystal

2.6.4 Kinetic Monte Carlo Simulation

We have developed a new kinetic Monte Carlo simulation specifically designed to investigate the diffusion processes in diamond and zinc blend structures. The simulation is based on a standard discrete random walk model with a constant transition rate k . A problem is that the mathematical expression of the lattice coordinates for the zinc blend crystal is known to be rather complicated. For example, what is the coordinates of the nearest neighbor to a lattice point (n, k, ℓ) ? The left panel of Fig 4 shows that the indexes of nearby sites seems unrelated to the site index. Furthermore, it is difficult calculate the distance between two sites from their indexing. *We have developed a new coordinate system which is mathematically simple and quick.* It simplifies the coding of KMC simulation significantly. We first explain briefly the new algorithm and results of the simulation follows.

2.6.4.1. Four dimensional indexing

We assign a set of four integer $\langle x_1, x_2, x_3, x_4 \rangle$ to every lattice point. If $\sum x_i \in \{0, 1\}$, the indexes represent a lattice point in zinc blende crystal. If $\sum x_i = 0$, then it is Zn site and if $\sum x_i = 1$, the point is S/Se site. There are many advantage to use this indexing system. Suppose that we want to know the location of the nearest neighbor to Zn at $\langle 1, 0, -1, 0 \rangle$. Just add 1 to one of the indexes. The nearest sulfur atoms are found at $\langle 2, 0, -1, 0 \rangle$, $\langle 1, 1, -1, 0 \rangle$, $\langle 1, 0, 0, 0 \rangle$, and $\langle 1, 0, -1, 1 \rangle$. Subtracting 1 from the sulfur indexes give the location of the nearest Zn atoms. Furthermore, the two tetrahedral interstitial sites are indexed in the same way but $\sum x_i = 2$ and 3.

Using the four-dimensional indexes, it is trivial to compute the minimum number of hops from one lattice site $\langle x_1, x_2, x_3, x_4 \rangle$ to another lattice site $\langle y_1, y_2, y_3, y_4 \rangle$. It is simply

$$d = \sum |x_i - y_i|. \quad (5)$$

Taking advantages of the four dimension indexing, we have written a new kinetic Monte Carlo simulation code which simulate random walks on the four dimensional simple cubic lattice under the above constraints. The algorithm is very simple and computation is quick in the four dimensional simulation. We can switch the four-dimensional coordinates to the original three-dimensional

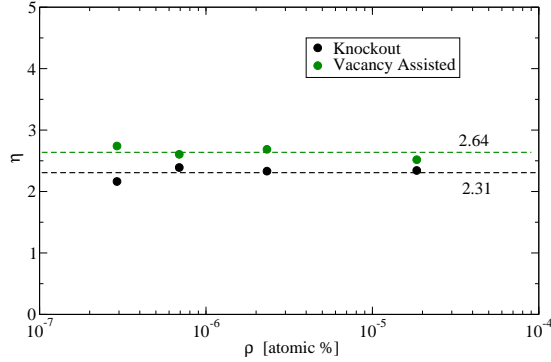


Figure 5: The value of η obtained from KMC simulation at four different concentrations of assisting particles.

coordinates by a simple linear transformation

$$\begin{pmatrix} X \\ Y \\ Z \\ N \end{pmatrix} = \begin{pmatrix} 1 & 1 & -1 & -1 \\ 1 & -1 & 1 & -1 \\ -1 & 1 & 1 & -1 \\ 1 & 1 & 1 & 1 \end{pmatrix} \begin{pmatrix} x_1 \\ x_2 \\ x_3 \\ x_4 \end{pmatrix} \quad (6)$$

where X , Y , and Z are the regular three-dimensional coordinates of lattice or interstitial site with lattice constant $a = 4$. For other lattice constant, X , Y , and Z should be scaled by an appropriate factor. $N \in \{0, 1, 2, 3\}$ is the integer index specifying type of the lattice/interstitial site.

2.6.4.2. Determination of η

We have carried out KMC simulation and obtained diffusion constant at four different concentrations of assisting particles. Since η does not depend on a nor κ , we set length scale $a = 1$ and time scale $\kappa = 1$. Figure 5 plots η for both vacancy assisted and knock-out migration. The data is still noisy due to insufficient sampling. Within the statistical error, η appears to be constant and order of 1 as predicted in the previous section.

We have also obtained the waiting time probability distribution from the same simulation. The results are plotted in Fig. 6. The data is not noisy even when the probability as small as 10^{-3} . However, the mean waiting time is about $10^5 - 10^6$ where the probability is extremely small and noisy. In other words, the diffusion constant is determined by very rare events, which explains why the diffusion in these system is so slow. We are currently running the simulation on the massively parallel computers to obtain more samples.

Although the statistics is still insufficient, we attempt to verify the relation (4). In Table 2, the mean waiting time for the both VA and KO mechanisms at various different concentration of assisting particles. Using these data, η is estimated using Eq. (4). η appears almost constant for all cases. However, their absolute value is slightly different from the direct observation shown in Fig. 5. This is due to insufficient sampling and we are trying to improve it.

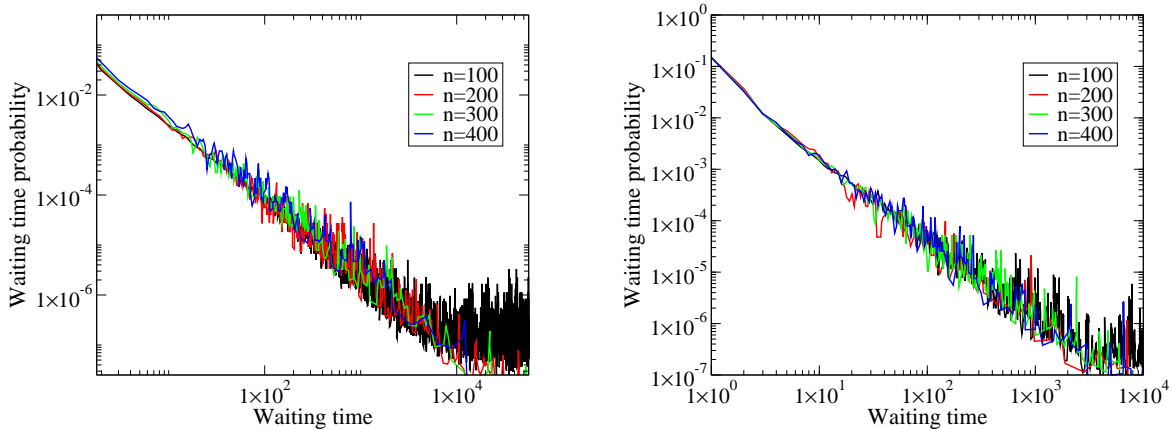


Figure 6: Waiting time probability distribution for vacancy-assisted migration (left) and knock-out migration (right).

Table 1: Mean Waiting Time

Concentration [at%]	Vacancy-Assisted		Knock Out	
	τ_w	η^*	τ_w	η^*
1.85×10^{-5}	9.19×10^5	2.94	9.00×10^5	3.00
2.33×10^{-6}	6.95×10^6	3.09	7.08×10^6	3.03
6.91×10^{-7}	2.12×10^7	3.41	2.32×10^7	3.12
2.92×10^{-7}	4.02×10^7	4.26	5.12×10^7	3.34

Table 2: Mean waiting time (τ_w) for VA and KO migration. Using these data, we estimated η^* in Eq. (4), which should be compared with the directly observed value shown in Fig. 5.

2.6.5 Electronic and Geometric Structures

The above discussion is based on the scale independent argument and thus it is not possible to get absolute diffusion constant with real world units. While the distance scale (lattice constant) is well known, the time scale (transition rate κ) is not known. For quantitative investigation, it is necessary to find the realistic value of κ either from experimental measurements or first principles calculation. Since we could not find useful data in literature, we must resort to first principles calculation. In general, transition rate is determined by migration energy (activation energy) E_a as

$$\kappa = \nu e^{-\beta E_a} \quad (7)$$

where $\beta = 1/k_B T$ is inverse temperature and ν attempt frequency. The migration barrier height can be calculated by density functional theory.

Another unknown value is the concentration of Zn vacancies and Zn interstitials. They are determined by the formation energy which can be also obtained from the density functional calculation. We are still calculating the barrier energies. Here we show the equilibrium energy, band structure and equilibrium geometry. The electronic and geometric structure of the crystals and

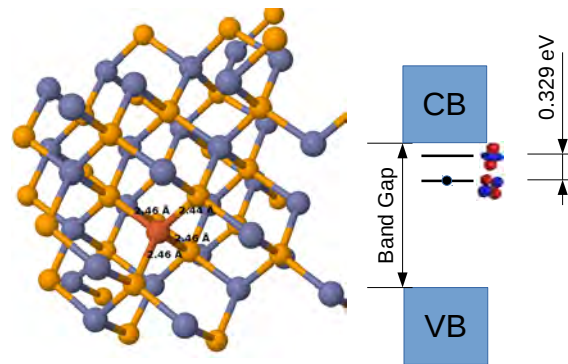


Figure 7: Left: Optimized geometry of substitutional Fe ion in ZnSe crystal. Distortion around the impurity is very small. Two localized states was found in the band gap. One is occupied and the other is not. The proposed mid-infra red laser utilized these two states.

impurities are computed with NWChem package, a part of which was based on the simulation codes developed by the present investigator (R. K.).

To calculate impurity states, we used supercell consisting of 216 atoms and about 2000 electrons. Each electron is represented by 160x160x160 grid. This size of calculation was too big for our in-house small cluster computers. The University of Alabama at Birmingham recently acquired a 2000 core cluster which becomes available for this project. Now, we will be able to compute the large systems.

2.6.5.1 Substitutional TM ion

We have calculated optimized geometry and electronic states for ZnS:Cr and ZnSe:Fe. Figure 7 shows the optimized geometry around the substitutional Fe ion. The distortion is found to be very small and thus local electronic state is unmodified significantly. Two localized state appear in the band gap, one is occupied and the other empty. The energy difference is 0.329eV which is within the mid-infrared region. We have a similar results for ZnS:Cr. However, our objective of the first principles calculation is to investigate the migration mechanism. We want to find how to destabilize the dopant ion so that it can move out of the stable position. we are currently calculating formation energy of TM- V_{Zn} Frenkel pair by forcing the TM atom to leave the lattice site. Since the Frenkel pair can initiate the chain of knock-out migration. The formation energy will tell us the likelihood.

2.6.5.2 Interstitial TM ion

Similarly, we calculated the optimized geometry and electronic states of TM ions in interstitial site. Again, we investigated ZnS:Cr and ZnSe:Fe. We confirmed that the charge state of the most stable configuration is 2+. Hence, we assume that the TM ions migrate as TM^{2+} .

One of the important quantity to understand KO migration is the energy cost of swapping interstitial Cr and Zn. We have calculated the energy of ZnS with interstitial Cr and ZnS with substitutional Cr and interstitial Zn. The latter is substantially more stable than the former. The energy difference is as much as 5.33 eV, indicating that the first step of KO migration (see Fig 3)

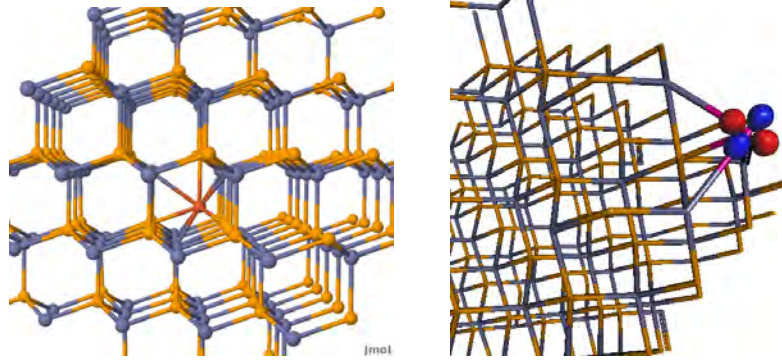


Figure 8: Left: Optimized geometry of interstitial Fe ion in ZnSe crystal. Distortion around the impurity is very small. Right: The charge state of Fe is found to be 2+ and the highest occupied state is localized in the band gap.

is slow but the second stage is very fast. Therefore, we need a high density of interstitial Zn to knock out Cr from the lattice site.

2.6.6 Ab initio Molecular Dynamics

Ab initio molecular dynamics simulation calculate the trajectory of atoms from the first principle. The trajectories are determined by classical Newton's equation of motion. However, the force between atoms are determined by computing electron density using density functional theory. Since the force is determined by the first principles, the molecular dynamics simulation is essentially parameter free. Hence, the method accurately predicts the motion of atoms. However, the simulation is computationally very expensive and a large number of CPU time is required. This kind of method is useful for short period of an event.

We set up initial conditions that is likely to lead to interstitial-to-interstitial migration. After several tries and errors, we are able to realize the migration.

In series of snapshots are shown in Fig. 9, Cr ions (blue) in ZnS crystal migrates from a T_S (yellow tetrahedron) to T_{Zn} (silver tetrahedron) and continues to the second T_S site. The first transition (2nd frame) state indicates huge deformation to reduce Coulomb repulsion. The second transition (4th frame) was quick since it is downhill process. Based on the unrealistic distortion during the first stage of the migration, this process is unlikely to happen under normal circumstance. It could happen under extreme conditions such as a large dose of radiation.

2.6.7 Conclusions

We have identified two most plausible migration mechanisms for TM ions in zinc blend crystals. Both require assistance from other particles such as vacancies and interstitial Zn ions. We have developed phenomenological theory for the diffusion constants which relates the diffusion speed to mean waiting time, which is in turn determined by the diffusion of assisting particles.

We have developed very efficient algorithm for kinetic Monte Carlo simulation based on random walk in a four dimensional space. The simulation confirmed the validity of the theory we developed.

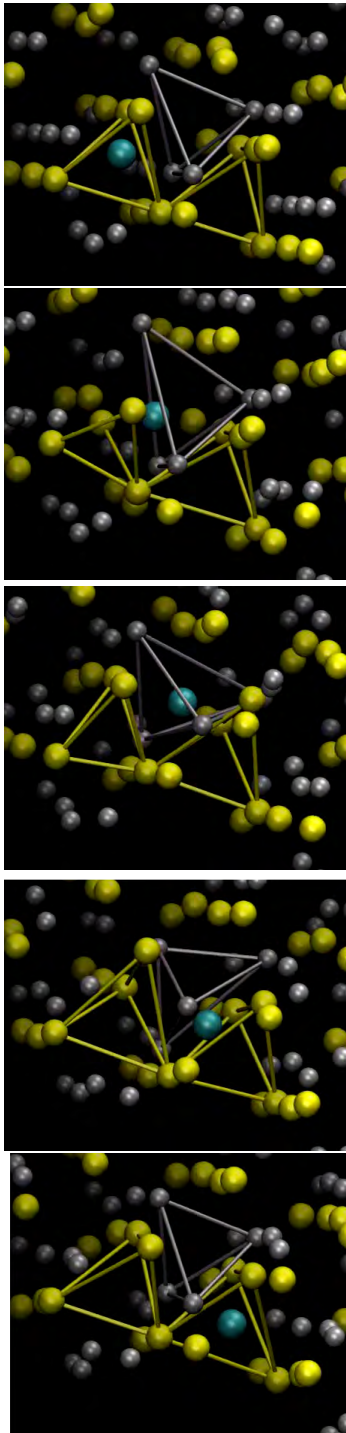


Figure 9: Ab initio molecular dynamics simulation of interstitial-to-interstitial migration.

2.7. TM Diffusion under Hot Isostatic Pressing

Another method for enhancement of diffusion is related to the diffusion temperature increase [39]. The use of elevated temperatures is accompanied by a strong sublimation of ZnS and ZnSe and reduction of the crystal's optical quality. The issue may be mitigated by simultaneous application of high temperature and high pressure. Thus, Hot Isostatic Pressing was used as the means for simultaneous application of high temperature (up to 13000 C) and high pressure (up to 3000 atm) to study diffusion processes of Fe in ZnSe and ZnS.

It is well-known that the diffusion rate increases with the increase of temperature. However, utilization of high temperatures is problematic for ZnSe/ZnS, because of the strong sublimation that these crystals have at elevated temperatures. Additionally, ZnS crystals transform from zinc blende (ZB) phase into wurtzite (W) phase at temperature of 1020 °C, which is accompanied by degradation of the optical quality[40]. The problem of sublimation can be addressed by simultaneous application of high pressure during the thermal diffusion process. Hot Isostatic Pressing (HIP) can provide both high temperatures and high pressures, thus HIP was utilized for enhancement of the diffusion rate of Fe in ZnSe/ZnS. CVD grown bulk polycrystals with dimensions 5x5x2mm³ were thoroughly cleaned with acetone, methanol, and DI-water. A 150 nm Fe film was deposited on one of the 5x5mm² facets. The ZnSe and ZnS samples were placed in HIP and treated at 1300°C at two different pressures of 1000 and 3000 atm. Measurement of Fe concentration was carried out in the HIP treated samples using the same platform described in Figure 2.5.1, but instead of the Er:Fiber laser a tunable Cr:ZnS laser operating at 2000 and 2600nm with a tightly focused beam of 56µm was used. Optical density as a function of diffusion distance was plotted. As can be seen from the Figure 2.7.1 the diffusion length does not depend on the pressure of the HIP chamber and is the same for both pressures. Diffusion coefficient corresponding to the diffusion length of 0.4 mm is $1.1 \times 10^{-9} \text{ cm}^2/\text{s}$, this is a ~14 times improvement over the diffusion coefficient of $8 \times 10^{-11} \text{ cm}^2/\text{s}$ measured at 950°C. The diffusion length of Fe in ZnSe treated at 1300°C and 3000 atm is 0.84 mm, as can be seen in Figure 2.7.2A, this translates to a diffusion coefficient of $4.9 \times 10^{-9} \text{ cm}^2/\text{s}$. This is an improvement of ~13 times as compared to diffusion coefficient at 950°C.

A second method was used to measure the Fe concentration using characteristic absorption of Fe^{2+} due to ${}^5E \rightarrow {}^5T_2$ transition. Absorption spectra of the samples shown in Figure 2.7.2 B were measured with Shimadzu FTIR spectrophotometer at room temperature by consequently polishing-off $\sim 40\text{-}100\mu\text{m}$ from the surface from which diffusion occurred. Graph of optical density vs polished-off thickness was obtained by normalizing to the value of the maximum optical density.

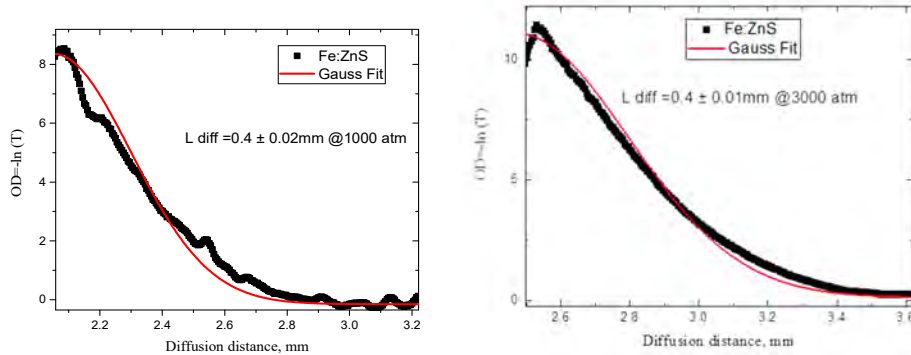


Figure 2.7.1 Optical density as a function of distance from the crystal facet in ZnS annealed at 1300°C , 1000 atm (left) and 3000 atm (right).

Using the solution of concentration distribution given in equation (2.5.1) the dependence of the optical density on the polished-off thickness (d) can be defined as,

$$OD(z) = \int_z^\infty \sigma C(x,t) dx = \sigma M \left[1 - \text{erf} \left(\frac{z}{4Dt} \right) \right] \quad (2.7.1)$$

where σ is the absorption cross-section and the error function is given by equation (4).

$$\text{erf}(x) = \frac{2}{\sqrt{\pi}} \int_0^x \exp(-\xi^2) d\xi \quad (2.6.2)$$

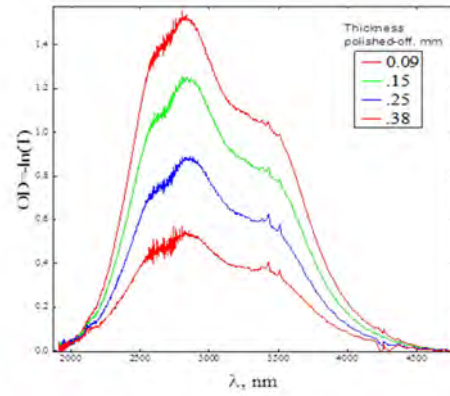
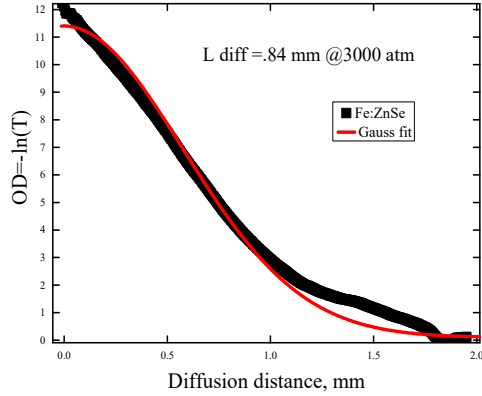


Figure 2.7.2 Optical Density as a function of distance from the crystal facet in ZnSe annealed at 1300°C, and 3000 atm (A, left). Absorption spectrum of Fe:ZnSe crystal measured in the direction of diffusion after polishing-off (B, right).

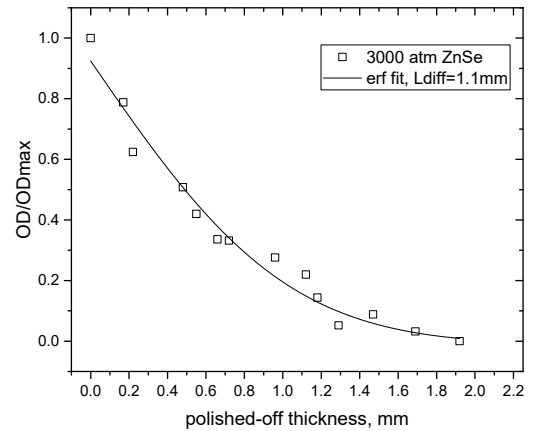
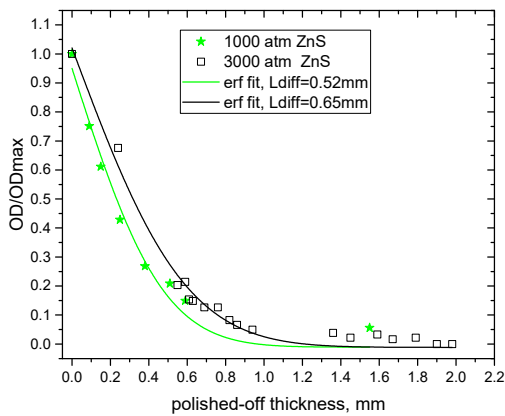


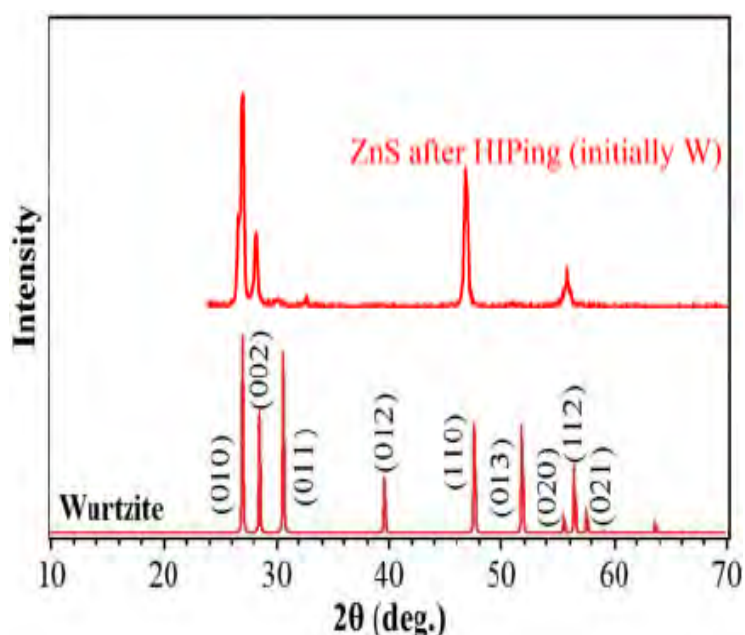
Figure 2.7.3 Normalized optical density as a function of polished-off thickness ZnS (A, left) and ZnSe (B, right).

Fitting according to the equation (3) was done, as shown by solid lines in Figure 2.7.3. From the parameters of the fit the diffusion length of Fe in ZnS was calculated to be 0.52mm and 0.65mm for 1300°C HIP treatments at 1000 atm and 3000atm, respectively. For Fe diffusion in ZnSe at 1300°C and 3000 atm the diffusion length was calculated to be 1.1mm. These results are in agreement with the more precise laser scanning method. The diffusion coefficient of Fe in ZnS is of the same order of magnitude. This is an unexpected behavior since diffusion of the TM ions in ZnS is usually slower than in ZnSe due to a smaller lattice constant in ZnS. It was seen that the grain size grows from ~40µm to ~250µm after HIP treatment of ZnS, similar grain size was reported by other groups as well [41]. On the other hand the

grain size grows much faster in ZnSe. The smaller grains size in ZnS creates a much higher grain boundary concentration than in ZnSe. Since diffusion predominantly occurs through the grain boundaries diffusion in ZnS is enhanced to a higher degree.

X-Ray Diffractometry (XRD) was used to verify the crystallographic phase of the HIP treated ZnS crystals with initial ZB and W structures. The XRD inspection was performed using a 2θ -scan x-ray diffraction (Philips X-Pert MPD, The Netherlands) with a Cu K-alpha anode. Spectra were measured in the 10° to 74° range of 2θ with a step size of 0.05 degrees and accumulation time of 2s. It was found that during preparation of the ZnS powder for XRD measurements the initial W phase of the polycrystalline samples were transformed to ZB by mechanical grinding at room temperature. Therefore, in our analysis only bulk polycrystalline samples without mechanical grinding were used. Thus, the ratio of the diffraction peak amplitudes could be different in comparison with standard powder pattern.

In our experiments both W and ZB polycrystalline samples were used. The XRD patterns in Figure 2.7.4 show that the used HIP conditions ($P=1000$ atm, $T=1300^\circ$ C) prevent phase transformation from W to ZB. More importantly it was seen that HIP treatment preserves the ZB crystallographic structure, which is crucial for practical applications.



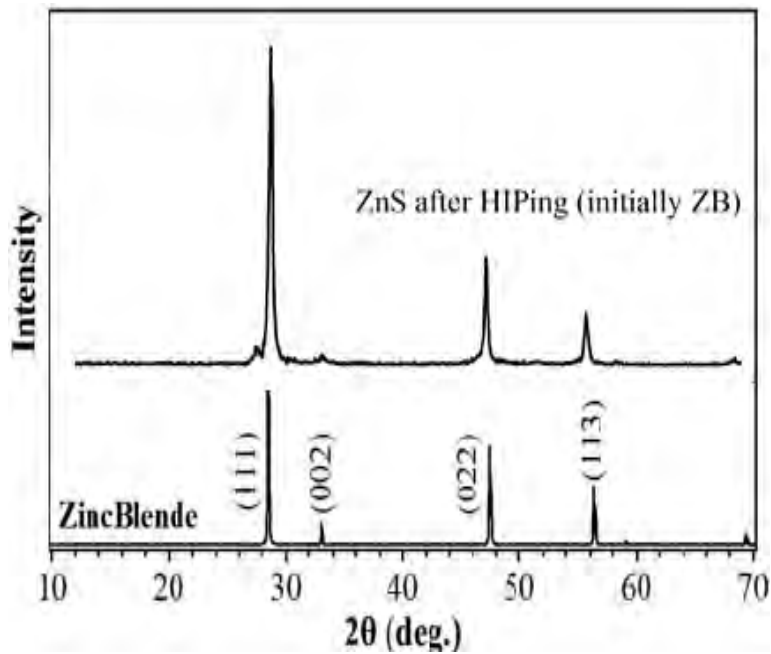


Figure 2.7.4 XRD pattern of HIP treated of predominantly W (top A) and ZB (top B) ZnS. The standard patterns of W and ZB are from JCPDS card 79-2204 and 77-2100, respectively A and B bottom.

Single Crystal Growth and Effective Doping of Fe:ZnS under Hot Isostatic Pressing

Polycrystalline bulk samples of ZnS ($7 \times 7 \times 8 \text{ mm}^3$) grown by chemical vapor deposition with the average grain sizes of $\sim 30 \mu\text{m}$ were used in our experiments. A 480 nm thick film of Fe was deposited on one of the $7 \times 7 \text{ mm}^2$ facets of the crystal. The crystals were wrapped in $25 \mu\text{m}$ thick Ta foil. Wrapping was done in order to reduce any possible contamination. The wrapped samples were placed in Hot Isostatic Pressing (HIP) chamber for treatment at temperature of 1350°C and 2000 atm pressure for 72 hours. The purpose of HIP treatment was to study the grain growth of polycrystalline ZnS and diffusion rate of Fe in the same crystal at elevated temperatures. Application of high pressures is necessary to suppress possible sublimation of the crystal at high temperatures as well as to suppresses conversion of the zinc blende (ZB) structure into wurtzite [7]. Since wurtzite structured ZnS has inferior optical quality to its ZB polymorph, preservation of the latter in our crystals is essential for preservation of the high optical quality of starting material.

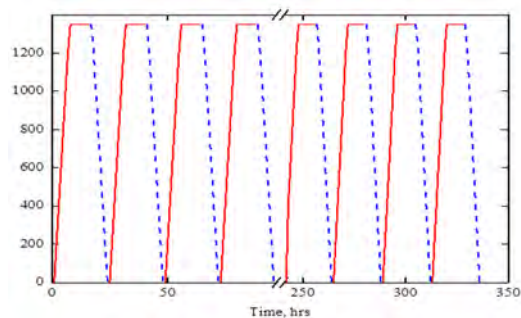


Figure 2.7.5. HIP consists of 8 cycles of treatment with 9h duration each.

After the HIP treatment was completed, the samples were removed from the chamber and the facets parallel to the direction of the diffusion were polished. After a rough polishing the grains were visible to the naked eye. The average grain size was estimated to be ~ 5 - 10 mm in diameter. The individual grains in HIP treated samples can be seen in Figure 2.7.6. X-Ray Diffractometry (XRD) was utilized to study the crystallographic structure of the HIP treated crystals with initial ZB structure. The XRD diffraction patterns were measured using a 2θ -scan angle X-ray diffractometer (Philips X-Pert MPD, The Netherlands) with a Cu K-alpha anode. Spectra were measured in the range of 25° - 65° with a step size of 0.05° and accumulation period of 2 seconds. The XRD patterns of the crystal before (red curve) and after (green curve) HIP treatment is shown in the Figure 2.7.7. From the Figure 2.7.7, all the peaks except for the (111) peak at 28.557° disappeared. This means that the initially polycrystalline ZB ZnS was converted to monocrystalline ZB under the HIP treatment. The (222) at 59.133° should be also seen, however, since the magnitude of this peak is 50 times smaller than the (111) peak it was not resolved. The grain growth in undoped ZnS was seen to be exponentially proportional to the temperature in [8] at temperatures up to $\sim 1100^\circ\text{C}$. Extrapolating this data yields $\sim 700\text{mm}$ grain size at 1350°C . We do not see the grain growth to this extent. This could be due to a slowing of the grain growth in doped ZnS that we noticed for Fe and Cr dopants.

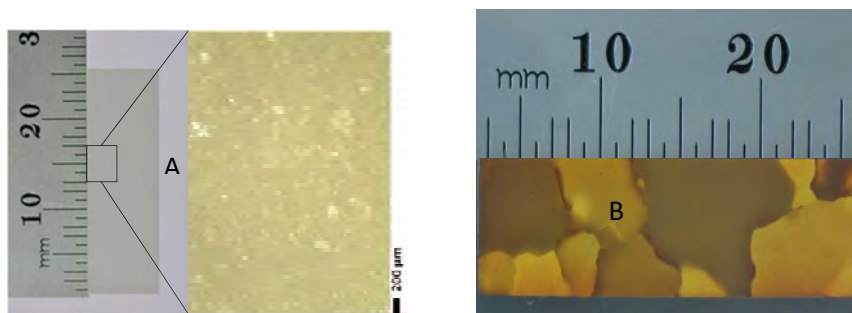


Figure 2.7.6. Picture of ZnS sample before HIP treatment (A) and Fe:ZnS sample after HIP treatment;

The diffusion of Fe in ZnS accompanied by ZnS recrystallization was also studied under HIP treatment at 1350°C . Two different methods were used to estimate the diffusion length of Fe in ZnS. In the first method, the power of a tunable Cr:ZnS laser, tuned to 2400nm and 1990nm , transmitted through the crystal as a function of diffusion distance was recorded. The transmission was calculated by normalizing to the incident power. The

transmission at 1990nm was used as the baseline and transmission of the 2400nm beam was used to map the Fe concentration as a function of the position from the crystal facet, since it falls in the absorption band of Fe^{2+} , due to ${}^5E \rightarrow {}^5T_2$ transition. From the transmission measurements (T) an optical density, $OD = -\ln(T)$, was calculated and plotted against the position, shown in Figure 2.7.8-a (solid line).

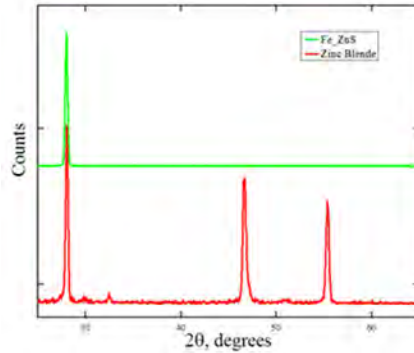


Figure 2.7.7 XRD patterns of Fe:ZnS in diffusion doped ZB polycrystal (bottom) and Fe:ZnS single crystal grown in the HIP process (top).

In the second method, the transmission spectra of the samples were measured with Shimadzu FTIR spectrophotometer at room temperature through a 1mm diaphragm where the crystal was shifted 0.5 mm in the direction of diffusion for each measurement. Figure 2.7.8-b shows transmission spectrum of Fe:ZnS near the edge of the facet through which the diffusion was performed. The transmission data at 2400nm matching the wavelength of the laser in the previous method was used to plot OD as shown in Figure 2.7.8-a (square dots). As can be seen from the Figure 2.7.8-a, there is a good agreement between the two methods. One can see that the diffusion does not follow the simple Fick's 2nd Law of diffusion and does not have a pure Gaussian shape. This phenomenon might be explained by a superposition of Fick's diffusion and diffusion through the grain boundaries experiencing fast exponential growth. Hence, for the first time Fe:ZnS crystals of 8 mm length with $\sim 3 \times 10^{18} \text{ cm}^{-3}$ were demonstrated via post-growth thermal diffusion process.

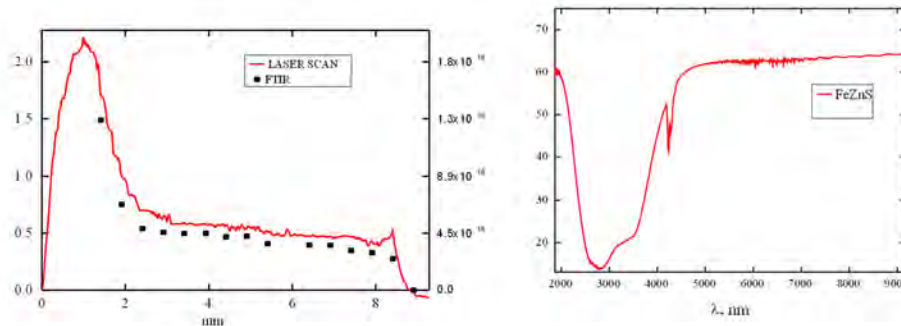


Figure 2.5.8. a) Optical density as a function of position in ZnS crystal measured by FTIR spectrometer (dots) and by laser radiation at 2.4 μm ; b) Transmission spectra of inspection polished Fe:ZnS

3. Diffusing doped RE:II-VI materials

3.6. Spectroscopic characterization of Pr³⁺:ZnSe crystals fabricated via post growth thermal diffusion

Rare Earth (RE) metal doped II-VI semiconductors are also suitable candidates for new promising mid-IR gain media. Pr³⁺ ions have several transitions covering spectral range from visible to mid-IR. The mid-IR lasing of Pr³⁺ ions has been demonstrated at 2.5, 5.2, and 7.2 μm oscillation wavelengths [42, 43, 44]. In our paper we report fabrication Pr:ZnSe crystals using post growth diffusion method and spectroscopic characterization of these materials under visible and near IR optical excitation

Sample Preparation

Post growth diffusion is simple and cost effective in comparison with crystal growth. This technology allows fabrication of large scale uniformly TM doped II-VI semiconductors. Praseodymium has relatively low melting point at 935°C enabling diffusion from the liquid phase in quartz ampoules. The samples of ZnSe were cut to 6x6x5 mm and polished and cleaned with acetone and methanol in sequence. These samples were then sealed in quartz ampoules evacuated to 10⁻³ Torr along with 0.3g of Praseodymium chunks.

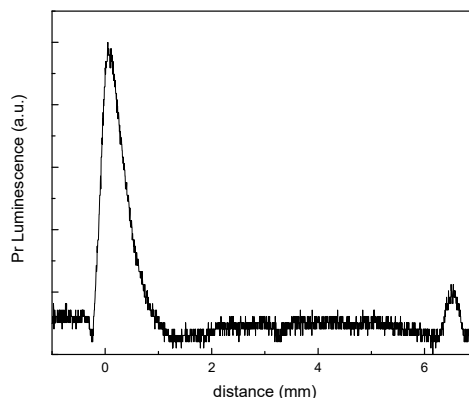


Figure 3.1.1. Intensity of PL under 1532 nm excitation as a function of distance from the facet that was in contact with Pr metal.

A sealed ampoule was annealed at 950°C for 7 days. Pr diffusion was enhanced by means of simultaneous gamma-irradiation during the thermal diffusion process with a power dose of 44R/s. During the annealing, one of the facets of the ZnSe crystal was in direct contact with liquid Pr metal. The samples were slowly cooled down to RT and characterized.

Experimental results and discussion

The spatial distribution of Pr^{3+} ions was measured using photoluminescence signal at ${}^3\text{P}_0 \rightarrow {}^3\text{H}_6$ transition (610 nm) using confocal microscope with a spatial resolution better than 10 μm . 532 nm radiation of second harmonic of single frequency Nd:YAG laser was used as a pump source. Figure 3.1.1. shows intensity of the PL signal as a function of position of the excitation spot. As one can see from the Figure, the PL from the crystal surface exposed to Pr diffusion from the liquid phase (left edge) was ~ 10 times bigger than that from the opposite side of the crystal. The diffusion length of praseodymium was estimated to be ~ 0.5 mm.

The mid-IR PL spectra were measured under excitation with 1532 nm Er-fiber laser radiation. Figure 3.1.2A demonstrates PL spectrum with a strong luminescence band centered at 2.4 μm corresponding ${}^3\text{F}_3 \rightarrow {}^3\text{H}_5$ transition of Pr^{3+} . Kinetics of photoluminescence were also measured in the 2-3 μm spectral range under excitation with a Q-switched, 532nm radiation of frequency doubled Nd:YAG laser with a pulse duration of 5ns. As one can see in Figure 3.1.2B, the kinetics exhibit non-exponential decay similar to that demonstrated in other materials doped with Pr^{3+} [42,43,44].

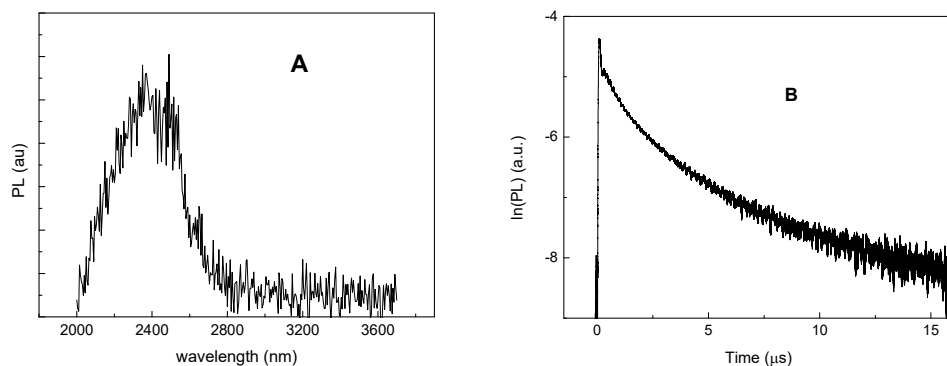


Figure 3.1.2 A) PL spectrum of Pr:ZnSe under 1532nm excitation. B) Kinetics of Pr:ZnSe PL under 532nm pump

Conclusions

Pr:ZnSe samples were fabricated using radiation enhanced post growth diffusion method. The spatial distribution of Pr ions measured with confocal microscopy shows that post growth thermal diffusion is a viable method of doping II-VI materials with Praseodymium. We have also studied ${}^3\text{F}_3 \rightarrow {}^3\text{H}_5$ mid-IR PL and kinetics of Pr^{3+} ions in ZnSe under visible and 1532 nm excitations. Novel low phonon spectrum Pr:ZnSe crystals are potentially promising mid-IR gain media.

3.2 Diffusion doped Er:ZnS and Er:ZnSe laser active powders

Erbium doped ZnS and ZnSe samples were prepared by thermal diffusion method. ZnS and ZnSe powders (Alfa Aesar) were mechanically mixed with ErF₃ (Sigma Aldrich) to 1.8% molar concentration. Powder samples were placed in quartz ampules and sealed under 10⁻³ Torr vacuum. Ampules were annealed at 950°C for 84 hours. Figure 9.1 shows Erbium doped ZnSe and ZnS powders in quartz ampules after annealing. Ampules were carefully opened, and the powders were studied using micro-Raman system.



Figure 3.2.1. Erbium doped ZnSe and ZnS powders sealed in quartz ampules.

Grain size of Erbium doped powders was studied using optical microscopy method. Figure 3.2.2 shows optical microscope image of Erbium doped ZnS powder after 84h annealing at 950°C. It can be seen that grain size was ranging from 1 μm to 10 μm and has not shown considerable grain growth comparing to starting materials. It is also seen that ZnS has a pink coloration corresponding to Erbium impurities.

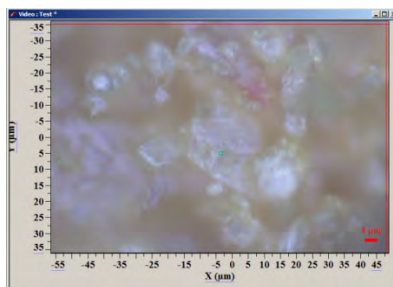


Figure 3.2.2 Optical microscope image of Erbium doped ZnS powder

Photoluminescence of Erbium doped samples was studied using Horiba Jobin Yvon LabRam HR Micro-Raman System equipped with 800 mm focal length spectrometer (HR 800 UV) optimized for the 200-1600 nm spectral region. Radiation of Argon-Ion laser operating at 514 nm was used for excitation. Figure 3.2.3a shows PL spectrum of Erbium doped ZnS powder. The PL spectrum showed characteristic Erbium emission bands around 550 nm, 850 nm, and 980 nm. The similar studies were performed with Erbium doped ZnSe powder sample. Figure 3.2.3b shows PL spectrum of Erbium doped ZnSe powder. The PL of Erbium doped ZnSe showed a strong and wide featureless band in 500-900nm spectral region (not show in Figure 3.2.3) presumably due to vacancies formed during annealing and doping process. The PL of these centers was strong enough to mask any signal due to Erbium in 500-900 nm spectral region. We were able to observe characteristic Erbium PL signal at around 970 nm as show in Figure 3.2.3b. The signal at wavelength longer than 1000 nm corresponds to visible light diffracted to the second order of the grating.

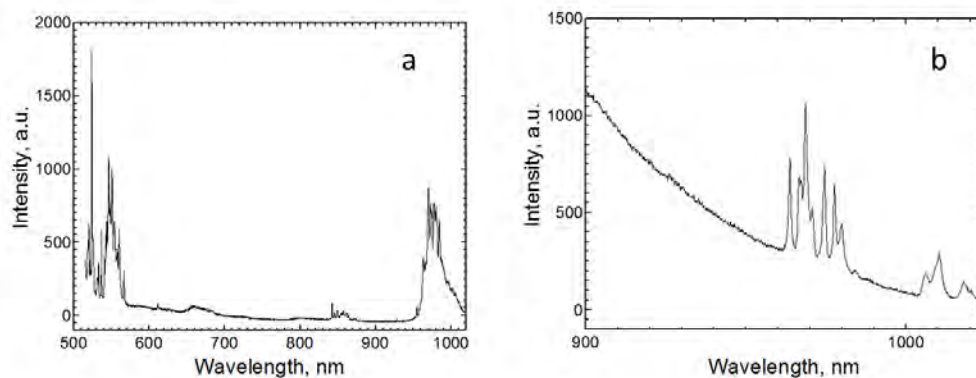


Figure 3.2.3. Erbium photoluminescence in a) ZnS and b) ZnSe powders under 514 nm excitation.

4. Electrically pumped transition metal doped II-VI semiconductor materials

4.1 Electrical Characterization And Electroluminescence Of Thin Film Structures

4.1.1 Electrical Properties of Thin Film Structures Containing Cr²⁺:ZnSe Layers.

Understanding the specific phenomena that govern the electrical properties of our ZnSe-based multilayer structures is essential for achieving our goal of an electroluminescent device. The PLD-grown films exhibit a substantial concentration of extended defects that will inevitably affect their electrical transport characteristics. Even the epitaxially-oriented films have large dislocation densities, and polycrystalline films are the norm above a critical thickness of 100-220 nm. The potential impact of grain boundaries must therefore be considered in the electrical properties. This is in addition to the well-established understanding of the effect of ohmic and/or rectifying junctions at the various metal/semiconductor and semiconductor/semiconductor interfaces in our structures. Grain boundaries may feature localized trap states that may need to be mitigated to achieve acceptable resistivities for electrical excitation. In order to study these effects, several multilayered thin film structures were produced and their electrical properties were correlated with sample characteristics, including thickness and crystal structure of the primary layers.

4.1.2 Structures Designed for Electrical Studies

A series of multilayered samples with the architecture shown in Fig. 4.1.1 were deposited for a study to relate the crystallographic and electrical properties of the samples. The main parameter varied in these thin film structures was the thickness t of the Cr²⁺:ZnSe layer as listed in Table 1. The XRD measurements shown in Fig. 4.1.2 allow an assessment of how the number of grain boundaries varies in these various structures. The patterns in Fig. 4.1.2 reveal that as the thickness of the Cr²⁺:ZnSe layer is increased,

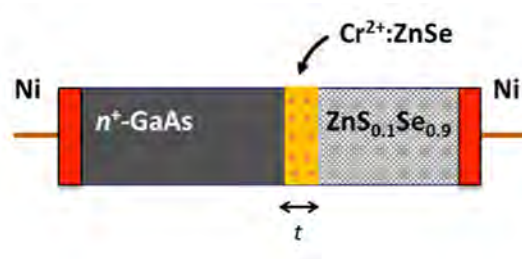


Figure 4.1.1. Layout of thin film structures designed for electrical characterization. The structure allows evaluation of the resistivity of the Cr²⁺:ZnSe and ZnS_{0.1}Se_{0.9} layers as well as interfaces.

Table 4.1.1. Material Layer Thicknesses of Deposited Thin Film Structures

##	ZnS _{0.1} Se _{0.9} Layer (nm)	Cr ²⁺ :ZnSe Interfacial Layer (nm)	Substrate
1	300	0 (no Cr ²⁺ :ZnSe layer)	n-GaAs
2	300	150	n-GaAs
3	300	300	n-GaAs
4	300	450	n-GaAs
5	300	600	n-GaAs

the intensities of the reflections that are “non-epitaxial” with respect to the substrate increase relative to the intensity of the “epitaxial” reflection. The increase in the relative peak heights of the non-epitaxial peaks indicates a trend away from epitaxial orientation and consequent increase in number of grain boundaries due to crystal misalignment of adjacent grains. Relative peak intensities were determined from the XRD patterns displayed in Fig. 4.1.2 and are listed in Table 4.1.2.

Most of the diffraction peaks observed in the XRD data in Fig. 4.1.2 are found at values of 2θ that lie somewhere in between the predicted values for ZnSe and ZnS for a common crystal plane, so these peaks are being referred to here as the Zn(S)Se group rather than by the independent diffraction peak locations of ZnSe and ZnS. The peaks P₁, P₂, and P₃ referenced in Fig. 4.1.2 and Table 4.1.2 refer to the Zn(S)Se (111), Zn(S)Se (200), and Zn(S)Se (220) growth peaks, respectively, and the intensities of these diffraction peaks were all measured relative to the Zn(S)Se (311) primary growth peak (P_{ref}) as observed in the XRD glancing angle 2θ data. While the P₁ Zn(S)Se (111) and P₂ Zn(S)Se (200) peaks were observed to increase for samples #3-5 as a function of thickness of the Cr²⁺:ZnSe layer, the P₃ Zn(S)Se (220) growth peak showed a less significant increase in relative height. The increase of relative peak height of the non-epitaxial growth peaks as a function of increasing thickness of the Cr²⁺:ZnSe layer indicate an increase in polycrystalline features such as number of crystallites, grain boundaries and mosaicity within the layer.

Table 4.1.2. XRD Diffraction Peak Intensities measured relative to Primary (311) Zn(S)Se Growth Peak in Deposited Thin Film Structures

##	P ₁ / P _{ref}	P ₂ / P _{ref}	P ₃ / P _{ref}
3	0.026	0.049	0.018
4	0.059	0.061	0.026
5	0.078	0.064	0.026

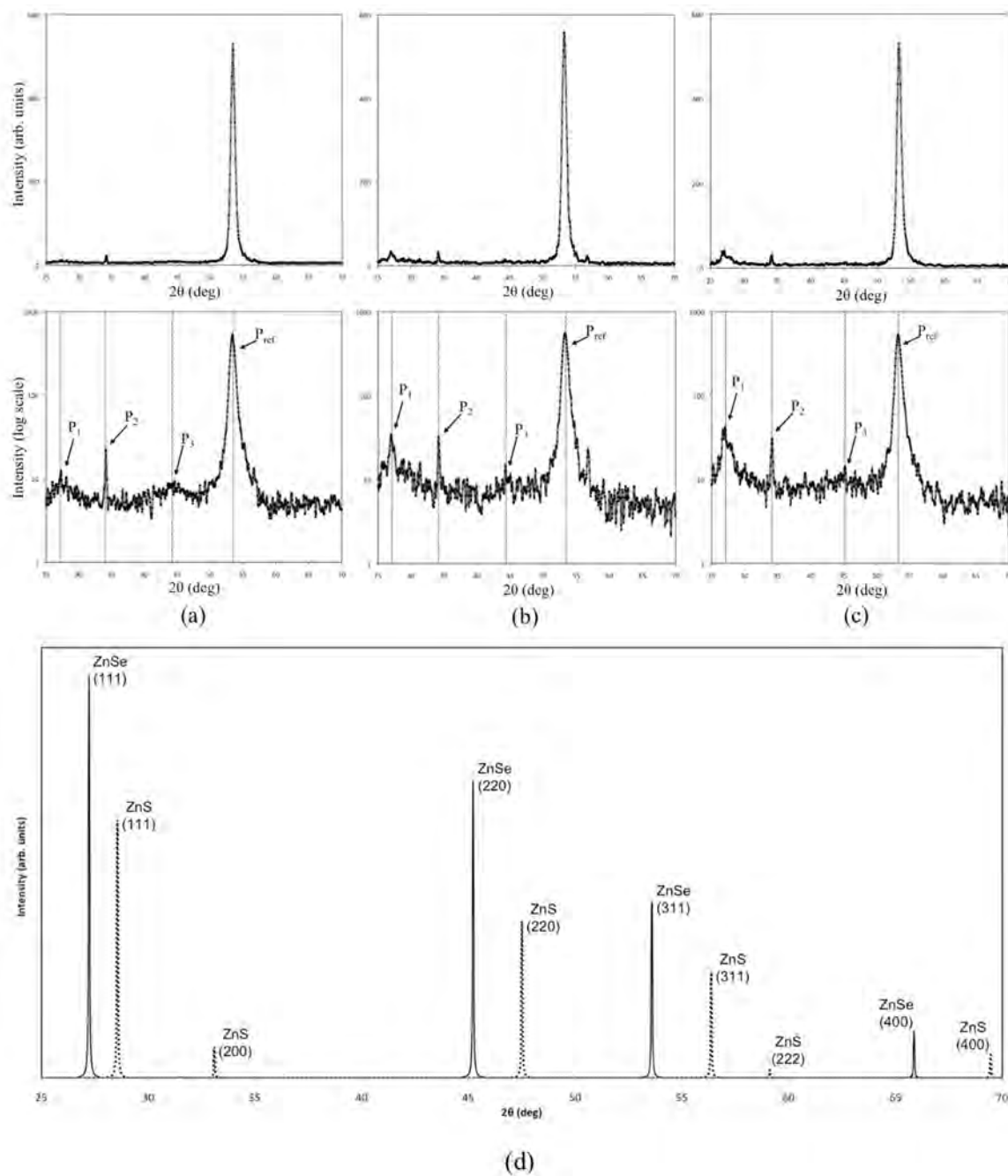


Figure 4.1.2. XRD Glancing Angle 2θ Scans of polycrystalline thin film structures showing relative heights of various observed diffraction peaks displayed in linear (top row) and logarithmic scale (middle row) for (a) sample #3, (b) sample #4, and (c) sample #5, along with (d) standard diffraction patterns for ZnSe (cubic) and ZnS (cubic) for comparison

4.1.3. Analysis of the Grain Boundary Resistivity of the Cr²⁺:ZnSe Layer

An essential characteristic of the grain boundary resistance expected to dominate the electrical behavior of the Cr²⁺:ZnSe layer is the barrier height of the Schottky-like junctions at the boundaries, as illustrated in Fig. 3. In all structures analyzed in this study, we identify two primary mechanisms driving current flow, each becoming dominant in a specific voltage regime. At low bias voltages (< 0.1 V), carrier tunneling is the dominant process for charge transport. Conversely, thermionic emission dominates at high bias voltages (approaching 0.5 V) as the Fermi level is raised closer to the conduction band edge. These trends are observed by fitting theoretical models to the I-V data, using carrier tunneling or thermionic emission as the dominant processes of charge transport in the appropriate voltage regime. Theoretical values of the tunneling current density were calculated using the following expression [45]

$$J_t \sim A^{**} B e^{-q\phi_B/E_{00}} e^{qV/E_{00}} \quad (1)$$

where

$$E_{00} = \frac{q\hbar}{2} \sqrt{\frac{N_D}{\epsilon_s m^*}} \quad (2)$$

where E_{00} is an energy constant of the material and is associated with the WKB expression for the transmission of the barrier [46]. For the theoretical model of the tunneling current, the relative permittivity of ZnSe ($\epsilon_s=9.1\epsilon_0$) and effective electron mass in the ZnSe system ($m^*=0.17m_e$) [47] were used in conjunction with barrier heights extracted from current-voltage data to formulate theoretical fits to the experimental values of current density versus voltage, using N_D and B as fitting parameters (where B is a parameter related to the temperature and Fermi level in the semiconductor).

The tunneling contribution to charge transport appears to be the dominant process for net current flow in all structures at low voltages, while thermionic emission becomes dominant at higher voltages (see Fig. 4.1.4). As the number of polycrystalline features increase throughout the structures (as observed in the XRD data), the transition of the dominant current flow process from tunneling to thermionic emission is observed to shift towards lower bias voltages. This is possibly due to a more pronounced narrowing of the double-Schottky barriers throughout structures with increased dislocation densities and polycrystalline features relative to structures displaying superior crystal quality.

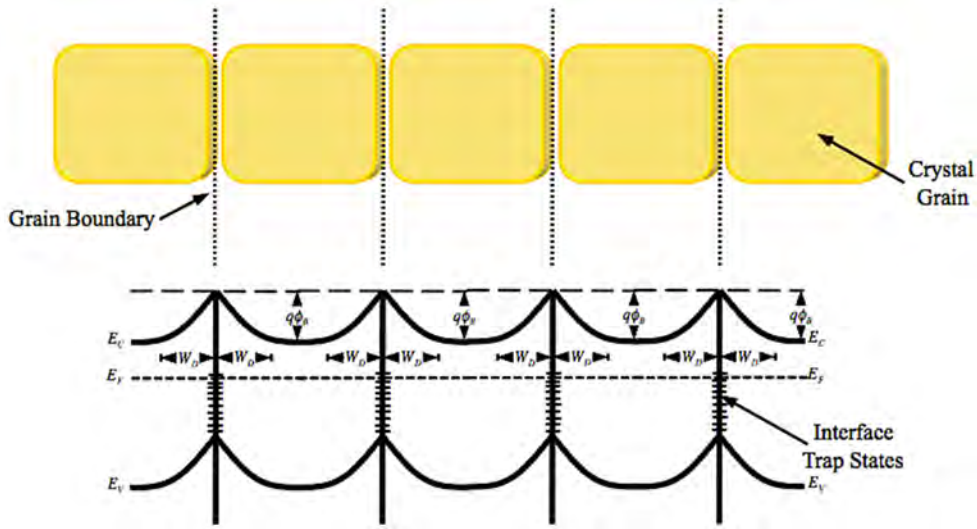


Figure. 4.1.3. Expected double Schottky-like band edge profile at grain boundaries in the ZnSSe film. Increasing applied voltages lead to reducing resistances due to growing leakage currents through potential barriers.

Since all structures in this study display a closer fit to a thermionic emission model at voltages approaching 0.5 V, barrier height determination via the thermionic emission method is utilized in this voltage range. By plotting the natural log of the current density versus applied bias voltage, the effective barrier height is extracted from the “y-intercept” of the extrapolated linear fit to the log-linear region (see Figs. 5 & 6). Effective barrier heights determined from the current density versus bias voltage data are listed in Table 4.1.3, along with corresponding values for the specific contact resistance of the junctions which were calculated by [48, 49]

$$R_C = \left(\frac{\partial J}{\partial V} \right)_{V=0}^{-1} \quad (3)$$

Eq. 3 can be further developed to yield

$$R_C = \frac{k}{qA^{**}T} e^{q\phi_B/kT} \quad (4)$$

Inserting material parameters and known constants into Eq. 4 gives a value for the specific contact resistance of the junction in units of $\Omega \cdot \text{cm}^2$. Dividing these values by the area of the contact (cm^2) gives a corresponding value of the resistance (Ω) contributed by the respective junction. Since Eq. 3 utilizes the partial derivative of the thermionic emission current density with respect to applied voltage, the calculated values of R_C are not expected to match the corresponding resistances of the Nyquist arcs with great accuracy at zero voltage, since tunneling appears to dominate over thermionic emission at low

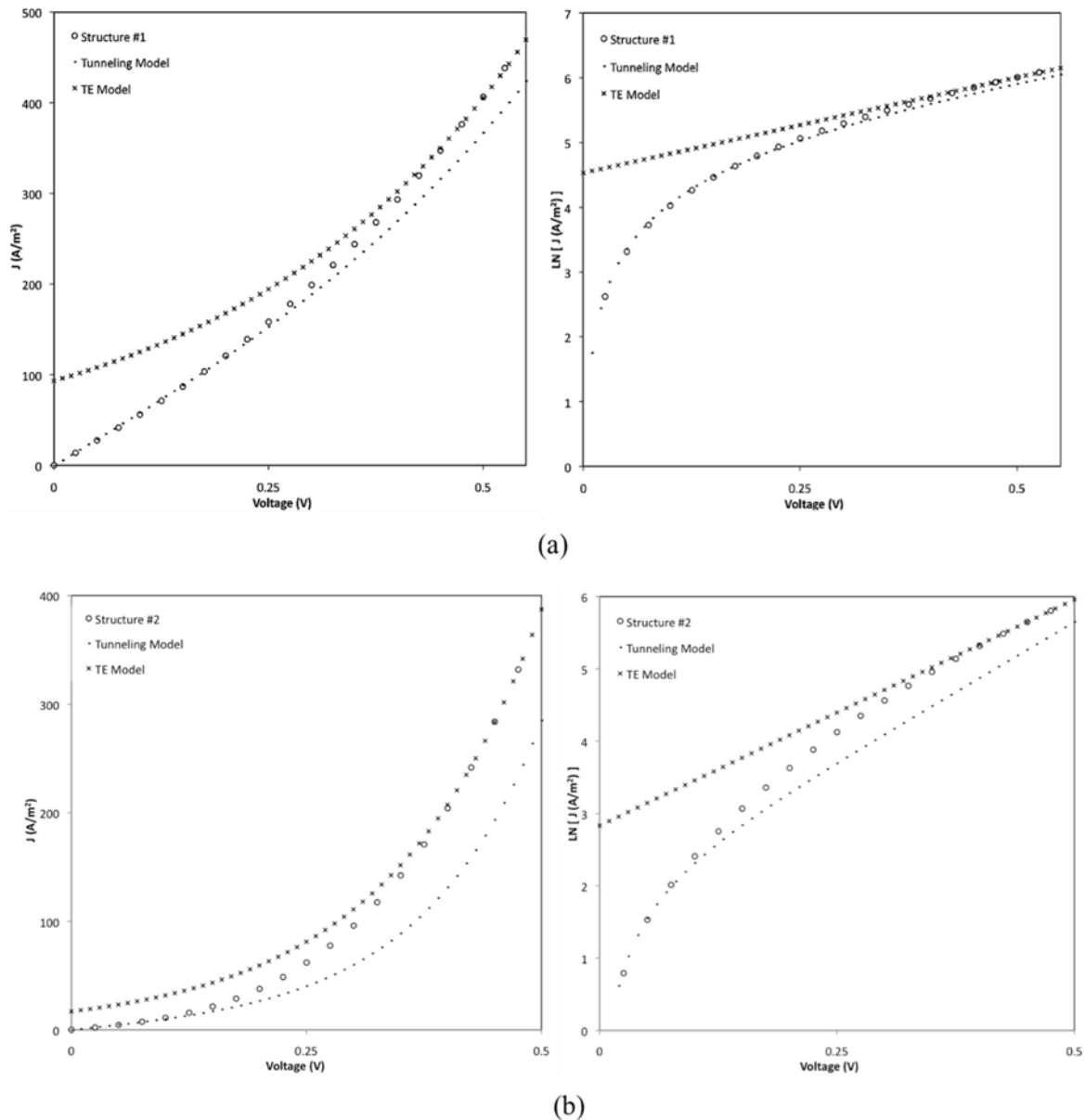


Figure 4.1.4. Linear and log scale plots of current density versus applied bias voltage for (a) structure #1 and (b) structure #2, showing the shift in the transition of the dominant current flow process of carrier tunneling to thermionic emission (TE) to increasing values of bias voltage as a function of sample polycrystallinity.

voltages (see Fig. 4.1.4). This trend is found for all structures with varying degrees of prevalence of tunneling and thermionic emission at low and high voltages, respectively.

Effective barrier heights listed in Table 4.1.3 were determined using the values of total current density measured for the respective structures. Values of specific contact resistance calculated from thermionic emission theory were consistently lower than the measured resistances displayed in the

impedance arcs at zero bias by a factor of ~ 4 . This underestimation of the net resistance of the potential barriers associated with the collection of grain boundaries is likely due to using the expression for thermionic emission to derive Eq. 4 rather than the expression for carrier tunneling shown in Eq. 1. Determination of these values of contact resistance via the tunneling equation was not possible due to the ambiguity of the parameter B within our structures.

Table 4.1.3. Values of Effective Barrier Height and Contact Resistance calculated from Current Density versus Applied Bias-Voltage Measurements on Deposited Thin Film Structures

##	Cr ²⁺ :ZnSe Layer (nm)	ϕ_B , (- V_{bias}) eV	ϕ_B , (- V_{bias}) eV	Rc/Area (- V_{bias}) Ω	Rc/Area (+ V_{bias}) Ω
1	N/A	0.509	0.505	6.7	5.7
2	150	0.553	0.557	165.4	193.0
3	300	0.592	0.597	404.4	490.2
4	450	0.639	0.638	1043.1	1003.7
5	600	0.662	0.690	1642.2	4820.8

The values of grain boundary resistance inferred from R_C and the overall resistance of the Cr²⁺:ZnSe allow the determination of an important figure of merit of the layer: the effective resistivity and how crystal quality of the structure may affect it. Table 4.1.4 displays relevant parameters and calculated values of effective resistivity for each layer present in the samples analyzed in this study. In order to extract values of resistance for the Cr²⁺:ZnSe layers in structures #2-5, the independent values of resistivity for the GaAs substrate and 300 nm ZnS_{0.1}Se_{0.9} layer (both with deposited Ni contacts) were calculated using the equivalent circuit model method applied to the GaAs sample and structure #1.

Resistivity values of 31 Ω ·cm and 1.95×10^5 Ω ·cm were calculated for the Ni/GaAs/Ni system and ZnS_{0.1}Se_{0.9} layer, respectively. These values of resistivity, in conjunction with extracted values for the specific contact resistance for the Schottky junctions present in each sample, were applied to subsequent equivalent circuit models of samples #2-5 to isolate values of resistance solely contributed by the Cr²⁺:ZnSe layers. These resistances were then used, along with relevant sample parameters, to calculate upper bounds to the effective resistivity (ρ^*) of the Cr²⁺:ZnSe layer.

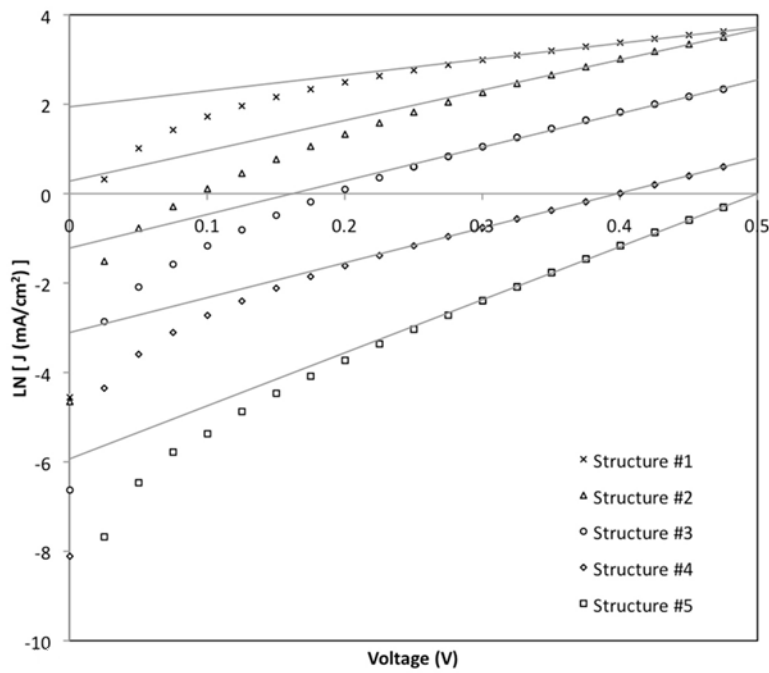


Figure 4.1.5. Natural log of current density versus *positive* applied bias voltage used in effective barrier height determination for structures #1-5

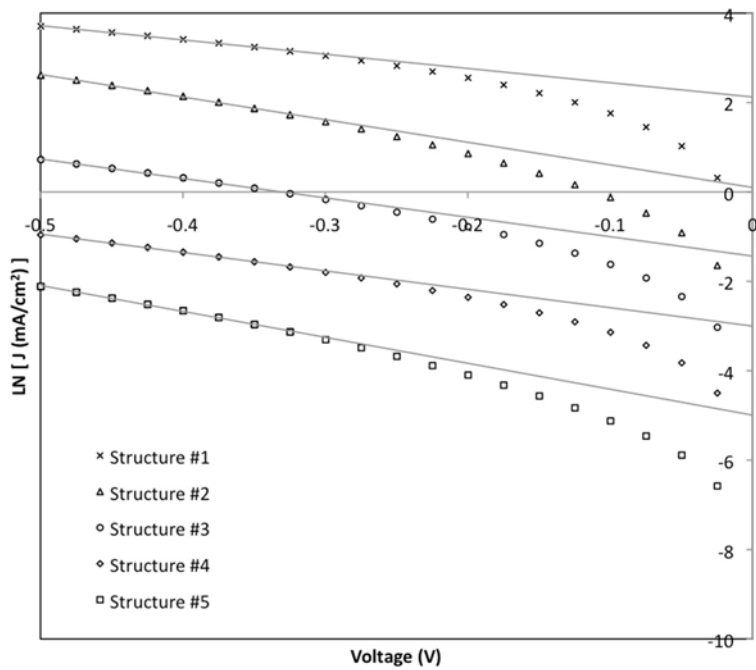


Figure 4.1.6. Natural log of current density versus *negative* applied bias voltage used in effective barrier height determination for structures #1-5

Table 4.1.4. Electrical Properties of Deposited Thin Film Structures

Sample	Contact Area (cm ²)	R _{Total} (Ω)	R _{Cr²⁺:ZnSe} (Ω)	ρ* _{Cr²⁺:ZnSe} (Ω.cm)
GaAs	0.55	2	N/A	N/A
1	0.45	13	N/A	N/A
2	0.12	1000	760	6.1×10 ⁶
3	0.22	2200	1755	1.3×10 ⁷
4	0.52	4070	3009	3.5×10 ⁷
5	0.80	20483	18830	2.5×10 ⁸

The observed increase in the effective resistivity of the Cr²⁺:ZnSe layer can be attributed to an increase in the number of grain boundaries with increasing layer thickness as confirmed by the XRD analysis.

For dopant concentration characterization, a slightly different approach must be taken from the conventional capacitance-voltage method due to the complex polycrystalline microstructure of these samples. Instead of using the relationship of the variation in total capacitance versus applied voltage, an approach utilizing the isolated capacitance of the grain boundaries must be taken. The equation relating the voltage-dependent nature of the grain boundary capacitance is given by [50]

$$\left(\frac{1}{C_{gb}} - \frac{1}{2C_{gb_0}} \right)^2 = \frac{2p^2}{qk\epsilon_0 N_D} \left(\phi_B + \frac{V}{p} \right) \quad (5)$$

where ϕ_B is the barrier height, V is the applied voltage, N_D is the dopant concentration, p is a normalization parameter dependent on the number of active barriers within the material, and C_{gb} and C_{gb_0} represent the grain-boundary capacitance under applied voltage V and $V=0$, respectively.

4.1.4 Double Varistor Behavior of Epitaxially-oriented Cr²⁺:ZnSe/ZnS_{0.1}Se_{0.9} Structure

The varying degrees of crystallinity noted as a function of thickness in the structures discussed in Section 4.1.3 (structure #3-5) showed that the overall resistivity of the Cr²⁺:ZnSe layer scales with the number of grain boundaries in the film. This is consistent with our varistor model where the observed current is governed by tunneling through the numerous grain boundary regions in the polycrystal. It is also interesting to consider the varistor behavior of structure #2, which contains a Cr²⁺:ZnSe that is epitaxially-oriented with respect to the GaAs substrate. The Cr²⁺:ZnSe layer in structure #2 has $t = 150$ nm, which is at or below the critical thickness for epitaxy of ZnSe on GaAs. Despite epitaxial orientation, this highly textured sample is unlikely to be a single crystal given the typical levels of mosaicity seen in PLD-grown films.

Nevertheless, the lower overall resistance of the $\text{Cr}^{2+}:\text{ZnSe}$ varistor allows the observation of additional impedance features in the range of applied voltages accessed in our experiments. This is seen in Fig. 4.1.7, which shows the impedance arcs for the 150-nm $\text{Cr}^{2+}:\text{ZnSe}$ sample for applied voltages of both polarities. As was the case for the structures with thicker layers, the large varistor arc that dominates the impedance plane shows decreasing resistance with applied voltage. The behavior is approximately symmetric with respect to polarity reversal as also noted for the greater thicknesses. However, at sufficiently high applied voltages ($V = +0.225$ V, positive polarity; $V = -0.475$ V, negative polarity), a second arc manifests itself in the impedance plot. This second arc becomes particularly clear in the case of $V > 0$, shown magnified in the bottom region of Fig. 4.1.7. Both arcs change with applied voltage, which rules out their origin in conduction processes of the grain interiors. Their characteristic magnitudes,

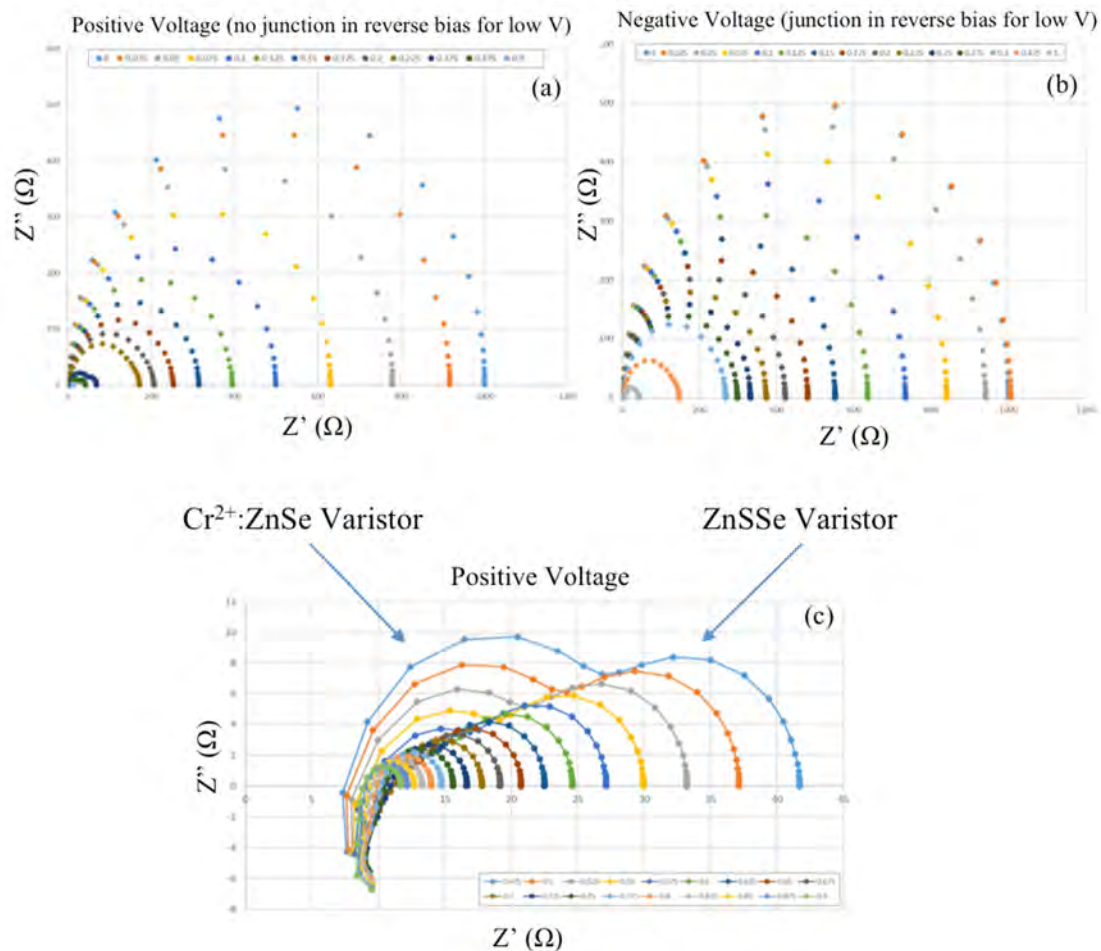


Figure 4.1.7. Impedance of structure #2 containing an epitaxially-oriented $\text{Cr}^{2+}:\text{ZnSe}$ layer of 150-nm thickness under (a) positive and (b) negative polarities. Panel (c) shows the arcs obtained at higher voltages for positive applied voltage. Both arcs are clearly voltage dependent, with resistance decreasing with applied voltage, consistent with their assignment to the $\text{Cr}^{2+}:\text{ZnSe}$ and ZnSSe varistors as indicated in the figure.

dependence of relaxation frequency, and a comparison with the ZnSSe (structure#1) impedance reveal that the low frequency arc, which is new arc to emerge, represents the ZnSSe varistor layer. As voltage increases, the resistance of the ZnSSe decreases as tunneling currents grow through the Schottky-like barriers in reverse in that layer. On the other hand, the high-frequency arc, which is also voltage-dependent, originates in the Cr²⁺:ZnSe varistor. The high frequency of the Cr²⁺:ZnSe varistor arc (in excess of 1 MHz) is a result of the very low resistance and capacitance of this layer under high applied fields. As the applied voltage increases, the resistivity of both varistor layers becomes very small, leading to high currents in the overall structure.

4.1.5 Asymmetry of the Impedance Characteristics of the Cr²⁺:ZnSe Layers

All structures containing Cr²⁺:ZnSe layers exhibit some level of asymmetry in the impedance with respect to polarity reversal. Since the varistor behavior is essentially associated with polycrystalline structures, whose grain boundaries are randomly oriented, the varistor scenario in the Cr²⁺:ZnSe and ZnSSe layers cannot account for the observed impedance asymmetry. One must invoke the presence of at least one rectifying junction in these structures that is under reverse bias when the applied voltage has negative polarity (thereby increasing the resistance of the structure). The three interfaces indicated in Fig. 4.1.8 (labeled A, B, and C) are in principle candidates for such a rectifying junction.

Interface “A” is an unlikely candidate because the n⁺-GaAs/Cr²⁺:ZnSe interface probably results in ohmic behavior after annealing and passivation of interface states. This is because the work function of the degenerate GaAs (≤ 4.09 eV) is certainly less than the work function of Cr²⁺:ZnSe ($\sim 5.0 \pm 0.5$ eV), and the band offset in the conduction band of this interface (≤ 300 meV), is not sufficient to create a Schottky barrier. Even in the improbable case that an interface state with appreciable concentration remains at interface “A,” leading to a Schottky junction, such a junction would be in forward bias when a negative voltage is applied to the structure, which cannot explain our results. Interface “B” is also unlikely to be source of rectification because no barrier was detected for negative applied voltages in samples with an identical interface. We therefore tentatively assign the rectifying behavior in the structures containing a Cr²⁺:ZnSe to a “p-n junction-like feature” at interface “C,” as illustrated in Fig. 4.1.9. The fact that the Ni/ZnS_{0.1}Se_{0.9} interface shows no rectification suggests that the work function of ZnS_{0.1}Se_{0.9} is approximately equal or greater than the corresponding value for Ni (i.e., 5.2 eV). This places the Fermi level in the ZnSSe at least 5.2 eV below the vacuum level. This is consistent with the high resistivity of our ZnSSe layers ($\sim 10^5$ Ω ·cm). On the other hand, the high density of high-lying states associated with the Cr²⁺ dopant in ZnSe, suggests that the Fermi level in Cr²⁺:ZnSe could be above the one for ZnSSe. If realized, these circumstances produce a junction that would be in reverse bias when an negative polarity

is applied to the structures containing the $\text{Cr}^{2+}:\text{ZnSe}$, in qualitative agreement with the observed behavior of our samples.

Although plausible, this scenario needs to be verified by additional experiments. Adjustment of the Fermi level in ZnSSe by intentional n -type doping, correlated with impedance measurements would be one route to confirm or rule out this interpretation of rectification in these structures.

At the writing of this report, we are refining the parameters in the analysis of the electrical properties of these multilayers and plan on submitting a manuscript for publication of these results in IEEE Transactions on Electron Devices.

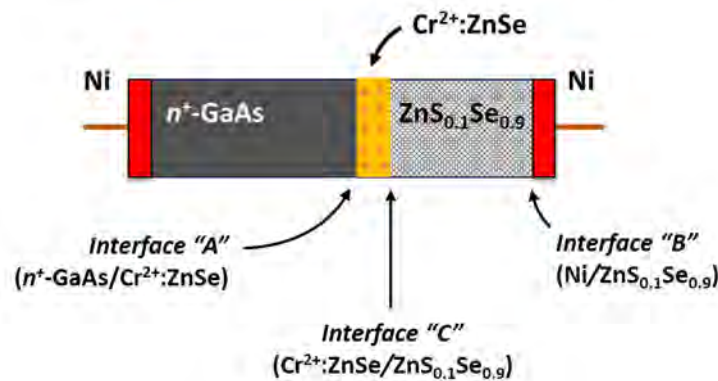


Figure 4.1.8. Schematic of the structures containing a $\text{Cr}^{2+}:\text{ZnSe}$ layer and the candidate interfaces (labeled A, B, and C) for a junction providing current rectification under negative applied bias voltage.

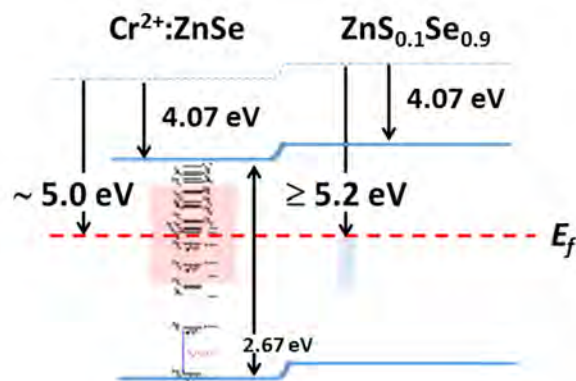


Figure 4.1.9. p - n junction-like interface posed to be present at $\text{Cr}^{2+}:\text{ZnSe}/\text{ZnS}_{0.1}\text{Se}_{0.9}$ heterojunction, likely providing current rectification under negative applied bias voltage

4.2 Electroluminescence in Thin Film Structures Containing Cr²⁺:ZnSe Layer

4.2.1 Structure and Crystallographic Characteristics.

The substrate chosen to be the deposition platform for a Cr²⁺:ZnSe electroluminescent structure was composed of a thin layer of conductive indium tin oxide (ITO) on top of glass. The ITO/Glass substrates were selected over GaAs for this application due to high electrical conductivities of ITO thin films and high optical transmission in the spectral region of interest for potential mid-IR emission. However, deposition of polycrystalline films of ZnSe was expected due to the large mismatch in lattice parameter between cubic ZnSe (5.668 Å) and cubic ITO (which is typically ~10 Å but varies with the composition of Sn in the alloy) [51].

Thin films (~3-4 μm) of Cr²⁺:ZnSe were deposited onto ITO/Glass substrates via PLD using a Cr²⁺:ZnSe ablation target produced in-house by mixing appropriate masses of ZnSe powder and CrSe powders (both 99.999% purity) to achieve a nominal Cr concentration of ~1.2×10²⁰ cm⁻³. In order to utilize the conductive ITO layer beneath the deposited film as an electrode, rectangular Si masks (~1 cm²) were installed on top of the ITO surface before thin film deposition as illustrated in Fig. 4.2.1.

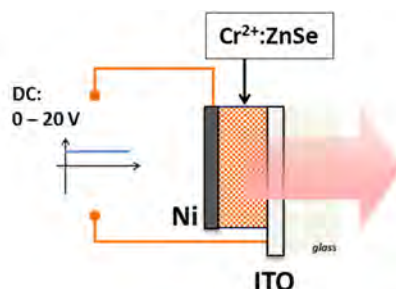


Figure 4.2.1. Schematic illustrating masking process implemented during thin film deposition leaving a portion of exposed ITO to act as the bottom electrode and deposited Ni contact atop the film to act as the top electrode for applying voltage across the Cr²⁺:ZnSe thin film in mesa geometry for electroluminescence measurements

Thin film deposition was performed at a growth temperature of 450°C, which resulted in a polycrystalline Cr²⁺:ZnSe film with a predominant (111) orientation. Subsequent depositions were performed at different growth temperatures (500°C, 550°C), and the effect of temperature on the crystal orientation of the film was negligible within this range. Following thin film deposition, the chamber was allowed to cool to room temperature before breaking vacuum to remove the sample for top contact deposition. The Si mask was removed, exposing the bare ITO to be used as the bottom electrode, and

circular Ni contacts (0.4 cm^2) were deposited atop the $\text{Cr}^{2+}:\text{ZnSe}$ film via magnetron sputtering for electroluminescence measurements.

4.2.2 Visible Electroluminescence in $\text{Cr}^{2+}:\text{ZnSe}$ Thin Films

Before electroluminescence measurements were attempted, the structure was tested for electrical characteristics via EIS measurements. Applied DC voltages ranged from 10–20 V, resulting in corresponding current densities of 16.5–30 mA/cm^2 through the sample. A maximum current of 12 mA through the sample was achieved with an applied voltage and electric field of 16.7 V and 42 kV/cm , respectively. DC voltages were applied via a 2-point probe setup utilizing mesa geometry orientation with the sample mounted vertically on an optical collection platform (designed in-house) to be used in synchrony with a Fluoromax UV-VIS Optical Spectrometer to obtain electroluminescence spectra.

To ensure proper functionality of the spectrometer, the emission spectrometer was calibrated using a water Raman calibration scan that utilized both the excitation and emission spectrometers of the device. However, since the excitation spectrometer component of the Fluoromax was not necessary for collection of emission via electrical excitation, an additional calibration procedure using an external 447 nm blue laser was implemented to assure proper alignment of the emission spectrometer. Before applying voltage across the structure, the sample-mounted platform was placed inside of the collection chamber of the spectrometer. To determine the optimal orientation of the sample to maximize collection of emitted light, a green light-emitting diode (LED) was powered at the sample location and horizontal and vertical adjustments were made while monitoring counts with the emission spectrometer fixed at the peak wavelength of the alignment LED.

While applying voltage across the sample, the emission spectrometer was scanned through a wavelength range of 400–900 nm over a period of 6–12 hours for each value of applied voltage. To verify that the spectra obtained from the scans was indeed emission from the sample under electrical excitation, the emission spectrometer was fixed at the peak emission wavelength from the sample spectrum, and the applied voltage was toggled on and off by modulating the power supply until a square-wave-like behavior was observed from the detector (see Fig.4.2.1). Considering the low intensity of emission due to impact ionization expected in this geometry from such a thin film of $\text{Cr}^{2+}:\text{ZnSe}$, no signal was detectable until a voltage of 10 V was applied to the sample. As the applied voltage was increased within the range of 10–20 V, the intensity of emission increased (as shown in Fig. 4.2.3) until device failure was realized at 19.2 V with an applied electric field of magnitude 48 kV/cm .

The electroluminescent emission spectrum obtained from the sample shows a broad peak centered at $\sim 650 \text{ nm}$ ($\sim 1.9 \text{ eV}$) that can be primarily attributed to deep centers due to crystal defects such as vacancies, interstitials, or other impurities in ZnSe [52]. Possible sources of emission in the detected range

are attributed to defects such as Zn vacancies (2.06 eV), Cu impurities (1.95 eV), and Cl impurities (2.05 eV) in ZnSe [53, 54].

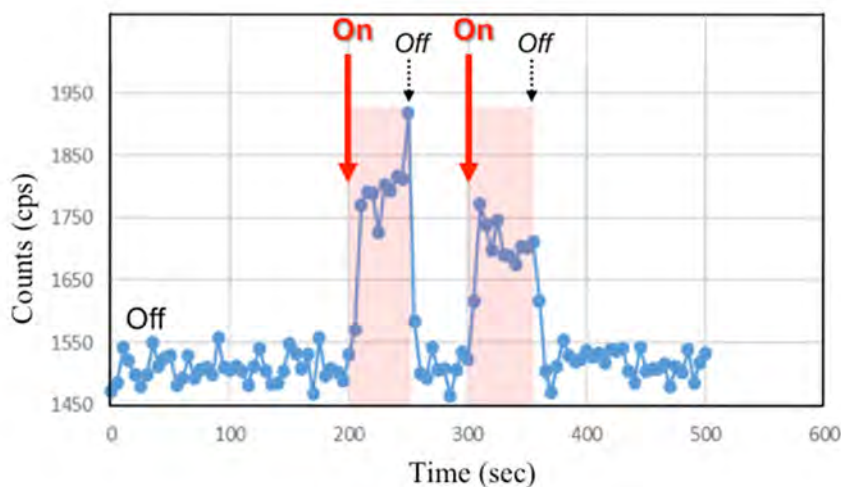


Figure 4.2.2. Detected signal from emission spectrometer of ZnSe/ITO/Glass sample under toggled electrical excitation (14.2 V, 10.6 mA, 26 mA/cm²)

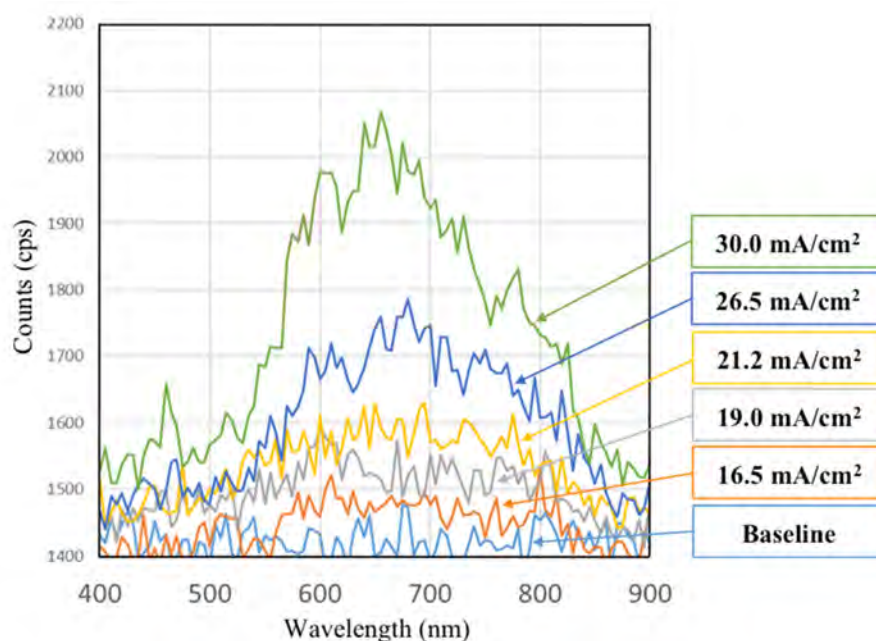


Figure 4.2.3. Electroluminescent signal versus emission wavelength of ZnSe/ITO/Glass sample under electrical excitation achieving the displayed current densities with increasing magnitude of applied voltage

In addition, the acceptor nature of Cr²⁺ ions and the established contribution of holes to the valence band under optical excitation with photon energy greater than ~1.9 eV [55], as well as absorption

by chromium ions due to sub-band excitation [⁵⁶], could partially contribute to the low measured intensities of emission in this 400-900 nm spectral region. If there is quenching in this region due to free hole formation, these holes may subsequently be captured by a Cr ion, which will result in Cr excitation and possible emission of a photon in the mid-IR spectral region [⁵⁷].

In addition to obtained visible luminescence, an electroluminescent signal was also detected within the 2-3 μm spectral range with a similar experimental setup utilizing low and high pass optical filters and a Ge optical detector, but the intensity of emission was too weak to obtain a spectrum of the detected luminescence. This result is promising for future investigation of mid-IR emission from similar $\text{Cr}^{2+}:\text{ZnSe}$ thin film structures. Possible future directions to explore include similar visible electroluminescence measurements as a function of decreasing temperature to observe the effect of temperature on the emission spectra, as well performing mid-IR electroluminescence measurements on similar Cr-doped samples with various thicknesses and multilayered geometries using an optimized infrared spectroscopic setup.

4.3. Electrical Characterization of bulk Cr(Fe):ZnSe Laser Active Materials

One of the tasks of the project was study of an influence of electrical carriers in n-type ZnSe on spectroscopic properties of crystals. While the electrical carriers could possibly make n-type ZnSe crystals conductive enough for electrical excitation, absorption of carriers may reduce optical quality of the crystal. In addition, a study was done to determine if the process by which the doped crystals were produced could be sped up. All of the crystals that were doped with TM materials were done so using post-growth thermal diffusion. This process involves annealing the samples in a vacuumed ampoule at very high temperatures for several days sometimes weeks. The short diffusion length of these materials especially Fe^{2+} is the reason as to why the process takes so long. To increase speed and efficiency at which the TM doped II-VI materials are fabricated, a procedure called electrolytic coloration was also examined. It involves running a high voltage through the dopant film and the crystal while they are being annealed. The produced electric field would push the positively charged TM ions towards the cathode, which in turn would enhance the diffusion rate of the diffuser

Sample Preparation and Experimental Setup

The CVD ZnSe samples used for electrical characterization were similar to the samples used for spectroscopic characterization. To fabricate conductive samples, the ZnSe polycrystalline were sealed with aluminum cuts in quartz ampule vacuumed to 10^{-5} torr. The ampules were annealed at $T=1000\text{C}$ during 1-10 days. The annealed Al:ZnSe was then cut to about 1.6 millimeters, polished for absorption measurements. Spectra were taken with both the UV-VISNIR and the FTIR spectrophotometers.

To measure the electrical properties annealed Al:ZnSe, the indium contacts were deposited onto two sides of the crystal. The experimental setup for electrical measurements is depicted in Figure 4.3.1. The studied samples were connected in series with loading resistor $R_L=870\text{k}\Omega$. The pulse generator HP 214B was used as a voltage source (V_{in}) in our experiments. The digital oscilloscope TDS 744A was used to measure voltage drop across loading resistor (V_R). The electrical current in the scheme and electrical resistance (R_s) and resistivity (ρ) of the ZnSe samples calculated from these measurements

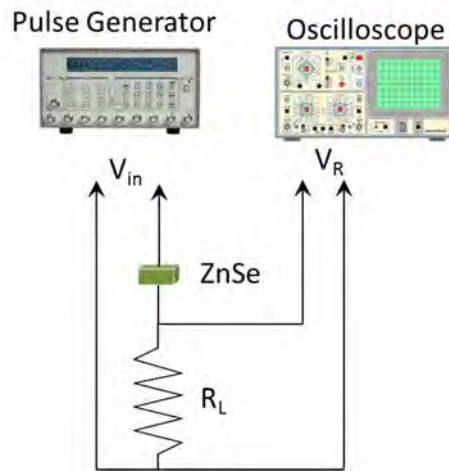


Figure 4.3.1 Experimental setup for electrical characterization

Experimental results and discussion

The I-V measurement of the one of the fabricated samples is shown in Figure 4.1.2. As one can see from this figure the result could be fitted by linear dependences for both applied voltage polarities. The calculated resistance and resistivity of this sample were measured to be $R_s=54k\Omega$, and $\rho=32k\Omega\text{cm}$ correspondingly.

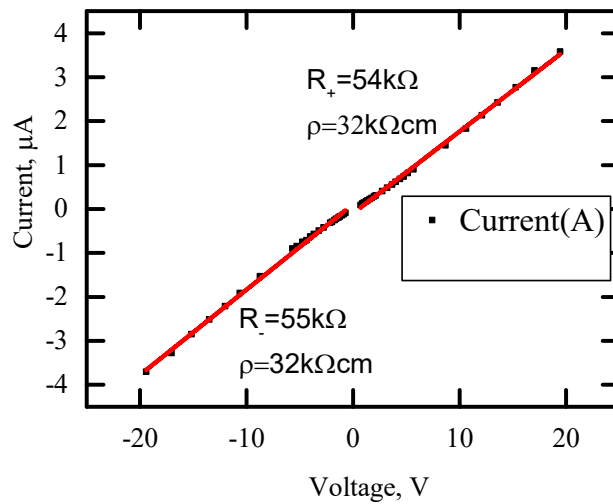


Figure 4.3.2 The I-V measurement of the n-type Al:Cr:ZnSe samples after annealing at 1000C in Al vapors

The transmission and absorption spectra of the n-type ZnSe samples are shown in the Figure 4.3.3

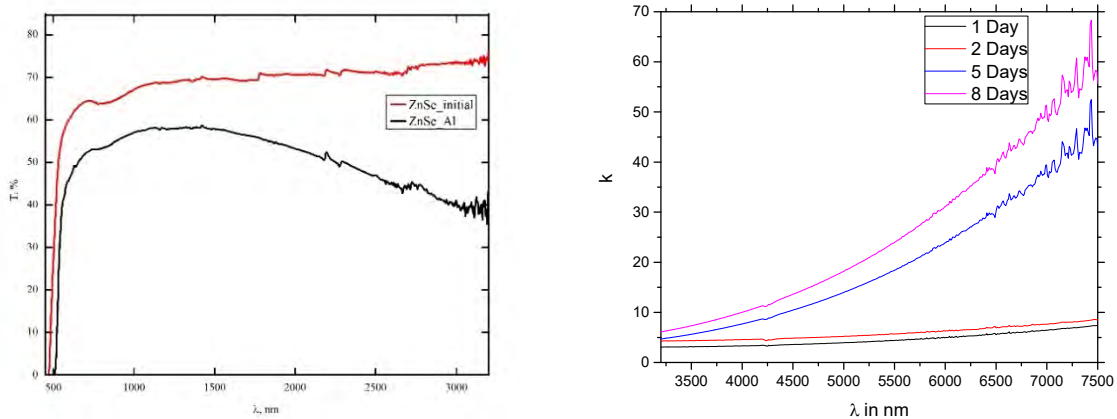


Figure 4.3.3. The transmission and absorption spectra of the n-type ZnSe samples annealed for 4 days (left) and for 1, 2, 5, and 8 days (right).

The left Figure shows transmission spectrum of the n-type ZnSe sample with resistivity $\rho=100\text{-}150\ \Omega\text{cm}$ after annealing for 4 days. The red curve shows initial transmission spectra. As one can see from the Figure, the conductive samples reveal strong passive absorption in the mid-IR spectral range induced by electrical carriers. For example, in the sample with resistivity $\rho=100\text{-}150\ \Omega\text{cm}$, the absorption coefficient of the induced losses in the maximum of the luminescence band of the Cr^{2+} ion at $2.4\ \mu\text{m}$ was measured to be $2.5\ \text{cm}^{-1}$. These losses should be minimized to achieve lasing under electrical excitation.

4.4. Electrical characterization TM:ZnSe samples at high temperatures

Electrical characterization of CVD grown polycrystals of ZnSe, Cr:ZnSe, and Fe:ZnSe were carried out as preliminary studies of feasibility of enhancement of TM diffusion under influence of high electric field, also known as electrolytic coloration. For this study conductivity of each sample was measured from 473-773K. Indium contacts were “ironed” on two largest parallel facets of the crystals, using soldering iron. The crystals were squeezed between two aluminum plates and copper leads were attached to the plates. Ceramic spacers were used to prevent shorting between the plates. The setup was placed in the furnace. And the leads were fit through the opening in the furnace. The other ends of the copper leads were connected to the same circuit

that was used to analyze Al:ZnSe in Figure 4.1.1. Input-output characteristics of the voltage were taken at RT, and at 100K increments starting with 373K up to 773K.

The slope of the I-V plots equal to the conductivity of the sample in the circuit. The graph of Logarithm of Conductivity vs 1000/Temperature was plotted as shown in Figure 4.2.1, which shows an exponential increase of the conductivity along with the increase in temperature. For example, conductivity of Fe:ZnSe rises at a rapid rate and already at 500°C is at $\sim 0.2 \text{ (k}\Omega\text{)}^{-1} \text{ cm}$. Extrapolating to 1000°C even higher conductivity is expected at level of $\sim 10 \text{ (k}\Omega\text{cm)}^{-1}$. Considering typical geometry of the samples currents of at least 100 A would be required to have 20kV voltage applied across the sample. This limits feasibility of application of the method due to unavailability of voltage sources that can provide both high voltage and high current at the required level.

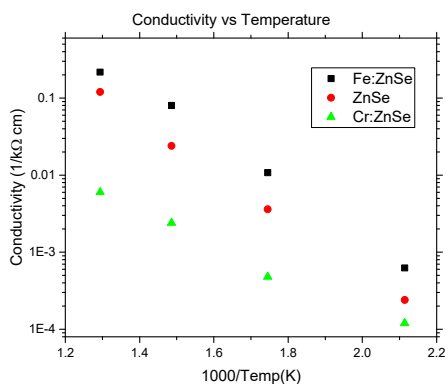


Figure 4.4.1. Temperature dependence of conductivity for Fe:ZnSe, Cr:ZnSe, and ZnSe.

Conclusions on Electrical Characterization of bulk Cr(Fe):ZnSe Laser Active Materials

Analysis of the absorption spectra of n-type Al:ZnSe and its electrical properties demonstrated increase of optical losses in the mid-IR spectral range induced by charge carriers. The optical losses at 2.4 μm was measured to be 2.5 cm^{-1} in the ZnSe sample with resistivity $\rho=100\text{-}150 \text{ }\Omega\text{cm}$

Finally, analysis of the electrical properties of (Fe)(Cr):ZnSe and their relationship to temperature demonstrated that the crystals could not be used for high voltage stimulation of the diffusion process. As was demonstrated heating of the TM:ZnSe results in a significant increase of the conductivity of the conductivity at elevated temperatures.

4.5 Ohmic Contact Formation in Al:Cr:ZnS(Se) crystals.

Another goal was study of Ohmic contact formation in n-type Al:Cr:ZnS(Se) crystals. All of the crystals were doped with TM(Cr, Fe) and Aluminum using post-growth thermal diffusion before contact formation. To measure the electrical properties of the n-type samples, metal contacts were deposited onto two sides of the crystals using plasma deposition methods. Several contact candidates were fabricated and tested on n-type Al:Cr:ZnSe and Al:Cr:ZnS samples using the deposition of metal thin films are summarized in the Table 4.5.

Crystal	Contact
n-type ZnSe/ZnS	Cr-Ag
n-type ZnSe/ZnS	Al-Ag
n-type ZnSe/ZnS	Cu-Ag
n-type ZnSe/ZnS	Ti-Ag
n-type ZnSe/ZnS	Fe-Ag

Table 4.5. Metal contacts deposited on ZnS and ZnSe samples

The best results for Chromium doped ZnS and ZnSe samples were demonstrated for Cr-Ag contact pairs. To fabricate ohmic contact a 50 nm chromium thin film were deposited on the crystals surfaces and annealed at 900°C for three hours. After it, a 200 nm silver film was deposited. Figure 4.5.1 shows I-V measurements of the n-type Al: Cr:ZnS(Se) samples with Cr-Ag contacts. As one can see from the Figure, the Cr-Ag metal contacts reveal good Ohmic formation on studied samples.

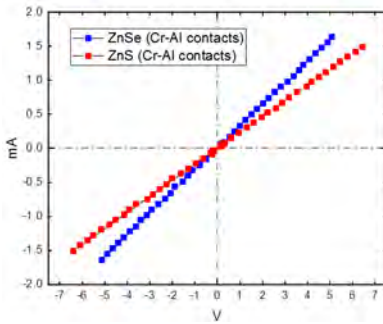


Figure 4.5.1 shows I-V measurements of the n-type Al: Cr:ZnS(Se) samples with Cr-Ag contacts

4.6 Mid-IR Electro Luminescence of n-type Cr:ZnSe Crystal

The bulk n-doped Cr:Al:ZnSe crystals were prepared using two post-growth thermal diffusions of Cr and Al, respectively. The sizes of samples were about 1x4x4 mm. During the first thermo-diffusion the ZnSe samples were placed on top of Zn and CrSe powder and annealed in sealed evacuated ampoules (~10⁻⁵ Torr) for seven days at 950°C for crystal doping with active Cr²⁺ ions. Zinc powder was used in the annealing to prevent the formation of Zn vacancies, and CrSe was used to compensate for sublimation of Se. The n-type samples were obtained by diffusion of Al impurities. The crystals were placed on top of mixture of Zn and Al powders (97 wt.% of Zn and 3 wt% of Al), and again placed in identical evacuated ampoules. They were annealed for 100 hours at 950°C. At the end of the Aluminum annealing, the samples were quickly cooled by immersion in water. Subsequent thermo-diffusion of Al in Cr:ZnSe was accompanied by ~ two-fold decrease of the Cr²⁺ coefficient of absorption. The procedure of formation of the Ohmic contacts was as follows: in the beginning, the surfaces of the samples were slightly polished and cleaned to avoid surface conductivity effects. After drying, the crystal was heated to about 120°C and liquid Indium was applied to the facet of the crystal. Once the Indium wet the surface and spread evenly over it, the crystals were placed on an uncoated side and heated to about 250°C for several minutes. This heating allowed near-surface diffusion of Indium necessary for proper contact formation [9]. The current-voltage I-V experiments were performed to control the formation of the Ohmic contacts and to establish samples resistivity. The chromium concentration in the samples was controlled using absorption spectrum measured with Shimadzu UV-VIS-NIR 3101PC Spectrophotometer. A typical room temperature mid-infrared absorption spectrum of Cr:ZnSe reveals a peak at 1.75 μm corresponding to the ⁵T₂→⁵E transition of Cr²⁺ ions in ZnSe with maximum absorption cross-section $\sigma \approx 10^{-18}$ cm². After chromium diffusion procedure the average absorption coefficient of Cr:ZnSe samples was about $k = 4$ cm⁻¹, which corresponds to Cr²⁺ ions concentration $N = 4 \times 10^{18}$ cm⁻³. Subsequent thermo-diffusion of Al in Cr:ZnSe was

accompanied by \sim two-fold decrease of the Cr^{2+} coefficient of absorption. However, Cr^{2+} absorption could still be observed. One of the reason of the Cr^{2+} suppression could be compensation of divalent chromium by donor impurities in Cr:Al:ZnSe samples.

The I-V measurements demonstrated that before aluminum doping procedure the Cr:ZnSe sample had high resistivity $\rho > 10^{10} \Omega\text{cm}$. In n-type Al-doped samples the dark resistivity at room temperature was decreased down to a value of $\rho = 10^3\text{-}10^2 \Omega\text{cm}$.

For electrical excitation of luminescence of n-doped Cr:Al:ZnSe crystals a High Voltage HP Pulse Generator was used. In order to avoid background from blackbody radiation the operation frequency was 0.1- 1 kHz. Pulses with peak values up to 1kV were applied to the samples. The electroluminescence measurements were taken using an Acton Research Corp. SpectraPro-300i Monochromator/Spectrograph.

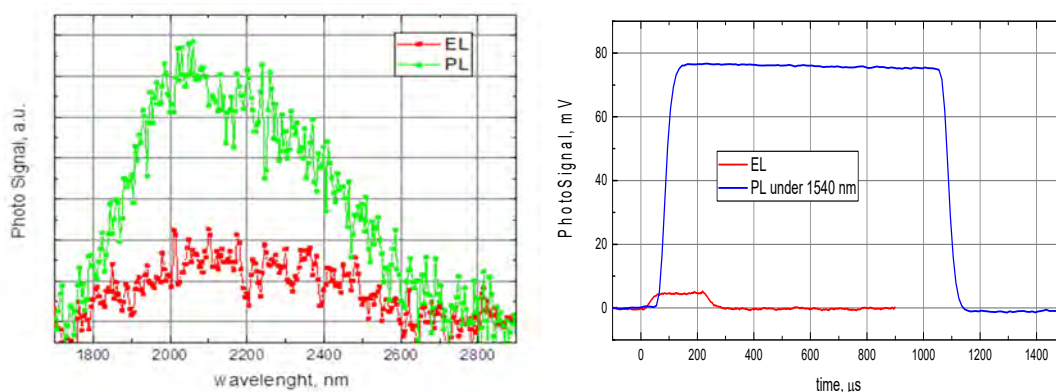


Figure 4.6.1 Left: Photo and electrical luminescence spectra of Al:Cr:ZnSe bulk sample at ${}^5\text{E}-{}^5\text{T}_2$ transition. Right; Comparison of the PL and EL signal of A:Cr:ZnSe sample

Emission spectra of the samples under direct optical excitation at ${}^5\text{T}_2 \leftrightarrow {}^5\text{E}$ transition of Cr^{2+} ions were also studied and compared with doped bulk samples. The emission was detected by photomultiplier in the visible spectral range and near IR. The emission spectra of ${}^5\text{T}_2 \leftrightarrow {}^5\text{E}$ transition of the Cr:Al:ZnSe samples under optical excitation were identical and in a good agreement with the published data. Under electrical excitation the luminescence signals in three spectral bands were observed. In the visible range a strong emission peak was detected near 600nm. Some authors assign this emission to $\text{V}_{\text{zn}}\text{-Al}$ complex in conductive crystals. The distinct peak in the 1800 – 2400 nm range corresponds to a well-known Cr^{2+} luminescence. Figure 4.6.1(right) shows typical oscilloscope traces of the voltage across the sample (I) and mid IR optical signal (II). Optical signal was measured by PbSe detector. In addition to these bands the luminescence band around 8 μm was also observed under electrical excitation. Two possible mechanisms were suggested for electrical excitation of Cr^{2+} . According to one of them Cr^{2+} centers in

ZnSe are directly excited by the impact of hot carriers. This mechanism is usually observed in Mn:ZnS TFEL devices [10]. Another possible mechanism of excitation suggests impact ionization of Cr^{2+} .

Summarizing, Room Temperature electroluminescence was achieved in n-type Cr:Al:ZnSe. Visible and mid-IR emissions were observed under electrical excitation. The mid-IR electroluminescence over 1800-2800 nm spectral range is in a good agreement with Cr^{2+} fluorescence under optical excitation.

5. Optical parametric oscillation in random medium

So far, perfectly regular crystals were believed to be essential for the operation of frequency converters based on quadratic nonlinearity $\chi^{(2)}$, such as second harmonic generators and optical parametric oscillators (OPOs). The phase-matching condition is usually achieved either by a proper crystal orientation, or via quasi-phase matching through controlled flipping of crystalline domains [9]. Surprisingly, it appears that a disordered material consisting of randomly-oriented domains, where the nonlinear wave-coupling coefficient arbitrarily varies between its maximum (d_{NL}) and minimum ($-d_{\text{NL}}$) values, might perform equally well.

Our approach is based on the phenomenon known as random phase matching (RPM) [58, 59]. RPM in disordered $\chi^{(2)}$ materials can be described by the random walk (or 'drunken sailor walk') theory (the same theory accounts for such phenomena as diffusion and heat transfer); it eliminates the need for orientation patterning and, most importantly, enables 3-wave interactions with extremely large bandwidths. A broadband and flat response in RPM is the result of phase randomization due to arbitrary distribution of the crystalline domains, which eliminates destructive interference.

The price to pay, however, is a slow growth of the output signal: the output intensity in RPM scales linearly with sample length, as opposed to the quadratic dependence for perfect phase (or quasi-phase) matching. Although in continuous-wave and nanosecond laser regimes RPM is much less efficient, than the conventional quasi-phase matching process [59], we claim that RPM is very well suited for three-wave processes when few-cycle pump laser pulses with broad spectra are used [60].

We recently demonstrated the world's first OPO based on RPM in ZnSe ceramics [61]. The OPO was synchronously pumped by a Kerr-lens mode-locked Cr:ZnS laser. The bow-tie ring OPO cavity contained a 1.5-mm-thick ZnSe ceramic sample (average grain size 100 μm) placed at Brewster angle and operated in the subharmonic mode near degeneracy. The oscillation threshold was 90 mW and the output spectrum spanned 3–7.5 μm . The observed pump depletion was 79%, which indicates that with an optimized outcoupling one can obtain high, approaching 100%, conversion efficiency.

In our view, RPM in ZnSe and in similar readily accessible random ceramics (ZnS, ZnTe, ZnO, CdSe, GaP, GaN ...) opens a new direction in nonlinear optics and represents a viable route for generation of few-cycle pulses and multi-octave frequency combs.

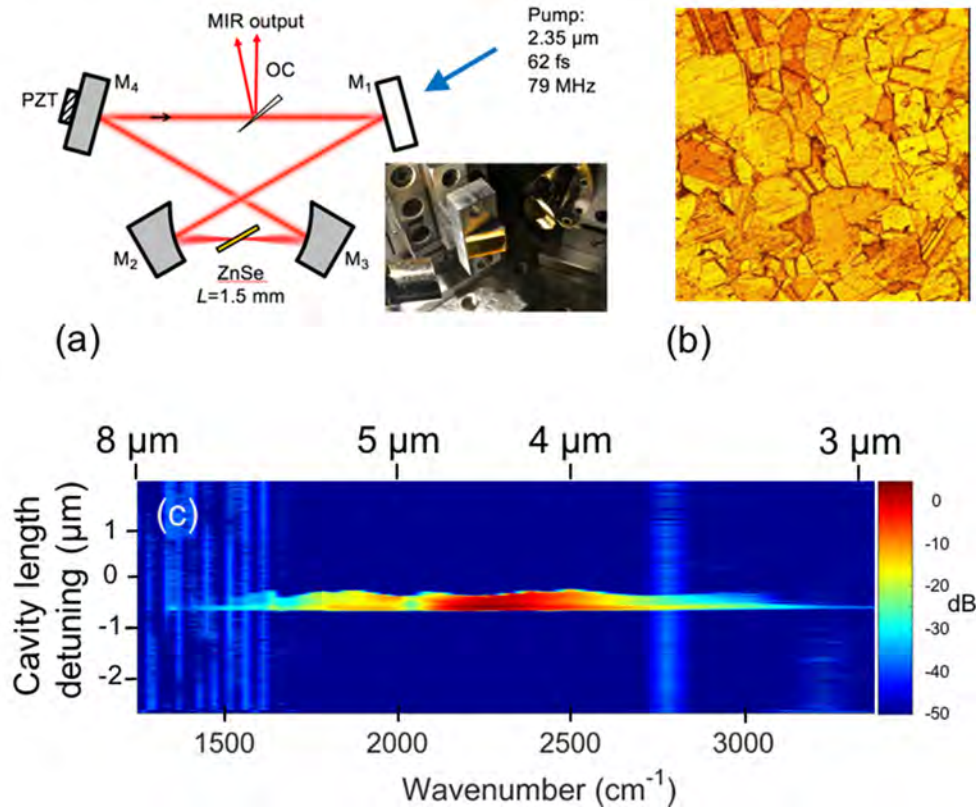


Figure 5.1 (a) Schematic of the RPM OPO. M1, incoupling dielectric mirror; M2-M4, gold-coated mirrors. OC, an OPO outcoupler. PZT, piezo-actuator for the cavity-length control. Inset: OPO 'engine' including the ZnSe ceramic sample located between two parabolic mirrors. (b) 500 x 500 μm cross section of our chemically etched ZnSe ceramic sample. (c) OPO output spectrum vs. cavity-length detuning showing a continuous spectral span of 3–7.5 μm.

6. Conclusions

1. Cation vacancy assisted γ -radiation -enhanced thermal diffusion of iron ions into II-VI crystals (up to 60% improvement)
2. Cation impurity assisted enhanced thermal diffusion of Cr ions into II-VI crystals (up to 500% improvement).
3. Electric field stimulated diffusion is questionable due to high temperature electronic conductivity of ZnSe.

4. Breakthrough in Fe diffusion enhancement (4 orders of magnitude) in ZnS during hot isostatic pressing accompanied by recrystallization into cm size single crystals.
5. Successful diffusion of the RE ions in ZnSe/ZnS in bulk and power samples Cr:ZnS IR transparent ceramics (67% transmittance & 11 μm) fabricated via vacuum hot pressing by consolidating colloiddally processed ZnS powders mixed with commercially sourced Cr_2S_3 powders.
6. Demonstrated *n-type* doping of ZnSe and Cr:ZnSe in PLD using Cl as dopant.
7. Achieved doping of ZnSe in PLD using mixed (ZnSe + Cu_2Se) pressed powder targets (likely *p-type*).
8. Reduced dislocation density in ZnSSe/GaAs films by adding ZnSe buffer layer
9. Demonstrated control of co-doping in the mid-IR active layer to achieve resistivities compatible with electrical injection.
10. Obtained p-n junction EL structure without optical confinement layers.
11. Lasing under optical excitation with photoionization transition realized.
12. Fabrication process for Ohmic Contact formation for Cr:ZnSe/ZnS bulk samples was developed.
13. Optimization of the annealing process of a TM doped Zn/ZnSe samples in Al- vapors results in n- type conductive ZnSe samples with preserved Cr concentration.
14. Strong quenching of the visible EL by TM ions indicates efficient energy transfer to TM ions.
15. Strong mid-IR electroluminescence of Cr:ZnSe ($N_{\text{Cr}}=2 \times 10^{18} \text{ cm}^{-3}$) was realized. Comparison of the mid-IR photo- and electro- luminescence in Cr:ZnSe crystals led to estimation of the laser threshold for electrical excitation $\sim 2.3 \text{ A/cm}^2$. We are \sim order of magnitude below the threshold.

7. REFERENCES

- ¹ V. V. Fedorov, W. Mallory, Jr., S. B. Mirov, U. Hömmerich, S. B. Trivedi, and W. Palosz, "Iron doped $Cd_xMn_{1-x}Te$ Crystals for Mid-IR Room Temperature Lasers," *J. of Crystal Growth* **310**, 4438-4442, (2008).
- ² N. Myoung, V.V. Fedorov, S.B. Mirov, L.E. Wenger, "Temperature and Concentration Quenching of Mid-IR Photoluminescence in Iron Doped ZnSe and ZnS Laser Crystals", *J. Luminescence* **132**, 600–606 (2012).
- ³ L. Podlowski, R. Heitz, P. Thurian, A. Hoffmann, and I. Broser, "Nonradiative Transition Rates of Fe^{2+} in III–V and II–VI Semiconductors," *J. Lumin.*, **58**, 252–256, (1994).
- ⁴ S. B. Mirov, V. V. Fedorov, I. S. Moskalev, D. V. Martyshkin, "Frontiers of Mid-Infrared Lasers Based on Transition Metal Doped II-VI Semiconductors," *Journal of Luminescence*, **133**, 268-275. (2013).
- ⁵ A.D. Martinez, D. V. Martyshkin, R. P. Camata, V. V. Fedorov, S. B. Mirov, "Crystal Field Engineering of Transition Metal Doped II-VI Ternary and Quaternary Semiconductors for Mid-IR Tunable Laser Applications," Submitted to *Optics Materials Express* (2015).
- ⁶ U. Hömmerich, J. T. Seo, A. Bluiett, M. Turner, D. Temple, S. B. Trivedi, H. Zong, S. W. Kutcher, C. C. Wang, R. J. Chen, and B. Schumm, —Mid-Infrared Laser Development Based on Transition Metal Doped Cadmium Manganese Telluride, *J. Lumin.* **87–89**, 1143–1145 (2000).
- ⁷ S. B. Trivedi, C. C. Wang, S. Kutcher, U. Hommerich, and W. Palosz, —Crystal Growth Technology of Binary and Ternary II-VI Semiconductors for Photonic Applications, *J. Cryst. Growth* **310** (6), 1099–1106 (2008)
- ⁸ K. Swiatek, M. Godlewski, and T.P. Surkova, "Fe photoionization transitions in ZnS_{Se}:Fe crystals – photo-ESR studies " *phys. stat. sol. (c)* **2**, No. 3, 1224– 1227 (2005).
- ⁹ C. I. Rablau, "Photoluminescence And Optical Absorption Spectroscopy of Infrared Materials Cr^{2+} :Znse and $ZnGeP_2$ " Ph.D. Thesis, West Virginia University, (1999).
- ¹⁰ R. Pappalardo and R. D. Dietz, "Absorption Spectra of Transition Ions in CdS Crystals," *Phys. Rev.* **123**, 1188-1203 (1961).
- ¹¹ V.I. Levchenko, V.N. Yakimovich, L.I. Postnova, V.I. Konstantinov, V.P. Mikhailov, N.V. Kuleshov, "Preparation and Properties of Bulk ZnSe:Cr Single Crystals," *Journal of Crystal Growth* **198/199**, 980-983 (1999).
- ¹² U. Hömmerich, I. K. Jones, E. E. Nyein, S. B. Trivedi, "Comparison of Optical Properties of Diffusion-doped Polycrystalline Cr:ZnSe and Cr:CdTe." *Journal of Crystal Growth*, **287**, 450-453. (2006).
- ¹³ K. Ghraham, S.B. Mirov, V.V. Fedorov, M.E. Zvanut, A. Avanesov, V. Badikov, B. Ignat'ev, V. Panutin, G. Shevirnyaeva, "Spectroscopic Characterization and Laser Performance of Diffusion Doped Cr^{2+} :ZnS," *OSA TOPS*, **50**, 561-567 (2001).
- ¹⁴ J. -O. Ndap, K. Chattopadhyay, O. O. Adetunji, D. E. Zelmon, A. Burger, "Thermal Diffusion of Cr^{2+} in Bulk ZnSe," *Journal of Crystal Growth* **240**, 176–184 (2002).
- ¹⁵ S. Mirov, V. Fedorov, I. Moskalev, and D. Martyshkin, invited paper "Recent Progress in Transition Metal Doped II-VI Mid-IR Lasers", *J. of Special Topics in Quantum Electronics*, **13** (3), 810-822 (2007).
- ¹⁶ S.B. Mirov, V.V. Fedorov, "Mid-IR microchip laser: ZnS:Cr²⁺ Laser and Saturation Absorption material", US Patent No 6,960,486.
- ¹⁷ S. Mirov, V. Fedorov, D. Martyshkin, I. Moskalev, M. Mirov, S. Vasilyev, "Progress in Mid-IR Lasers Based on Cr and Fe Doped II-VI Chalcogenides", *IEEE J. of Selected Topics in QE*, **21** (1), 1601719 (2015).
- ¹⁸ N. Myoung, D. V. Martyshkin, V. V. Fedorov, A. Martinez and S. B. Mirov, "Energy Scaling of Room Temperature Fe^{2+} :ZnSe Gain-Switched 4.3 μm Laser", *Proc. SPIE* **7912**, 79121C (2011).
- ¹⁹ N. Myoung, "Development and Characterization of Thermal Diffusion Doped Fe^{2+} :ZnSe/ZnS Polycrystalline Gain Media for Room Temperature Mid-IR Lasing," Ph.D. dissertation, Dept. of Physics, University of Alabama at Birmingham, Birmingham, AL, 2011.
- ²⁰ T. R. Allen and G. S. Was, "Radiation-Enhanced Diffusion and Radiation-Induced Segregation," In K. E. Sickafus, E. A. Kotomin, and B. P. Uberuage, editors, *Radiation Effects in Solids*, chapter 6. Springer, 2007.
- ²¹ H. Wolf, J. Kronenberg, F. Wagner, Th. Wichert, "Pre-requisites for the formation of unusual diffusion profiles in II–VI semiconductors," *Phys. Status Solidi B* **247** (6), 1405–1408 (2010).
- ²² T. Konak, M. Tekavec, V. V. Fedorov, S. B. Mirov, "Electrical, Spectroscopic, and Laser Characterization of γ -Irradiated Transition Metal Doped II-VI Semiconductors," *Optical Materials Express* **3** (6), 777-786 (2013).

- ²³ U. Demirbas, A. Sennaroglu, M. Somer, "Synthesis and Characterization of Diffusion-Doped Cr²⁺:ZnSe and Fe²⁺:ZnSe," *Optical Materials* **28**, 231–240 (2006).
- ²⁴ H. Mehrer, *Diffusion in solids: Fundamentals, Methods Materials, Diffusion-Controlled Processes*, Springer, Berlin, Heidelberg & New York, Ch. 3 (2007).
- ²⁵ "Gamma Radiation-Enhanced Thermal Diffusion of Transition Metal Ions into II-VI Semiconductor Crystals" A. Martinez, L. Williams, V. Fedorov, S. Mirov, ASSL (OSA), Shanghai, China, November 16-21 (2014).
- ²⁶ A. Martinez, L. Williams, V. Fedorov, S. B. Mirov, "Gamma Radiation-Enhanced Thermal Diffusion of Transition Metal Ions into II-VI Semiconductor Crystals", in *Advanced Solid-State Lasers*, G. Huber and P. Moulton, eds., OSA Technical Digest (online) (Optical Society of America, 2014), paper ATu2A.13 (3 pages).
- ²⁷ "Gamma Radiation-Enhanced Thermal Diffusion of Transition Metal and Rare Earth Ions into II-VI Semiconductor Crystals," A. Martinez, L. Williams, O. Gafarov, D. Martyshkin, V. Fedorov, S. Mirov, Photonics West (SPIE), San Francisco, CA, USA, February 10-12 (2015).
- ²⁸ A. Martinez, L. Williams, O. Gafarov, D. Martyshkin, V. Fedorov, S. Mirov "Radiation-Enhanced Thermal Diffusion of Transition Metal and Rare Earth Ions into II-VI Semiconductors", *Proc. SPIE 9342, Solid State Lasers XXIV: Technology and Devices*, 9342-15 (2015).
- ²⁹ A. Martinez, L. Williams, V. Fedorov, S. Mirov, "Gamma Radiation-Enhanced Thermal Diffusion of Iron Ions into II-VI Semiconductor Crystals," *Optics Materials Express*, **5** (3), 558-565 (2015).
- ³⁰ "Spectroscopic Characterization of Pr³⁺:ZnSe Crystals Fabricated via Post-Growth Thermal Diffusion" A. Martinez, O. Gafarov, D. Martyshkin, V. Fedorov, S. Mirov, CLEO (OSA) San Jose, CA, USA, May 10-15 (2015).
- ³¹ K. Bentley, R. Kawai, University of Alabama at Birmingham, personal, personal communication.
- ³² U. M Gosele, "Fast Diffusion in Semiconductors," *Annual Review of Materials Scienc* Vol. 18: 257-282 (1988).
- ³³ J.-O. Ndap, K. Chattopadhyay, O. O. Adetunji, D. E. Zelmon, and A. Burger, "Thermal diffusion of Cr²⁺ in bulk ZnSe," *J. Cryst. Growth* 240(1-2), 176–184 (2002).
- ³⁴ S. B. Zhang, S.-H. Wei, and A. Zunger, "Intrinsic n-type versus p-type doping asymmetry and the defect physics of ZnO," *Phys. Rev. B*, **63**, 075205 (2001).
- ³⁵ L.L. Kulyuk, D.D. Nedeoglo, A.V. Siminel, and K.D. Sushkevich, "Effect of annealing of ZnSe:Cr crystals in Bi(Zn) melt on the intensity of radiation bands of Cr ions," *Moldavian J. of the Physical Sciences*, 9(2), 138-140 (2010).
- ³⁶ M. Aven and H. H. Woodbury, "Purification of II-VI compounds by solvent extraction," *Appl. Phys. Lett.* **1**, 53 (1962).
- ³⁷ G. H. Blount, A. C. Sanderson, and R. H. Bube, "Effects of Annealing on the Photoelectronic Properties of ZnS Crystals," *J. Appl. Phys.* **38**, 4409 (1967).
- ³⁸ A.V. Savitskii, V.I. Tkachuk, and P.N. Tkachuk, *Sov. Phys. Semicond.* **26**, 536 (1992).
- ³⁹ A. E. Dormidonov, K. N. Firsov, E. M. Gavrishchuk, V. B. Ikonnikov, S. Yu. Kazantsev, I. G. Kononov, T. V. Kotereva, D. V. Savin, N. A. Timofeeva, "High-efficiency room-temperature ZnSe:Fe²⁺ laser with a high pulsed radiation energy," *Appl. Phys. B*, 122:211 (2016).
- ⁴⁰ E. V. Karaksina, V. B. Ikonnikov, and E. M. Gavrishchuk, "Recrystallization Behavior of ZnS during Hot Isostatic Pressing," *Inorganic Materials*, 43(5), 452–454 (2007)
- ⁴¹ D.R. Vij, and N Singh, "Luminescence and Related Properties if II-VI Semiconductors," (Commack, NY, 1998), p 172.
- ⁴² A.G.Okhrimchuk, L.N.Butvina, E.M.Dianov, N.V.Lichkova, V.N.Zagorodnev, A.V.Shestakov, "Oscillation on the RbPb₂Cl₅:Pr³⁺ Crystal within the 2.31-2.59 μm Emission Band", CThFF3 Lasers and Electro-Optics, 2006 and 2006 Quantum Electronics and Laser Science Conference. CLEO/QELS 2006.
- ⁴³ S. R. Bowman, J. Ganem, B. J. Feldman, and A. W. Kueny, "Infrared laser characteristics of praseodymium-doped lanthanum trichloride," *IEEE J. Quantum Electron.* **30**(12), 2925-2928 (1994).
- ⁴⁴ S. R. Bowman, L. B. Shaw, B. J. Feldman, and J. Ganem, "A 7-μm Praseodymium-based Solid-state Laser," *IEEE J. Quantum Electron.* **32**(4), 646 (1996).
- ⁴⁵ Yu, L. S., Jia, L., Qiao, D., Lau, S. S., Li, J., Lin, J. Y., & Jiang, H. X. (2003). "The origins of leaky characteristics of schottky diodes on p-GaN." *IEEE Transactions on Electron Devices*, 50(2), 292-296. doi:10.1109/TED.2002.808558
- ⁴⁶ Crowell, C.R. & Rideout, V.L. (1969). "Normalized Thermionic-Field (T-F) Emission in Metal-Semiconductor (Schottky) Barriers." *Solid-State Electronics*, Vol. 12, pp. 89-105.

-
- ⁴⁷ Marple, D. T. F. (1964). "Electron effective mass in ZnSe." *Journal of Applied Physics*, 35(6), 1879-1882. doi:10.1063/1.1713761
- ⁴⁸ Xu, F., Vos, M., Weaver, J. H., & Cheng, H. (1988). "Interface dipoles, surface work functions, and schottky-barrier formation at Au/ZnSe(100) interfaces." *Physical Review B*, 38(18), 13418-13421. doi:10.1103/PhysRevB.38.13418
- ⁴⁹ . Koide, Y., Kawakami, T., Teraguchi, N., Tomomura, Y., Suzuki, A., & Murakami, M. (1997). "Schottky barrier heights of metals contacting to p-ZnSe." *Journal of Applied Physics*, 82(5), 2393-2399. doi:10.1063/1.366049
- ⁵⁰ . Bueno, P. R., Varela, J. A., & Longo, E. (2007). "Admittance and dielectric spectroscopy of polycrystalline semiconductors." *Journal of the European Ceramic Society*, 27(13-15), 4313-4320. doi:10.1016/j.jeurceramsoc.2007.02.155
- ⁵¹ Thirumoorthi, M., & Thomas Joseph Prakash, J. (2016). "Structure, optical and electrical properties of indium tin oxide ultra-thin films prepared by jet nebulizer spray pyrolysis technique." *Journal of Asian Ceramic Societies*, 4(1), 124-132. doi:10.1016/j.jascer.2016.01.001
- ⁵² Perna, G., Capozzi, V., Plantamura, M. C., Minafra, A., Orlando, S., & Marotta, V. (2002). "ZnSe films deposited on crystalline GaAs and amorphous quartz substrates by means of pulsed laser ablation technique." *European Physical Journal B*, 29(4), 541-545. doi:10.1140/epjb/e2002-00337-0
- ⁵³ Gezci, S., & Woods, J. (1975). Edge emission in zinc selenide. *Journal of Luminescence*, 10(4), 267-272. doi:10.1016/0022-2313(75)90075-7
- ⁵⁴ Jones, G., & Woods, J. (1974). "The luminescence of self-activated and copper-doped zinc selenide." *Journal of Luminescence*, 9(5), 389-405. doi:10.1016/0022-2313(74)90032-5
- ⁵⁵ Kuznetsov, P. I., Yakushcheva, G. G., Jitov, V. A., Zakharov, L. Y., Shchamkhalova, B. S., Kozlovsky, V. I., Tiberi, M. D. (2006). "MOVPE growth and study of ZnCdSe/ZnSSe MQW structures for green VCSELs." Paper presented at the *Physica Status Solidi C: Conferences*, 3(4) 771-775. doi:10.1002/pssc.200564685
- ⁵⁶ Fedorov, V. V., Gallian, A., Moskalev, I., & Mirov, S. B. (2007). "En route to electrically pumped broadly tunable middle infrared lasers based on transition metal doped II-VI semiconductors." *J. Lumin.*, 125: 184.
- ⁵⁷ Radevici, I. (2014). "Influence of the chromium and ytterbium co-doping on the photoluminescence of zinc selenide crystals." *Journal of Rare Earths*, 32(10), 938-945. doi:10.1016/S1002-0721(14)60166-6
- ⁵⁸ E. Yu. Morozov and A. S. Chirkin, "Stochastic quasi-phase matching in nonlinear-optical crystals with an irregular domain structure," *Sov. J. Quantum Electron.* 34, 227-232 (2004)
- ⁵⁹ M. Baudrier-Raybaut, R. Haïdar, P. Kupecek, P. Lemasson, E. Rosencher "Random quasi-phase-matching in bulk polycrystalline isotropic nonlinear materials", *Nature* 432, 374 (2004).
- ⁶⁰ S. Vasilyev, I. Moskalev, M. Mirov, V. Smolski, S. Mirov, V. Gapontsev "Ultrafast middle-IR lasers and amplifiers based on polycrystalline Cr:ZnS and Cr:ZnSe", *Opt. Materials Express* 7, 2636 (2017).
- ⁶¹ Q. Ru, N. Lee, X. Chen, K. Zhong, G. Tsoy, M. Mirov, S. Vasilyev, S. B. Mirov, K. L. Vodopyanov "Optical parametric oscillation in a random polycrystalline medium" *Optica* 4, 617 (2017).

AFOSR Deliverables Submission Survey

Response ID:10430 Data

1.

Report Type

Final Report

Primary Contact Email

Contact email if there is a problem with the report.

mirov@uab.edu

Primary Contact Phone Number

Contact phone number if there is a problem with the report

2059348088

Organization / Institution name

The University of Alabama at Birmingham

Grant/Contract Title

The full title of the funded effort.

Transition metal and rare earth doped II-VI chalcogenides for optically and electrically pumped broadly tunable mid-IR lasers

Grant/Contract Number

AFOSR assigned control number. It must begin with "FA9550" or "F49620" or "FA2386".

FA9550-13-1-0234

Principal Investigator Name

The full name of the principal investigator on the grant or contract.

Sergey Mirov

Program Officer

The AFOSR Program Officer currently assigned to the award

Dr. Ali Sayir

Reporting Period Start Date

09/30/2013

Reporting Period End Date

09/29/2018

Abstract

AFOSR sponsored research work at University of Alabama at Birmingham enabled development of new middle-infrared chalcogenide laser materials via post-growth radiation and hot isostatic pressing enhanced thermal diffusion of laser active transition metal impurities into the polycrystalline crystal host. We report on unique process of recrystallization and effective doping of ZnS ceramics under hot isostatic pressing resulting in a large cm-scale monocrystalline domains formation and an increase of the Fe diffusion length by four orders of magnitude. In collaboration with the University of Central Florida and IPG Photonics Corporation a new breakthrough was demonstrated: a first ultrafast optical parametric oscillator based on random phase matching in disordered polycrystal, ZnSe ceramic. A new kinetic Monte Carlo simulation algorithm for cation diffusion in zinc blend (ZB) crystals has been developed. One of difficulty is the lattice indexing for ZB crystals. We found that diffusion in ZB crystals can be mapped to the diffusion in the four-dimensional simple cubic crystal with certain constraints. This algorithm has various advantage, in particular it finds the neighboring lattice sites quickly and also it makes it very easy to calculate the hopping distance between two distance lattice sites. Using this algorithm, we have simulated diffusion processes

DISTRIBUTION A: Distribution approved for public release.

based on interstitial-assisted knock-out and vacancy-assisted mechanisms. The simulation was carried out on the cluster computer using 500 cores. The results are analyzed with waiting time distribution. The relation between the diffusion constants and concentration of the assisting impurities. Based on the the results we are able to explain the increases of Cr-ion diffusion rate under high concentration of Zn interstitials in ZnS. UAB team also created a multilayer thin film structure that integrates an optically-active mid-IR material (Cr²⁺-doped ZnSe) with carrier-injection layers using pulsed laser deposition as a single fabrication platform. The resistivity, crystalline quality, and interface defect densities of the structure are within the range required for light emission under electrical excitation. With the addition of optical confinement layers to the structure, this technology may open the way for electrically-pumped, compact, tunable, mid-IR laser sources that operate at room temperature.

Distribution Statement

This is block 12 on the SF298 form.

Distribution A - Approved for Public Release

Explanation for Distribution Statement

If this is not approved for public release, please provide a short explanation. E.g., contains proprietary information.

SF298 Form

Please attach your SF298 form. A blank SF298 can be found [here](#). Please do not password protect or secure the PDF. The maximum file size for an SF298 is 50MB.

[sf0298.pdf](#)

Upload the Report Document. File must be a PDF. Please do not password protect or secure the PDF. The maximum file size for the Report Document is 50MB.

[2018_09_UAB__AF_final_report.pdf](#)

Upload a Report Document, if any. The maximum file size for the Report Document is 50MB.

Archival Publications (published) during reporting period:

Dissertations (4)

1. Alan Martinez (Physics), PhD Dissertation, "Spectroscopic Characterization of Iron-doped II-VI Compounds for Laser Applications," August 2015.
2. Jeremy Peppers (Physics) PhD Dissertation, "Study of Cobalt, Cobalt-Iron, and Chromium Doped II-VI Media for Laser Applications," July 2016.
3. Matthew Rhoades (Physics), MS Dissertation, "Pulsed Laser Deposition and Electrical Properties of Zinc Selenide based Thin Film Structures For Integration With Mid-Infrared Applications," April 2018.
4. Z. R. Lindsey, "Growth and Analysis of Transition-Metal-Doped ZnSe-based Materials and Thin Film Structures for Mid-Infrared Optoelectronic Applications," Ph.D. Dissertation (Physics), successfully defended on August 8, 2018.

Refereed Articles (18)

1. Yu. V. Terekhov, D. V. Martyshkin, V. V. Fedorov, I. Moskalev and S. B. Mirov, "Fiber Pumped Er:YAG Laser Passively Q-Switched by Co:ZnS and Cr:ZnSe crystals". Laser Physics, 24 025003 (5pp) (2014).
2. V.V. Fedorov, T. Konak, J. Dashdorj, M.E. Zvanut, S.B. Mirov, "Optical and EPR spectroscopy of Zn:Cr:ZnSe and Zn:Fe:ZnSe crystals", Optical Materials, 37, 262-266 (2014).
3. S. Mirov, V. Fedorov, D. Martyshkin, I. Moskalev, M. Mirov, S. Vasilyev, "Progress in Mid-IR Lasers Based on Cr and Fe Doped II-VI Chalcogenides", IEEE Selected Topics in Quantum Electronics (Invited paper), vol. 21, no.1, 1601719 (20pp) (2015).
4. A. Martinez, L. Williams, V.V. Fedorov, S.B. Mirov, "Gamma radiation-enhanced thermal diffusion of iron ions into II-VI semiconductor crystals", Optical Materials Express 5(3). 558-565 (2015).
5. J. Peppers, V.V. Fedorov, S.B. Mirov, "Mid-IR photoluminescence of Fe²⁺ and Cr²⁺ ions in ZnSe crystal

DISTRIBUTION A: Distribution approved for public release.

under excitation in charge transfer bands", *Optics Express* 23(4), 4406-4415 (2015).

6. V.O. Smolski, S. Vasilyev, P.G. Schunemann, S.B. Mirov, K.L. Vodopyanov, "Cr:ZnS laser pumped subharmonic GaAs OPO with an instantaneous bandwidth 3.6-5.6 μm ", *Opt. Lett.*, 40(12), 2906-2908 (2015).

7. A.D. Martinez, D.V. Martyshkin, R.P. Camata, V.V. Fedorov, and S.B. Mirov, "Crystal field engineering of transition metal doped II-VI ternary and quaternary semiconductors for mid-IR tunable laser applications", *Optical Materials Express* 5(9), 2036-2046 (2015).

8. S. Vasilyev, I. Moskalev, M. Mirov, S. Mirov, V. Gapontsev, "Multi-Watt mid-IR femtosecond polycrystalline Cr²⁺:ZnS and Cr²⁺:ZnSe laser amplifiers with the spectrum spanning 2.0–2.6 μm ," *Opt. Express* 24(2), 1616-1623 (2016).

9. NoSoung Myoung, JeongSoo Park, Alan Martinez, Jeremy Peppers, Sang-Youp Yim, Won Seok Han, Vladimir V. Fedorov, and Sergey B. Mirov, "Mid-IR spectroscopy of Fe:ZnSe quantum dots," *Opt. Express* 24(5) 5366-5375 (2016).

10. Y. Li, Y. Liu, V.V. Fedorov, S.B. Mirov, Y. Wu, "Hot-pressed chromium doped zinc sulfide infrared transparent ceramics," *Scripta Materialia* 125, 15-18 (2016).

11. I. Moskalev, S. Mirov, M. Mirov, S. Vasilyev, V. Smolski, A. Zakrevskiy, and V. Gapontsev, "140W Cr:ZnSe laser system," *Opt. Express*, 24(18), 21090-21104 (2016).

12. O. Gafarov, A. Martinez, V. Fedorov, S. Mirov, "Enhancement of Cr and Fe diffusion in ZnSe/S laser crystals via annealing in vapors of Zn and hot isostatic pressing," *Opt. Materials Express*, 7(11), 25-31 (2017).

13. Q. Ru, N. Lee, X. Chen, K. Zhong, G. Tsoy, M. Mirov, S. Vasilyev, S. Mirov, and K. Vodopyanov, "Optical parametric oscillation in a random polycrystalline medium," *Optica (memorandum)*, 4(6), 617-618 (2017).

14. D. Hobbs, B. Macleod, E. Sabatino, S. Mirov, D. Martyshkin, M. Mirov, G. Tsoy, S. McDaniel, and G. Cook, "Laser testing of anti-reflection microstructures fabricated in ZnSe and chromium-ion doped ZnSe laser gain media," *Opt. Materials Express* 7(9), 3377-3388 (2017).

15. C. Canalias, S. Mirov, T. Taira, and B. Boulanger, "Feature issue introduction: shaping and patterning crystals for optics," *Optical Materials Express* 7(9), 3466-3470 (2017).

16. B. Boulanger, S. Jiang, S. Mirov, J. Nilsson, A. Petersen, F. Rotermund, S. Taccheo, T. Taira, "Feature issue introduction: Advanced Solid-State Lasers 2017," *Optical Materials Express* 8 (5), 1246-1252 (2018).

17. A. Sincore, J. Cook, F. Tan, A. El Halawany, A. Riggins, S. McDaniel, G. Cook, D.V. Martyshkin, V.V. Fedorov, S.B. Mirov, L. Shah, A.F. Abouraddy, M.C. Richardson, K.L. Schepler, "High power single-mode delivery of mid-infrared sources through chalcogenide fiber," *Optics Express*, 26 (6), 7313-7323, (2018).

18. Sergey Mirov, Igor Moskalev, Sergey Vasilyev, Viktor Smolski, Vladimir Fedorov, Dmitry Martyshkin, Jeremy Peppers, Mike Mirov, Alex Dergachev, Valentin Gapontsev, invited paper "Frontiers of mid-IR lasers based on transition metal doped chalcogenides," *IEEE Journal of Selected Topics in Quantum Electronics (Early Access)*, 20 February 2018, pp 1-29. DOI: 10.1109/JSTQE.2018.2808284.

Proceedings (16)

1. J. M. Peppers, T. Konak, D. V. Martyshkin, V. V. Fedorov, S. B. Mirov, "Spectroscopy and mid-IR lasing of

DISTRIBUTION A: Distribution approved for public release.

- Cr²⁺ ions in ZnSe/ZnS crystals under visible excitation" Proc. SPIE, Solid State Lasers XXIII: Technology and Devices, vol. 8959, p. 89590E(pp.7), (2014).
2. A. D. Martinez, D. V. Martyshkin, V. V. Fedorov, S. B. Mirov, "Spectroscopic characterization of Fe²⁺-doped II-VI ternary and quaternary mid-IR laser active powders", Proc. SPIE, Solid State Lasers XXIII: Technology and Devices, vol. 8959, p. 89591Q(pp.6), (2014).
3. J. M. Peppers, D. V. Martyshkin, V. V. Fedorov, S. B. Mirov, "Spectroscopic characterization and energy transfer process in cobalt and cobalt-iron co-doped ZnSe/ZnS crystals", Proc. SPIE, Solid State Lasers XXIII: Technology and Devices, vol. 8959, p. 89591P(pp.7), (2014).
4. A. Martinez, L. Williams, O. Gafarov, D. Martyshkin, V. Fedorov, S Mirov "Radiation-Enhanced Thermal Diffusion of Transition Metal and Rare Earth Ions into II-VI Semiconductors", Proc. SPIE 9342, Solid State Lasers XXIV: Technology and Devices, 9342-15 (2015).
5. J. M. Peppers, V. V. Fedorov, S. B. Mirov "Spectroscopic characterization of Cr²⁺ ions in ZnSe/ZnS crystals under visible excitation", Proc. SPIE 9342, Solid State Lasers XXIV: Technology and Devices, 9342-81 (2015).
6. S. B. Mirov, V. V. Fedorov, D. V. Martyshkin, I. S. Moskalev, M. B. Mirov, S. Vasilyev, "Mid-IR lasers based on transition and rare-earth ion doped crystal (Invited Paper)" Proc. SPIE 9467, Micro- and Nanotechnology Sensors, Systems, and Applications VII, 94672K (2015).
7. S.B. Mirov, V.V. Fedorov, D.V. Martyshkin, I.S. Moskalev, M.S. Mirov, O. Gafarov, A. Martinez, J. Peppers, V. Smolski, S. Vasilyev, and V. Gapontsev, "Mid-IR Gain Media Based on Transition Metal Doped II-VI Chalcogenides", invited paper, Proc. SPIE, Optical Components and Materials XIII, Vol. 9744, 97440A (2016).
8. Sergey Vasilyev, Igor Moskalev, Mike Mirov, Sergey Mirov, Valentin Gapontsev, "Mid-IR Kerr-lens mode-locked polycrystalline Cr²⁺:ZnS lasers," invited paper, Proc. SPIE, Defense + Commercial Sensing, Ultrafast Bandgap Photonics Conference, vol.9835, 98350W (2016).
9. Zachary Lindsey, Matthew Rhoades, Vladimir Fedorov, Sergey Mirov, Renato Camata, "Pulsed Laser Deposition of Epitaxial Zn_{Sx}Se_{1-x} Thin Films for Waveguiding Applications in Mid-IR Active Multilayered Structures," MRS Advances, 1-7, 2017 DOI: <https://doi.org/10.1557/adv.2017.166>. Published online: 08 February 2017.
10. Ozarfar Gafarov, Alan Martinez, Vladimir Fedorov and Sergey Mirov, "Enhancement of Fe diffusion in ZnSe/S laser crystals under hot isostatic pressing," Proc. SPIE 10082, Solid State Lasers XXVI: Technology and Devices, 1008213 (February 17, 2017); doi:10.1117/12.2252337.
11. Ozarfar Gafarov, Rick Watkins, Chandler Bernard, Vladimir Fedorov and Sergey Mirov, "Temperature dependence of spectroscopic and electrical properties of Cr(Fe):ZnSe laser active materials," Proc. SPIE 10082, Solid State Lasers XXVI: Technology and Devices, 1008226 (February 17, 2017); doi:10.1117/12.2252670.
12. Dmitry Martyshkin, Taylor Kesterson, Vladimir Fedorov and Sergey Mirov, "Mid-IR CW Cr:ZnS laser tunable with acousto-optical filter," Proc. SPIE 10082, Solid State Lasers XXVI: Technology and Devices, 100820G (February 28, 2017); doi:10.1117/12.2253095.
13. Zachary R. Lindsey, Matthew W. Rhoades, Vladimir V. Fedorov, Sergey B. Mirov, "Pulsed Laser Deposition of Epitaxial Zn_{Sx}Se_{1-x} Thin Films for Waveguiding Applications in Mid-IR Active Multilayered Structures," MRS Advances, 1-7, 2017 DOI: <https://doi.org/10.1557/adv.2017.166>. Published online: 08 February 2017.
14. Shova D Subedi, Vladimir V Fedorov, Jeremy Peppers, Dmitry V Martyshkin, Sergey B Mirov, Linbo Shao, Marko Loncar, "Laser spectroscopy of highly doped NV- centers in diamond", Proc. SPIE 10511, Solid State Lasers XXVII: Technology and Devices, 105112D (20 February 2018) doi: 10.1117/12.2290705; <https://doi.org/10.1117/12.2290705>
15. Ozarfar Gafarov, Dmitriy Martyshkin, Vladimir Fedorov, Sergey Mirov, "Grain growth and significant Fe diffusion in polycrystalline ZnS at elevated temperatures and pressures", Proc. SPIE 10511, Solid State Lasers XXVII: Technology and Devices, 105111R (15 February 2018); doi: 10.1117/12.2290957; <https://doi.org/10.1117/12.2290957>
16. Qitian Ru, Taiki Kawamori, Nathaniel Lee, Xuan Chen, Kai Zhong, Mike Mirov, Sergey Vasilyev, Sergey B. Mirov, Konstantin L. Vodopyanov, "Optical parametric oscillation in a random poly-crystalline medium: ZnSe ceramic", invited paper Proc. SPIE 10516, Nonlinear Frequency Generation and Conversion:

Invited talks sponsored by AFOSR grant

Keynote (2)

1. "Frontiers of Mid-IR lasers based on transition metal doped II-VI chalcogenide ceramics," S.B. Mirov*, I.S. Moskalev, S. Vasilyev, M.S. Mirov, V.V. Fedorov, D.V. Martyshkin, V. Smolski, V. Gapontsev, keynote talk presented at 12th Laser Ceramics Symposium, Saint Louis, France, 28 Nov-2nd Dec. 2016.
2. "Massively parallel sensing of trace molecules and their isotopes with broadband mid-IR frequency combs produced via optical subharmonic generation," K. Vodopyanov*, A. Muraviev, Z. Loparo, S. Vasilyev, S. Mirov, keynote talk presented at SPIE Defense and Security, Ultrafast Bandgap Photonics III Conference, April 18, 2018, Orlando, FL.

Invited (10)

1. "Cr and Fe doped II-VI mid-IR gain media. Fabrication challenges and practical applications in fiber-bulk mid-IR laser systems," S.B. Mirov*, invited talk presented to 20th American Crystal Growth and Epitaxy conference (ACCGE-20), August 2015, Bug Sky, Montana, USA.
2. "Mid-IR Gain Media Based on Transition Metal Doped II-VI Chalcogenides", S.B. Mirov*, V.V. Fedorov, D.V. Martyshkin, I.S. Moskalev, M.S. Mirov, O. Gafarov, A. Martinez, J. Peppers, V. Smolski, S. Vasilyev, and V. Gapontsev, invited talk presented at Photonics West 2016, Optical Components and Materials XIII conference, February 15, 2016, San Francisco, CA, USA.
3. "Mid-IR lasers based on Cr- and Fe-doped ZnSe and ZnS polycrystals," S.B. Mirov*, V.V. Fedorov, D.V. Martyshkin, I.S. Moskalev, M.S. Mirov, S. Vasilyev, V.P. Gapontsev," invited talk presented at Photonics West 2016 Novel In-Plane Semiconductor Lasers XV conference, February 16, 2016, San Francisco, CA, USA.
4. "Mid-IR Kerr-lens mode-locked polycrystalline Cr²⁺:ZnS lasers," Sergey Vasilyev, Igor Moskalev, Mike Mirov, Sergey Mirov*, Valentin Gapontsev," invited talk presented at Defense and Commercial Sensing, Ultrafast Bandgap Photonics Conference, April 17-21, 2016, Baltimore, MA, USA.
5. "Transitioning Cr²⁺ and Fe²⁺ Doped Zn Chalcogenide Laser Technology to Commercial Products – Lessons Learned," S.B. Mirov*, I.S. Moskalev, M.S. Mirov, S. Vasilyev, V.V. Fedorov, D.V. Martyshkin, V. Smolski, and V. Gapontsev, invited talk presented at CLEO'16, June 5-10, 2016, San Jose, CA, USA.
6. "Progress in Cr and Fe doped ZnS/Se mid-IR CW and femtosecond lasers," Sergey Vasilyev, Igor Moskalev, Mike Mirov, Viktor Smolski, Dmitry Martyshkin, Vladimir Fedorov, Sergey Mirov* and Valentin Gapontsev, invited talk presented at SPIE Defense + Commercial Sensing, 2017, April 9-13, Anaheim, CA, USA.
7. "Instantaneous spectral span of 2.85–8.40 μm achieved in a Cr:ZnS laser pumped subharmonic GaAs OPO," Qitian Ru, Kai Zhong, Nathaniel P Lee, Zachary E Loparo, Peter G Schunemann, Sergey Vasilyev, Sergey B Mirov, Konstantin L Vodopyanov*, invited talk presented at CLEO'17, may 14-19, 2017, San Jose, CA, USA.
8. "Optical parametric oscillation in a random poly-crystalline medium: ZnSe ceramic," Qitian Ru, Taiki Kawamori, Nathaniel Lee, Xuan Chen, Kai Zhong, Mike Mirov, Sergey Vasilyev, Sergey B. Mirov, Konstantin L. Vodopyanov*, invited talk presented at Photonics West 2018, Nonlinear Frequency Generation and Conversion: Materials and Devices XVII conference, February 15, 2018, San Francisco, CA, USA.
9. "Femtosecond Mid-IR Laser Sources based on Cr²⁺:ZnS oscillators and sub-harmonic OPOs," Sergey Vasilyev, Viktor Smolski, Igor Moskalev, Jeremy Peppers, Mike Mirov, Andrey Muraviev, Konstantin Vodopyanov, Sergey Mirov*, and Valentin Gapontsev, invited talk presented at SPIE Defense and Security, Ultrafast Bandgap Photonics III Conference, April 18, 2018, Orlando, FL.
10. " Mid-IR Broadly Tunable CW and Ultrafast Lasers Sources Based on Cr and Fe doped Chalcogenides, Subharmonic OPOs and Potential Quantum Cascade - Fe:II-VI Hybrid Platforms," Sergey Mirov*, Igor Moskalev, Sergey Vasilyev, Viktor Smolski, Mike Mirov, Vladimir Fedorov, Dmitri Martyshkin, and Valentin Gapontsev, invited talk presented at SPIE Defense and Security, Micro- and Nanotechnology Sensors, Systems, and Applications X Conference, April 19, 2018, Orlando, FL.

Contributed (26)

ASSL'16 – Best Student Paper: O. Gafarov, V. Fedorov and S. Mirov, "Enhancement of Cr and Fe Diffusion in ZnSe/S Laser Crystals via Annealing in Vapors of Zn and Hot Isostatic Pressing

New discoveries, inventions, or patent disclosures:

Do you have any discoveries, inventions, or patent disclosures to report for this period?

No

Please describe and include any notable dates

Do you plan to pursue a claim for personal or organizational intellectual property?

Changes in research objectives (if any):

None

Change in AFOSR Program Officer, if any:

None

Extensions granted or milestones slipped, if any:

None

AFOSR LRIR Number

LRIR Title

Reporting Period

Laboratory Task Manager

Program Officer

Research Objectives

Technical Summary

Funding Summary by Cost Category (by FY, \$K)

	Starting FY	FY+1	FY+2
Salary			
Equipment/Facilities			
Supplies			
Total			

Report Document

[image.png](#)

[image.png](#)

Report Document - Text Analysis

Report Document - Text Analysis

Appendix Documents

[image.png](#)

[image.png](#)

2. Thank You

E-mail user

DISTRIBUTION A: Distribution approved for public release.

Sep 28, 2018 19:44:57 Success: Email Sent to: mirov@uab.edu